UNIVERSITY OF PADOVA
FACULTY OF ENGINEERING
Department of Management and Engineering
Doctoral School in Mechatronics and Product Innovation Engineering
Cycle XXIX

FUNCTIONAL DESIGN OF MECHATRONIC SYSTEMS FOR HUMAN-ROBOT COLLABORATION

A dissertation submitted in partial fulfillment of the requirements for the degree of Doctor of Philosophy in Mechatronics and Product Innovation Engineering

Prof. Giovanni Antonio Longo, Chair of the School
Prof. Roberto Caracciolo, Course Coordinator
Prof. Aldo Rossi, Candidate's Supervisor
Prof. Giulio Rosati, Candidate's Co-supervisor

Ph.D. Candidate: LUCA BARBAZZA

January 30, 2017

La vita è un dono, dei pochi ai molti, di coloro che sanno e che hanno a coloro che non sanno e che non hanno

— A. Modigliani

ABSTRACT

Traditionally, robots have been caged off from human activity but, recently, improvements in advance robotic technology as well as the introduction of new safety standards, have allowed the possibility of collaboration between human workers and robotic systems. The introduction of Human-Robot Collaboration has the potential to increase the quality and the flexibility of the production process while improving the working condition of the operators. However, traditional industrial robots are typically characterized by small payload and small reachable workspace that reduce the range of possible applications. These drawbacks can overcome the advantages related to a collaborative task and make the collaboration not effective.

This work aims at analyzing innovative mechatronic solutions capable of increasing the workspace and the versatility of the system with the final goal of creating effective collaborations with humans. Cable driven Parallel Robots (CDPRs) are considered a promising technology able to satisfy these requirements. In fact, compared to rigid serial and parallel robots, they have several advantages such as large workspaces, high payloads per unit of weight, ease of construction, versatility and affordable costs.

This work presents two innovative solutions of CDPR able to enlarge the workspace, improve the versatility and reduce the collisions risk. The first solution consists of a cable-suspended parallel robot with a reconfigurable end-effector whereas the second solution is an innovative model of cable-driven micro-macro robot.

In the first part of the thesis, the kinematic and dynamic models of these innovative systems are presented and analyzed in order to characterize their capability. Trajectory planning and optimal design are addressed with the purpose of maximizing the performance of the systems.

The last part of the thesis deals with the design of a novel family of Intelligent CAble-driven parallel roBOTs whose architecture and control are conceived to maximize the robot versatility to the task to be performed and the environment in which the robot is intended to operate.

Keywords: Human-Robot Collaboration, Cable-Driven Robots, functional design, versatility, performance optimization

SOMMARIO

La crescente necessitá di far fronte a produzioni industriali caratterizzate da elevata personalizzazione richiede elevata flessibilitá dei sistemi di produzione e assemblaggio. Una delle soluzioni piú interessanti consiste nell'idea di combinare le capacitá manuali di un operatore con le potenzialitá tipiche di sistemi robotici per consentire una collaborazione efficace. Al giorno d'oggi, in ambiente industriale, lo spazio operativo in cui operano sistemi ad elevata automazione é marcatamente separato dallo spazio operativo in cui puó muoversi un operatore umano, tuttavia le recenti normative prevedono la possibilitá che questi due soggetti collaborino all'interno di uno spazio condiviso. Sulla base di un'approfondita ricerca bibliografica, in cui é emerso l'elevato interesse da parte della comunitá scientifica e industriale nelle applicazioni di cooperazione uomo-robot, abbiamo deciso di analizzare il problema della movimentazione di carichi in ampi spazi di lavoro per l'asservimento agli operatori. I robot collaborativi presenti sul mercato sono tipicamente caratterizzati da carichi trasportabili e spazi di lavoro ridotti che ne riducono il potenziale impiego. Tali aspetti possono superare i pregi dovuti alla collaborazione e renderla inefficace. L'obiettivo del progetto é, quindi, lo studio ed il progetto funzionale di sistemi meccatronici innovativi capaci di incrementare lo spazio operativo e la versatilitá del sistema con lo scopo finale di creare una collaborazione uomo-robot efficace. Considerando le grandi aree di lavoro, la possibilitá di operare in ambienti industriali in cui possono essere presenti ostacoli e l'elevato carico utile che potrebbe essere necessario, i robot cavi rappresentano una valida soluzione. Inoltre, la possibilitá di riconfigurare rapidamente il sistema (online oppure offline) e la loro semplicitá costruttiva li rende attraenti anche dal punto di vista economico.

Il lavoro svolto durante il percorso di dottorato ha permesso di individuare due soluzioni innovative di robot a cavi capaci di ingrandire lo spazio di lavoro, aumentare la versatilitá le sistema e ridurre i rischi di collisione. La prima soluzione consiste in un robot a cavi sospeso con end-effector riconfigurabile mentre la seconda soluzione é un innovativo modello di Micro-Macro Robot attuato a cavi. Sono stati sviluppati ed analizzati i modelli cinematici e dinamici di questi sistemi con l'obiettivo di caratterizzarne le proprietá. Inoltre, sono stati affrontati i problemi di pianificazione della traiettoria e di ottimizzazione del sistema.

Per dimostrare le enormi possibilitá caratterizzanti i robot a cavi, é stato sviluppato un software di progettazione. Tale software é caratterizzato da un simulatore con il quale é possibile configurare rapidamente il layout di un robot a cavi e valutarne le prestazioni in termini di prestazioni cinematiche e dinamiche. Inoltre é possibile simulare movimenti e valutare eventuali collisioni con gli ostacoli presenti nell'ambiente operativo. Il simulatore é stato realizzato con lo scopo di sviluppare una nuova famiglia di robot a cavi intelligenti (ICABOT, Intelligent CAble RoBOT) la cui architettura é concepita per massimizzare la versatilitá del sistema rispetto al compito da esguire e all'ambiente in cui deve operare. Un prototipo in ICABOT é stato sviluppato presso il laboratorio di Robotica dell'Universitá di Padova. Tale prototipo é costituito da componenti meccanici modulari e da un'architettura di controllo EtherCAT basata sulle piattaforme Matlab e Twincat 3.

ACKNOWLEDGMENTS

Undertaking the Ph.D. has been a truly life-changing experience for me that it would not have been possible without the support and guidance I received from many people. I have learned to pose questions and to find answers, but most importantly, I have learned to take the best from the people who surround me.

The research presented in this thesis has been carried out at the Department of Management and Engineering(DTG), University of Padua (Italy), and, partially, at the Robotics And Rehabilitation Laboratory (ROAR), Columbia University (New York, USA). First and foremost, I would like to express my gratitude to those who have helped to develop the results presented in this thesis. I am particularly grateful to my supervisor, Professor A. Rossi for his continued encouragement and to Professor G. Rosati for his fundamental suggestions and valuable contributions to this work. I am also thankful for his confidence in me. Furthermore, I am deeply grateful to Professor R. Caracciolo, who coordinates the doctoral school in Mechatronics and Product Innovation Engineering. I would also like to acknowledge Professor S. K. Agrawal for his hospitality at the Robotics And Rehabilitation Laboratory, and for the help he provided in the design of robotic systems. The joy and enthusiasm he has for his research was contagious and motivational for me. Special thanks also to Professor D. Zanotto for his constructive comments and the invaluable suggestions he gave me. I am also thankful for the excellent example he has provided as a researcher. Special thanks to the members of ROAR laboratory for their precious contributions.

I gratefully acknowledge the funding sources that made my Ph.D. work possible. My work was funded by the department of Management and Engineering of the University of Padua and the Italian Ministry of Education, Universities and Research. I also gratefully acknowledge the support from the Fondazione Ermenegildo Zegna, whose grant has funded my research period in the US.

I would like to thank all the Ph.D. candidates at the DTG department, my colleagues Fabio and Simone for the assistance they provided during these three years, and the two students who collaborated to the development of the ICABOT prototype. My time in New York was made enjoyable in large part due to the many friends and groups that became a part of my life. I am especially grateful to Haohan, Rosie, Luca, Julia, Alessandro, Fabio and Veronica. A very special thank you to Riccardo because he has been my first reference frame.

Finally, I want to thank my Mum, my Brother, Anna, Francesca and Antonio for their encouragement and support. This thesis is also yours. And most of all, I want to thank my loving and patient girlfriend Sara whose faithful support during all the Ph.D. was invaluable. She is simply the one who completes me. Our future is bright.

CONTENTS

1 INTRODUCTION

1.1 HUMAN-ROBOT COLLABORATION

In recent years major changes in the world of goods manufacturing have occurred, such as worldwide competition, advanced manufacturing process technologies and new manufacturing system structures [1]. Manufacturing enterprises should design and control their production systems so that they can quickly and economically adapt to unpredictable conditions, such as varying volumes and costs [2], and automation is usually a way to lower the costs of labour in Western countries [3]. Although automated systems have attracted significant attention over the years, a significant amount of tasks in various manufacturing industries still require the flexibility and adaptability of a human operator. In fact some processes require high levels of dexterity and judgment from human operators. Therefore, in certain manufacturing processes, the traditional vision of full automation is difficult to achieve. In these processes the desire to appropriately integrate automated systems (e.g. robots) and humans to collaborate in the same workspace has become an attractive solution. Thus, the emerging concept being sought is industrial human-robot collaboration (HRC) [4]. The motivation behind this concept is to alleviate the human weaknesses with the strengths of a robot and vice versa as shown in 1. For instance, humans lack accuracy, repeatability, speed and strength, while robots are very accurate and do not suffer from fatigue. Also, industrial HRC can enhance the ergonomics of the work place by delegating heavy, repetitive and sometimes dangerous tasks to the robots. As a result the support of humans by robotic system can lead, on the one hand, to more ergonomic work places and, on the other hand, to more time-efficient production processes.

For example human operators are the optimal solution in case of assembly systems with low productivity and low batch dimensions as shown in Fig. 2. On the contrary, when high productivity and high batch dimensions are required, automation is the only way to reduce the unit direct production cost. In fact the costs of task-adequate robots and the effort to set-up, program, and integrate them into existing production lines amortize only with a large number of manufactured products and a low number of variants, because the costs of the integration of a robot are approximately ten times the price of the robot itself.

The flexibility required by the market nowadays is hardly reachable with fully automated assembly systems [5], but human-robot collaboration has the potential to bridge the gap between fully-automated systems and fully manual workstation [6]. The advantage of an effective human-robot collaboration is only in early stages and needs further research to reach safe, robust and efficient realization.

The flexibility and adaptability obtained through human-robot collaboration allows constantly changing production environments as well as the manufacturing of highly customized products in the so called *factories of the future* [7]. As a result HRC is a key-feature of the next industrial revolution called *Industry 4.0* [8] and represents an opportunity for researchers and enterprises.

1.2 STATE OF THE ART

A significantly amount of research has been carried out in the area of physical human-robot interaction (pHRI) for assistive [9, 10, 11] and rehabilitation purposes [12, 13, 14]. Recently the interest of HRI for industrial applications has increased and many researchers, especially over the last few years, have proposed human-robot cooperation as a response to the flexibility–productivity trade-off problem. The following section aims at presenting an overview of the systems that have been introduced in the past to tackle human-robot collaboration in industrial environments.

Kosuge et al. [15] introduced in 1994 a robotic system consisting of multiple impedance-controlled robots. With this system the operators are able to command the motion of a manipulated object by applying the force to the object in coordination with the robots. The robots, supporting the most part of the load of the object, move the object as commanded by the humans.

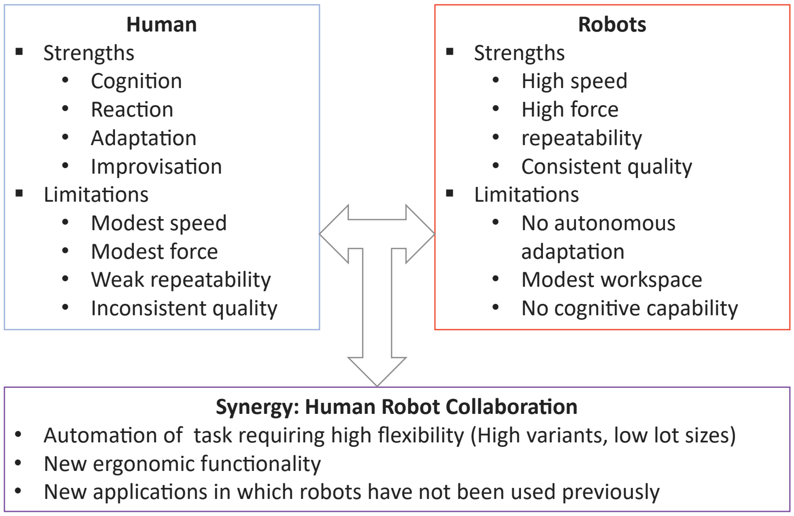

Figure 1: Synergy of Human-Robot Collaboration

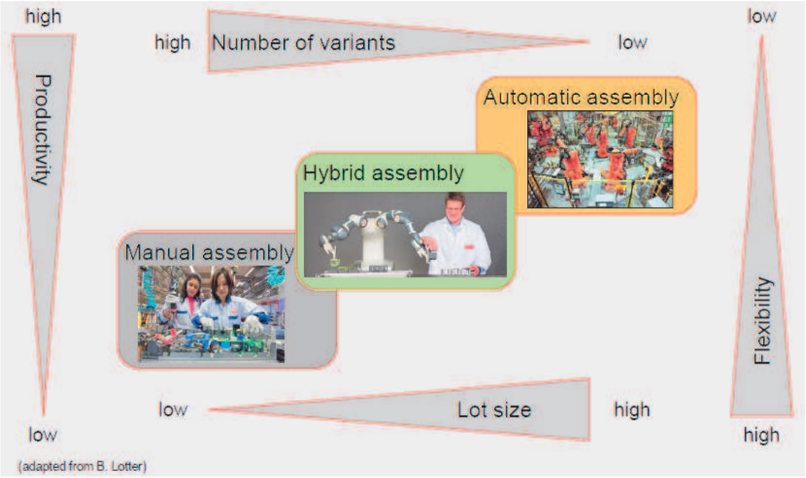

Figure 2: Convenience location of hybrid assembly compared to manual assembly and automatic assembly (adapted from B. Lotter).

Colgate et al. [16] introduced a class of systems named *cobots* that consist of robotic devices which manipulate objects in collaboration with human operators. These devices provide assistance to the human operators by setting up virtual surfaces which can be used to constrain and guide motions. Compared to conventional servo-actuated haptic devices, which are typically active and can supply energy to the human operator, *cobots* are intrinsically passive. This is because *cobots* do not use servos to implement constraint, but instead employ steerable nonholonomic joints. As a consequence of their passivity, *cobots* are potentially well-suited to safety-critical tasks (e.g. surgery) or those which involve large interaction forces (e.g. automobile assembly).

Kathib [17] presented several strategies to support operators in case of compliant motion and cooperative manipulation between multiple platforms. In addition to the controlling of multiple arms corresponding to the applied forces, multiple holonomic mobile platforms were coordinated to have a fully flexible mobile assistant.

Schraft et al. [18] presented *PowerMate*, which is a robotic assistant for handling and assembly task. The system is able to modify the robot velocity based on the working conditions: normal velocity if no human is present, limited velocity if the system detects the presence of human. The system has been also one of the first robots to implement the so called *teaching by demonstration*. In fact it is equipped with force/torque sensors that allow the operator to pull the robot on its gripper to a desired position.

Krüger et al. [6] studied the close cooperation of human and machine in hybrid assembly. The effectiveness of these systems depends on the lot size, but also on the design of the cooperative workplace and its automated systems. The overall effectiveness of hybrid assembly also depends on the intelligent feeding of workpieces to the cooperative workplace.

Takata et al. [19] proposed a human-robot allocation planning method for hybrid systems. The method allows the selection of an initial allocation pattern that can potentially minimize the total production cost, taking into account the changes in the product models and the volumes demanded in the future.

Morioka and Sakakibara [20] described a cell production assembly system with human–robot cooperation in order to increase operator productivity and reliability. This system consists of three key technologies: parts feeding by double manipulators on a mobile base, production process information support for the operator and safety management for the cooperation between the operator and the robot.

Medellin et al. [21] investigated automatic assembly planning for robot and manual assembly. They use the octree decomposition technique to generate robot and manual assembly plans. Other recent contributions on human-robot cooperation are available also in different manufacturing technologies, for example in constructing metallic structures [22] or casting processes [23].

Michalos et al. [24] investigated multiple aspects of safety that should be considered during the design and deployment of human-robot collaborative work cells. The authors defined the main variables that influences hybrid systems such as type of robot, robot's payload, power/force to apply, part's characteristics and manufacturing process.

Haddadin et al. [25] presented two collision detection algorithms and several reaction strategies were presented and extensively validated by experiments. The methods proposed allowed the robot to detect and distinguish unexpected collisions from an intended cooperation, in which a human stretching out his arm tries to catch the robot.

Corrales et al. [26] presented a human-interaction system which can be used to develop collaborative tasks between human operators and robotic manipulators in industrial environments. The main components of this system were a human tracking system and a robot controller based on human-robot distance. This system was successfully applied in three different assembly and disassembly tasks in order to show its applicability.

Pedrocchi et al. [27] proposed a safe-network of unsafe devices where the network architecture should allow the achievement of high-safety standards in terms of functional performance and of the necessary versatility and expandability in order to integrate nodes devoted to the elaboration of collision avoidance algorithms. The authors presented a particular collision avoidance strategy to be implemented in standard IR controllers. The set-up demonstrated the feasibility of the suggested approach and the experimental results show that safe collaborative workspace can be guaranteed with current standard industrial robot and IR controllers.

Schmidt and Wang [28] presented an integrated and cost-effective approach for real-time active collision avoidance in a human-robot collaborative work cell that enables all time safety protection. This approach connects virtual 3D models to a set of motion and vision sensors for real time monitoring and collision detection in augmented virtuality, aiming to improve the overall manufacturing performance

Flacco et al. [29] presented a new collision avoidance method for robot manipulators equipped with an exteroceptive depth sensor. The core of the algorithm is an innovative approach to evaluate the distances between the robot and the dynamic obstacles in its workspace, based only on simple and efficient computations on depth space data. These distances are used to generate repulsive vectors which are processed so as to obtain smooth and feasible joint velocity commands that avoid obstacles.

Morato et al. [30] presented a separation monitoring framework that allows a robot and human to safely collaborate and achieve shared tasks in assembly cells. The authors designed an N-Kinect framework to generate a 3D model of human's movements in real-time and rapidly evaluate human-robot interference in 3D Euclidean space by using a physics-based simulation engine.

To successfully integrate collaborative robots in an industrial process, the psychological research on cognitive process during human-robot interaction is fundamental. Arai et al. [31] assessed the mental strain of HRC through physiological measurements. The experimental results indicate that operators feel high mental strain when a robot moves near to them and the recommended distance from the robot to the operators should be more than 2.0 m. Furthermore, the moving speed towards a human operator should be less than 500 mm/s and it is recommended for a human operator to be notified of robot motions before it moves.

Despite the expected benefits of industrial HRC and the extensive research on this field, close collaboration of humans and robots in industry has been prevented largely due to safety concerns. Any device or machine, to be freely marketed within the European Community countries, shall meet the requirements of EU directives. They establish the general principles that the builders must follow to put on the market products that are not dangerous for the operators. The UNI EN ISO 10218 [32, 33] specifies requirements and guidelines for integrated safe design, protective measures and information for the use of industrial robots.

Given the variable nature of the hazards of the different uses of industrial robots, the first part of ISO 10218 [32] specifies requirements and guidelines for the inherent safe design, protective measures and information for use of industrial robots. It describes basic hazards associated with robots and provides requirements to eliminate, or adequately reduce, the risks associated with these hazards.

The second part of ISO 10218 [33] has been created in recognition of the particular hazards that industrial robot systems present when integrated and installed in industrial robot cells and lines. Hazards are frequently unique to a particular robot system. The number and types of hazards are directly related to the nature of the automation process and the complexity of the installation. The risks associated with these hazards vary with the type of robot used, its purpose and the way in which it is installed, programmed, operated and maintained.

1.3.1 *Design requirements for collaborative Robots*

The first part of [32], in addition to reporting the general safety requirements for industrial robots, describes the design requirements of a system capable of cooperating with an operator.

Robots designed for collaborative operation shall provide a visual indication when the robot is in collaborative operation and shall comply with one or more of the following requirements. The robot shall stop when a human is in the collaborative workspace and the stop function shall comply with the robot stopping functions defined in [34] and [32]. The robot may resume automatic operation when the human leaves the collaborative workspace. Alternatively, the robot may decelerate, resulting in a category 2 stop in accordance with IEC 60204-1 [34]. Once stopped, this standstill shall be monitored by the safety-related control system. Fault of the safety-rated monitored stop function shall result in a category 0 stop.

During the collaboration, the robot shall maintain a determined speed and separation distance from the operator. These functions may be accomplished by integral features or a combination of external inputs. Detection of the failure to maintain the determined speed or separation distance shall result in a protective stop as defined in Sec. 5.5.3 of [32] whereas the speed and separation monitoring functions shall comply with Sec. 5.4.2 of [32]. Furthermore, the power or force limiting function of the robot shall be constantly monitored and, if any parameter limit is exceeded, a protective stop shall be issued.

It is important to point out that the robot is simply a component in a final collaborative robot system and is not in itself sufficient for a safe collaborative operation. The collaborative operation applications are dynamic and shall be determined by the risk assessment performed during the application system design. Information for use shall contain direction for implementing speed values and separation distances. The second part of ISO 10218 [33] shall be used for designing collaborative operations.

1.3.2 *Safety requirements for the integration of collaborative robots*

The second part of ISO 10218 [33] specifies safety requirements for the integration of industrial robots and industrial robot systems as, defined in [32], and industrial robot cell(s). The integration includes the following:

- the design, manufacturing, installation, operation, maintenance and decommissioning of the industrial robot system or cell;
- necessary information for the design, manufacturing, installation, operation, maintenance and decommissioning of the industrial robot system or cell;
- component devices of the industrial robot system or cell.

The norm defines a *collaborative robot operation* as a collaboration between a person and a robot sharing a common workspace. It is only:

- used for predetermined tasks;
- possible when all required protective measures are active;
- for robots with features specifically designed for collaborative operation complying with ISO 10218-1 [32].

Due to the potential reduction of the spatial separation of human and robot in the collaborative workspace, physical contact between the human and the robot can occur during the operation. Protective measures shall be provided to ensure the operator's safety at all times. The norm defines the requirements to be fulfilled:

- The integrator shall conduct a risk assessment that must consider the entire collaborative task and workspace, including the characterization of:
  1. robot characteristics (e.g. load, speed, force, power);
  2. end-effector hazards, including the workpiece (e.g. ergonomic design, sharp edges, protrusions, working with tool changer);
  3. layout of the robot system;
  4. operator location with respect to proximity of the robot arm (e.g. prevent working under the robot);

5. operator location and path with respect to positioning parts, orientation to structures (e.g. fixtures, building supports, walls) and location of hazards on fixtures;
6. fixture design, clamp placement and operation, other related hazards;
7. design and location of any manually controlled robot guiding device (e.g. accessibility, ergonomic, etc.);
8. application-specific hazards (e.g. temperature, ejected parts, welding splatters);
9. limitations caused by the use of necessary personal protective equipment;
10. environmental considerations [e.g. chemical, radio frequency (RF), radiation, etc.];
11. performance criteria of the associated safety functions.

- Robots integrated into a collaborative workspace shall meet the requirements of ISO 10218-1.
- Protective devices used for presence detection shall meet the requirements defined in Sec. 5.2 of [33].
- Additional protective devices used in a collaborative workspace shall meet the requirements of [33].
- The safeguarding shall be designed to prevent or detect any person from advancing further into the safeguarded space beyond the collaborative workspace. Intrusion into the safeguarded space beyond the collaborative workspace shall cause the robot to stop and all hazards to cease.
- The perimeter safeguarding shall prevent or detect any person from entering the non-collaborative portion of the safeguarded space.
- If other machines, which are connected or attached to the robot system and present a potential hazard, are in the collaborative workspace itself then the safety-related functions of these machines shall comply, at a minimum, with the requirements defined in Sec. 5.2 of [33].

Moreover, the design of the collaborative workspace shall be such that the operator can easily perform all tasks and the location of equipment and machinery shall not introduce additional hazards. Safe-rated soft axes and space limiting should, whenever possible, be used to reduce the range of possible free motions.

To successfully integrate collaborative assembly systems in today's processes, high demands regarding safety, efficiency, ergonomics, flexibility, programmability and adaptability need to be met. The new safety regulations on human-robot collaboration [32, 33] and the extensive research on this field, have created the basis for a new generation of collaborative robots for industrial applications. The next section aims at presenting an overview of some collaborative robots available in the market.

1.4 COLLABORATIVE ROBOTS FOR INDUSTRIAL APPLICATIONS

According to the International Federation of Robotics (IFR) [35], since 2010, the demand for industrial robots has accelerated considerably due to the ongoing trend toward automation and the continued innovative technical improvements of industrial robots. Between 2010 and 2014 the average robot sales increase was at 17% per year.

Robot manufacturers and automated system integrators are continuously working to improve the performance of their systems. Human-robot collaboration has the potential to increase productivity and improve the working condition of the operators generating value along the production process. Several manufacturers propose collaborative robots in their catalogs. Kuka presented a 7-axis lightweight robot (Fig. 3a) with integrated joint torque sensors [36]. This lightweight robot is especially designed for interaction with unknown environements and with humnas. The robot can adapt to its environement and can also adapt its motion by 'learning' from previous experiences. Haddadin used this arm to build a sensor-based robotic co-worker for a safe and close collaboration and presented strategies for safe interaction with humans [37]. Fanuc [38] presented the collaborative robot with the largest payload in the industry combined with the largest reachable workspace.(Fig. 3b). The robot is a regular industrial robot mounted on a big force torque sensor and covered with a rubberized skin. This allows it to detect forces (FT sensor) as well as reduce force impact and pinch points (rubber skin). To further increase the reachable workspaces and the versatility of industrial robots, some companies proposed solutions characterize by dual-arm collaborative robot (Fig. 4a). ABB [39] has developed YuMi (Fig. 4b), a collaborative dual arm conceived for small parts assembly that includes flexible hands, parts feeding systems and camera-based part location. However, the low payload (0.5 kg per arm) limits the range of applications.

All the solutions previously presented are traditional industrial robot equipped with torque sensors. These solutions are characterized by small payload and small reachable workspace that reduce the range of possible applications. These drawbacks can overcome the advantages related to a collaborative task and make the collaboration not effective. This work aims at analyzing innovative mechatronic solutions capable of creating effective collaborations with humans while increasing the workspace and the versatility of the system.

(a) (b)

Figure 3: Kuka LBR iiwa(a) and Fanuc CR-35iA(b).

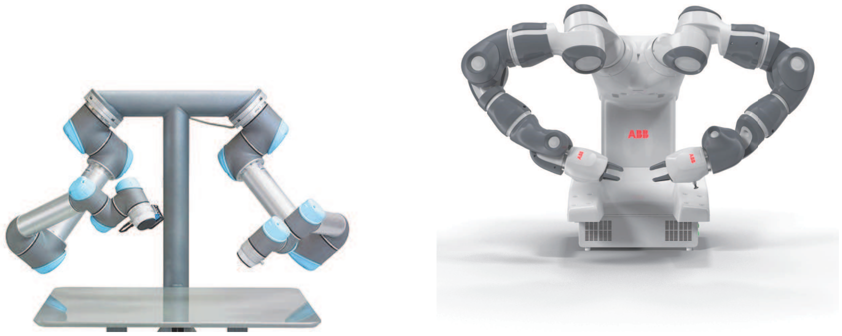

(a) (b)

Figure 4: Universal Robot (a) and ABB YuMi (b).

1.5 AIM OF THE WORK

The aim of this research is the design of mechatronic systems able to work inside large workspaces and safely collaborate with human operators. The main research questions of this study can be summarized as follows:

1. Which is the best design technology for mechatronic systems able to work inside a large workspace and guarantee high levels of versatility?
2. Is it possible to design a system able to avoid obstacles and/or collaborate with human operators?
3. Which is the optimal design of such a system?

The work presented in this dissertation aims at answering these questions and the starting point is an overview of the most common robotic solutions for industrial applications.

1.6 ROBOTIC SYSTEMS FOR INDUSTRIAL APPLICATIONS

This section aims at presenting an overview of robotic systems employed for industrial applications, characterizing their advantages and disadvantages. The goal is to address the first research question and identify the most appropriate technology for mechatronic systems able to work inside large workspaces and guarantee high levels of versatility.

When designing new robotic devices, some of the most important requirements that designers must take into account are: cost-effectiveness, force capability, dynamic performances, capability of handling large workspaces, repeatibility, versatility and safety [40]. Moving loads is a common task in industrial automation and several robotic solutions with different features are available as shown in Fig. 5.

The capability of moving heavy objects over large workspace is typical of crane-type structures (Fig. 6). Gantry cranes are used to load and unload containers in ship and trains whereas tower cranes and mobile cranes are employed in building construction. Those systems are energetically efficient; however, the underconstrained nature of

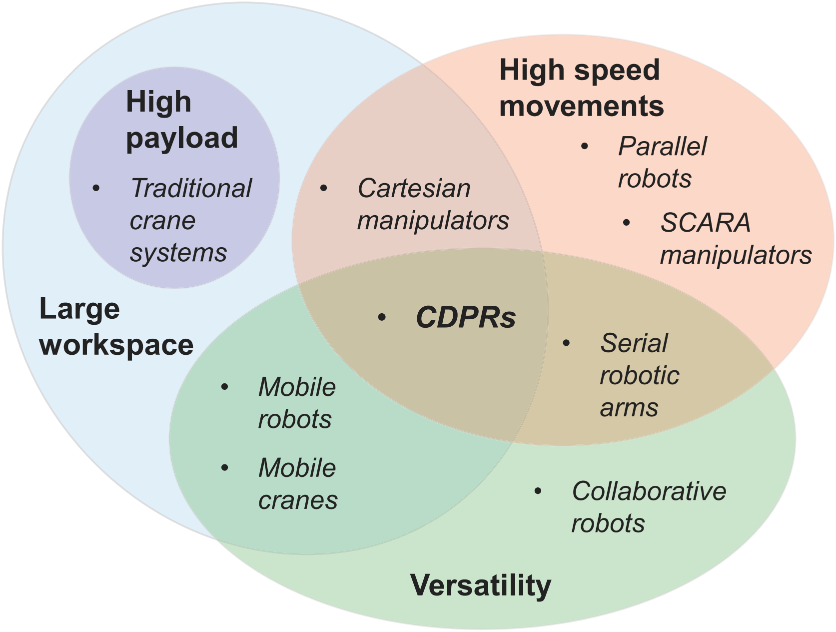

Figure 5: Industrial robots: a comparison based on workspace, speed, versatility and payload.


(a) (b)

Figure 6: Gantry crane (a) and Mobile crane (b).

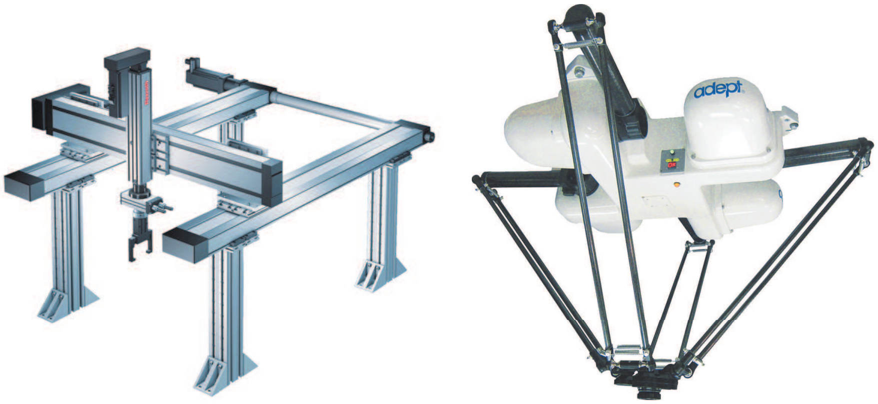

(a) (b)

Figure 7: Cartesian manipulator (a) and Parallel robot (Adept Quattro)(b).

the cranes makes them difficult to control forcing a quasi-static control of the load.

Cartesian manipulator (Fig. 7a) are mechatronic devices that use motors and linear actuators to position a tool. They make linear movements in three axes, x,y,z, and they can work over medium-large workspaces. Due to their rigid structure, these robots can manipulate relatively high loads so they are often used for pick-and-place applications, machine tool loading and stacking parts into bins. The main disadvantages of a cartesian manipulator is that it takes too much space comapared to the useful workspace and that it is not reconfigurable.

Parallel robots (Fig. 7b), also referred as Delta robots, are best suited for high speed pick-and-place applications with relatively light loads. The versatility of this robot is very low since it cannot handle variable orientation of the end-effector.

Serial robots (Fig. 3) have a number of links connected in series by rotational joints. These robots are very versatile and are used in ap-

(a) (b)

Figure 8: SCARA robot (Epson G6) (a) and AGV (Amazon warehouse) (b).

plications ranging from welding to machine tending where the robot arm reaches into a machine to grab a finished part, takes it out, and places it into the next part of the process. Some 6-Axis robots can be mounted in various orientations including wall mounted and ceiling mounted. On the other hand, the available workspace is typically small.

SCARA robots (Selective Compliant Assembly Robot Arm) are 4-DOF robots that have two revolute joints and a rotating prismatic joint (Fig. 8a). SCARA robots have limited movements but it is also its advantage as it can move faster than a 6-axis robot. They are mostly used in applications that require fast, repeatable and articulate point to point movements such as palletizing, machine loading/unloading and assembly. Its disadvantages are that it has limited movements and it is not very versatile.

A mobile robot is an automated machine that is capable of locomotion and it can rely on guidance devices that allow it to navigate in complex environments. Automated guided vehicle (AGV) are most often used in industrial applications to move materials around a manufacturing facility or warehouse as shown in Fig. 8b. The main disadvantage that characterizes a mobile robot is the low speed of the movements.

Recently, a new class of robotic devices has increased the interest of researchers: Cable-Driven Parallel Robots (CDPRs). CDPRs represent a particular class of parallel robots whose links are cables; they have been extensively studied in the past twenty years but their appealing advantages still make them a promising field of research [41]. In fact, compared to rigid serial and parallel robots, they have several advantages such as large workspaces, high payloads per unit of weight, ease of construction, versatility and affordable costs [42].

Thus, applications that require a combination of such features are good candidates for the use of CDPRs (Fig. 5).

As a result, the possibility to design CDPRs able to operate over large workspaces and guarantee high level of flexibility as well as high performance is the driving factor of this thesis and an overview of the dissertation is presented in the next section.

1.7 OVERVIEW OF THE DISSERTATION

Aiming to address the scientific and technical questions raised in Sec. 1.5, this dissertation presents the design of CDPRs conceived to avoid obstacles and/or collaborate with human operators. The design of cable systems conceived for human-robot collaboration is a first novelty of this work. The subsequent chapters of this dissertation are organized as follows.

Chapter 2 introduces the design of CDPRs through a literature review and a comprehensive description of the kinematic and dynamic models. The possibility to evaluate the performance of CDPRs is described through the concepts of manipulability and performance indices. Adaptive and reconfigurable cable-driven parallel robot are presented in order to introduce two innovative designs of end-effector for CDPRs. The first solution consists of a reconfigurable end-effector whereas the second solution is an innovative model of micro-macro robot.

Chapter 3 presents the model of a suspended CDPR for pick and place applications that has the capability of modifying the position of the anchor points of the cables to the end-effector. Furthermore, a novel trajectory planning algorithm for pick and place applications is presented. Finally the optimal design of a 7-DOF CDPR with reconfigurable end-effector is proposed.

An innovative model of cable-based micro-macro robot is introudec in Chapter 4. The system consists of a cable suspended parallel robot whose end-effector is a two-link passive serial manipulator. The system is under-actuated but it can be controlled using the differential flatness paradigm. Finally, a novel design approach based on multi-objective optimization and optimal control is illustrated.

Chapter 5 illustrates the design of a novel family of Intelligent CAble-driven paralle roBOTs (ICABOTs) whose architecture and control will maximize the robot adaptability to the task to be performed and the environment in which the robot is intended to operate.

Conclusion and future work are presented in Chapter 6.

2

DESIGN OF CABLE ROBOTS

This chapter presents a brief introduction on cable-based systems. The related literature is outlined and a basic classification of cable-driven parallel robots as well as the main features of this class of robots are illustrated. Kinematic and dynamic models are derived for a generic CDPR. The concept of manipulability is addressed as well as the possibility to design adaptive and reconfigurable CDPRs to increase the performance of traditional CDPRs. Finally, two innovative solutions of CDPRs able to increase the workspace and avoid obstacles are presented.

2.1 CABLE DRIVEN PARALLEL ROBOTS

Cable driven parallel robots can be classified as fully constrained or under-constrained [42], based on the degree to which the cables determine the pose of the manipulator. In the fully constrained case the pose (position and/or orientation) of the end-effector can be completely determined given the current lengths of the cables (Fig. 9a). In contrast, under-constrained cable systems must rely on the presence of gravity to determine the resulting pose of the end-effector (Fig. 9b). Cable-Suspended Parallel Robots (CSPRs) are typical example of under-constrained systems. CDPRs can also be under-actuated (Fig. 9c), leading to pendulum-type mechanisms whose degrees of freedom are not all controlled [43, 44]. Under-actuated CDPRs also raise the interesting issue of the determination of their static pose for a given geometry of the attachment points and given cable lengths. This problem involves geometric and static conditions and leads to a set of very complex algebraic equations.

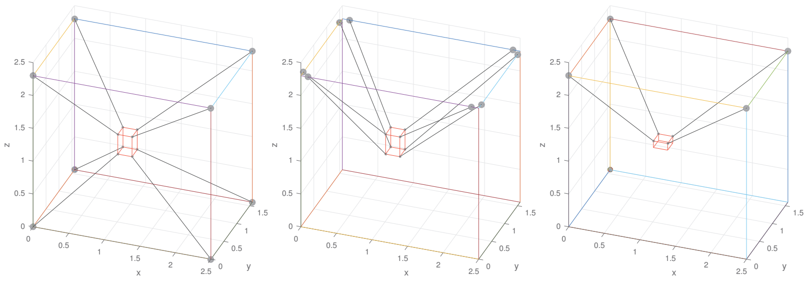

(a) (b) (c)

Figure 9: CDPR fully-constrained (a), CDPR under-constrained (b), CDPR under-actuated (c).

Several authors have proposed interesting prototypes of CDPRs in the last years. The most successful examples are represented by Skycam [45] (Fig. 10a) and NIST RoboCrane [46] (Fig. 10b). RoboCrane is a 6-dof crane used for lifting and positioning operations or to control position, velocity and force of tools and machinery for cutting or excavating tasks.

Holland and Cannon [47] first patented a suspended cable robot system which have the ability to precisely manipulate heavy loads, such as shipping containers over large workspaces (Fig. 11a). Pott et. al [48] introduced a prototype of fully-constrained CDPR for a large-scale process like the assembly of parabolic reflector panels (Fig. 12). Recently, Izard et al. [49] presented a prototype of suspended CDPR with a redundant actuated configuration (8 cables, 6 DOFs[1]) suitable for pick and place applications (Fig. 14b). An innovative large-scale CDPR has been developed by the Max Planck Insitute and the Fraunhofer IPA that is the first one capable of transporting humans while at the same time setting new standards in terms of workspace, acceleration and payload for a motion simulator (13a). The Arecibo Radio Telescope and the Five-hundred meter Aperture Spherical Telescope [50](Fig. 13b) are examples of large cable-suspended systems driven by cables.

Other important applications have been proposed in the field of rehabilitation robotics. The Feriba3 [51, 52], depicted in Fig. 15a, is a 4-wire planar CDPR with a circular end-effector and a square-shaped workspace. It was designed to be used as a general-purpose haptic display, i.e. a device capable of reproducing real and virtual environments by exerting a variable mechanical impedance to the user's hand. It exploits 4 driven cables to generate 3 generalized forces on a round-shaped end-effector. The end-effector position is imposed by the operator who perceives the force-feedback from the device. The direction and amount of force reflected depends on the end-effector

---

[1] Degrees Of Freedom.


(a) (b)

Figure 10: Skycam (a) and Robocrane (b).

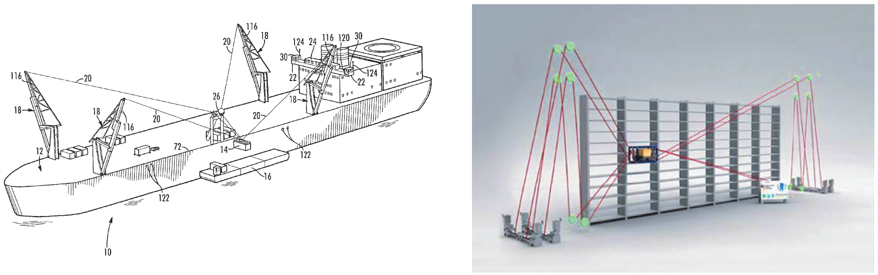

(a)

(b)

Figure 11: CSPR for containers shipping (a) and CDPR for storage applications (b).

position and on the specific remote or virtual environment represented.

PiRoGa5 is a cable-driven 5-DOF haptic display, with a pen-like shaped end-effector [53]. Six wires are attached to the end-effector, three to each end-point of the pen. Each wire is tensioned by a motor-pulley direct drive system allowing the operator to move the end-effector along six DOFs.

NeReBot (NEuro REhabilitation roBOT) [54] is a cable-suspended device for upper limb rehabilitation of post-stroke patients. Three nylon wires convert the rotating motion of three d.c. motors into a 3D trajectory of patient's arm. A real-time software performs both on-line point by point acquisition and repetition of the 3D trajectory obtained by interpolating the acquired points. This device was designed to target post-stroke patients in a very early stage (a few days after the stroke) and can be operated both at bed side or with wheel-chaired patients.

The evolution of NeReBot is MariBot (MARIsa roBOT), a 5 DOF cable-suspended robot for neurorehabilitation [55]. This robot is designed for post-stroke upper limb rehabilitation in the post-acute phase. Three nylon wires are used to sustain the forearm of the patient and produce motion in the vertical plane, while two additional

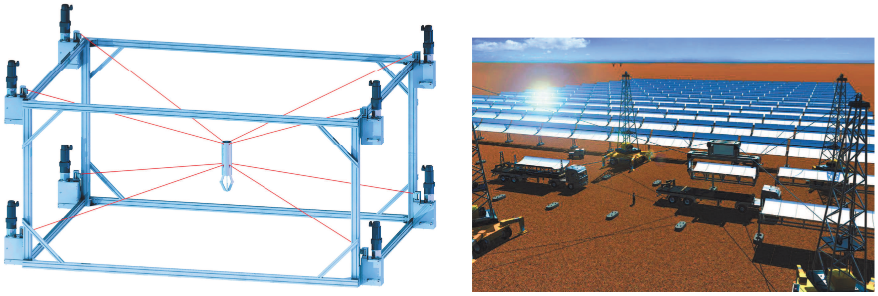

(a)

(b)

Figure 12: Ipanema (a) and Atlas (b).

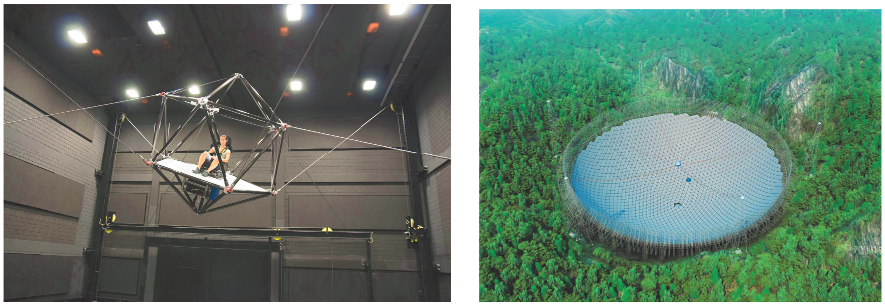

(a) (b)

Figure 13: Flight simulator (a) and Fast (b).

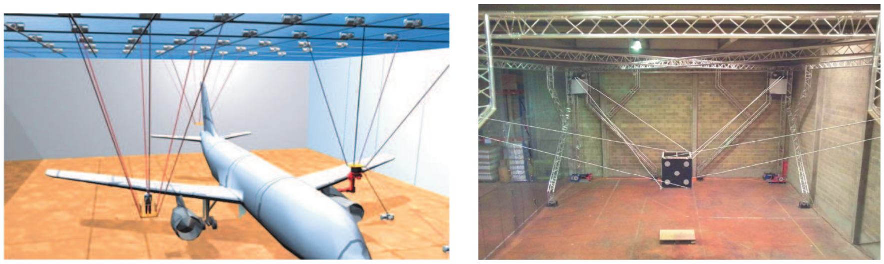

(a) (b)

Figure 14: CableBot (a) and CoGiRo (b).

(a) (b)

Figure 15: Prototype of cable robot developed at the University of Padua: Feriba (a) and Nerebot (b).

actuators move the overhead structure to adjust the cable configuration in the horizontal plane.

Recently, Vashista et al. [56] presented the prototype of a novel tethered pelvic assist device (T-PAD) that consists of springs and cables (Fig. 16b). TPAD provides pelvic support in the form of applied forces in any direction, including the direction of gravity. Additionally its tethers can also be configured to apply asymmetric forces on the pelvis. It is designed to assist in understanding issues of adaptation of forces applied during a gait cycle.

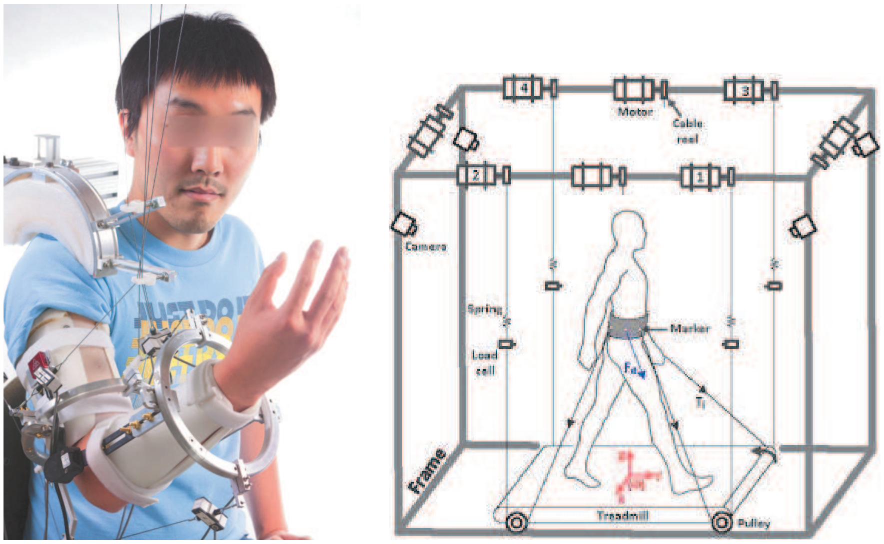

(a)

(b)

Figure 16: Prototype of cable robot developed at Columbia University: Carex (a) and TPAD (b).

Mao et al. [57] presented CAREX, a light-weight exoskeleton designed for the upper arm in which rigid links of the exoskeleton are replaced by lightweight cuffs attached to the moving limb segments of the human arm. Cables, driven by motors, are routed through these cuffs to move the limb segments. Because of this structure, it is nearly an order of magnitude lighter than conventional exoskeletons.

Thanks specifically to their advantages in terms of large workspaces and high payloads per unit of weight, CDPRs are particularly indicated for high speed manipulations and crane-like applications [47, 58, 59]. For such applications two types of CDPRs can be found: fully-constrained, if the pose of the end effector is completely defined by the lengths of the cables, and under-constrained suspended, when the end effector makes use of gravity to get a pose [60].

If compared to fully-constrained CDPRs, under-constrained Cable Suspended Parallel Robots (CSPRs) can reduce collision risks between cables and obstacles since the mobile platform is suspended with cables connected to the ceiling, making cable-free the workspace below the platform [61] (Fig. 14b). However, they rely on gravity to maintain the cables in tension [62]. In contrast to fully-constrained CDPRs, which have at least one pose that ensures force closure, gravity is fundamental to generate any type of force and momentum and the lack of the ability to exert a complete set of forces in the workspace generates control issues.

As it will be discussed in the following sections, the analysis and the optimization of the performance of a CDPR is a major topic in literature. The main aspects to address when dealing with cable-based systems are the workspace size, the manipulability, the dynamics and the control [42]. In the next section the kinematic and dynamic models of a generic CDPR are defined in order to characterize its performance.

2.2 KINEMATIC MODEL

Let us consider the model of a generic CDPR with n degrees of freedom (DOFs) and N cables as shown in Fig. 17.

The kinematic model of such a robot is represented by the relationship between the angular position of each pulley θ_i and the pose (position and orientation with Euler or RPY angles) of the end-effector with respect to the global reference frame [63]. Let the vector $\mathbf{x} = [x_G, y_G, z_G, \alpha, \beta, \gamma]^T$ represent the reference frame of the end effector in its center of mass, $\mathbf{x_P} = [x_P, y_P, z_P, \alpha, \beta, \gamma]^T$ in the tool center point. The former is used in the dynamic model; the latter for the trajectory planning of the robot movements. The two reference frames of the end effector are here defined with the same orientation so that they differ in a known translation only. The position of the tool center point P can be calculated as follows:

$$^{O}\mathbf{p} = {^{O}\mathbf{e}} + {^{O}\mathbf{q}} = {^{O}\mathbf{e}} + {^{O}_{G}\mathbf{R}}(\alpha, \beta, \gamma)\, {^{G}\mathbf{q}} \tag{1}$$

where ${^{O}_{G}\mathbf{R}}(\alpha, \beta, \gamma)$ is the rotation matrix from the global frame to the end effector frame in G.

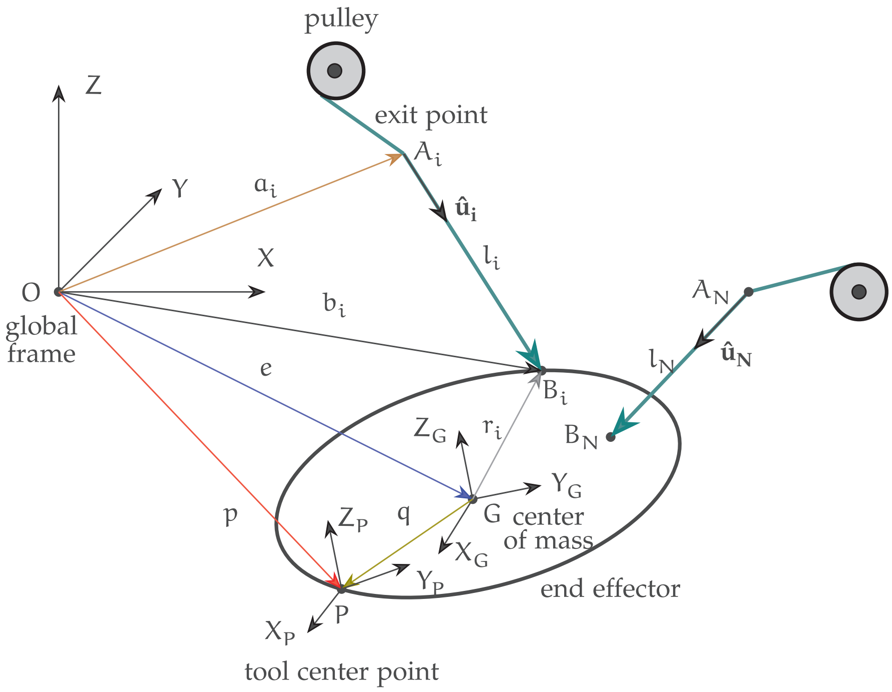

Figure 17: Model of a cable driven parallel robot (CDPR) with reconfigurable anchor points on end effector.

The cable vector is computed as the line segment between B_i and A_i, as follows:

$$^{O}\mathbf{l_i} = l_i \hat{\mathbf{u}}_\mathbf{i} = {}^{O}\mathbf{b_i} - {}^{O}\mathbf{a_i} \qquad i = 1, \dots, N \tag{2}$$

where

$$^{O}\mathbf{b_i} = {}^{O}\mathbf{e} + {}^{O}\mathbf{r_i} = {}^{O}\mathbf{e} + {}^{O}_{G}\mathbf{R}(\alpha, \beta, \gamma)\,{}^{G}\mathbf{r_i} \qquad i = 1, \dots, N \tag{3}$$

The inverse position kinematics problem is simply the calculation of the cable lengths $^{O}\mathbf{l_i}$ given the Cartesian position $\mathbf{x}$ (Eqs. 2 and 3). On the contrary, the forward position kinematics can be stated as: given the cable lengths $^{O}\mathbf{l_i}$, calculate the Cartesian position $\mathbf{x}$. This problem is typically over-constrained and authors proposed several algorithm to solve it [64, 65, 66].

The i^{th} angular position of each pulley is related to the distance of the i^{th} cable $l_i = \|\mathbf{l_i}\| = \|\mathbf{B_i} - \mathbf{A_i}\|$ by the following equation:

$$\theta_i = \frac{l_i - l_{i,0}}{r_{p_i}} \qquad i = 1, \dots, N \tag{4}$$

where r_{p_i} is the pulley radius and $l_{i,0}$ is the initial length of the i^{th} cable.

We can similarly define the angular velocity $\dot{\theta}_i$ and acceleration $\ddot{\theta}_i$ of the i^{th} pulley as follows:

$$\dot{\theta}_i = \frac{\dot{l}_i}{r_{p_i}} \tag{5}$$

$$\ddot{\theta}_i = \frac{\ddot{l}_i}{r_{p_i}} \qquad i = 1, \dots, N \tag{6}$$

where $\dot{l}_i$ and $\ddot{l}_i$ are the linear velocity and acceleration of cable i, which are related respectively to the velocity $^{O}\dot{\mathbf{x}}$ and acceleration $^{O}\ddot{\mathbf{x}}$ of the end effector by the following relations:

$$\dot{\boldsymbol{\theta}} = \frac{\partial \boldsymbol{\theta}}{\partial \mathbf{x}}\dot{\mathbf{x}} = \mathbf{J}\dot{\mathbf{x}} \tag{7}$$

where the Jacobian mattrix $\mathbf{J} \in \mathbb{R}^{\mathbf{6} \times \mathbf{6}}$:

$$\mathbf{J} = \frac{\partial \theta}{\partial x} = \begin{bmatrix} \frac{\partial \theta_1}{\partial x_1} & \frac{\partial \theta_1}{\partial x_2} & \cdots & \frac{\partial \theta_1}{\partial x_n} \\ \frac{\partial \theta_2}{\partial x_1} & \frac{\partial \theta_2}{\partial x_2} & \cdots & \frac{\partial \theta_2}{\partial x_n} \\ \vdots & \vdots & \vdots & \vdots \\ \frac{\partial \theta_N}{\partial x_1} & \frac{\partial \theta_N}{\partial x_2} & \cdots & \frac{\partial \theta_N}{\partial x_n} \end{bmatrix} \tag{8}$$

The inverse velocity problem (7) is solved directly with little effort using Eqs. 2, 3 and 4.

However, to solve the forward velocity kinematics problem, Eq. 7 must be inverted: $\dot{\mathbf{x}} = \mathbf{J}^{\#}\dot{\boldsymbol{\theta}}$. Due to redundant actuation, $\mathbf{J}$ can have different sizes and $\mathbf{J}^{\#}$ can be defined in different ways:

- If $N > n$, then $\mathbf{J}^{\#} = (\mathbf{J}^T\mathbf{J})^{-1}\mathbf{J}^T$
- If $N < n$, then $\mathbf{J}^{\#} = \mathbf{J}^T(\mathbf{J}\mathbf{J}^T)^{-1}$
- If $N = n$, then $\mathbf{J}^{\#} = \mathbf{J}^{-1}$

2.3 DYNAMIC MODEL

Let $\mathbf{W} = [F_x, F_y, F_z, M_x, M_y, M_z]^T$ be the resultant of all forces and moments acting on the end-effector [67]. The dynamic equation of the end effector, with respect to the center of mass, is given by:

$$\mathbf{M}\ \ddot{\mathbf{x}} = \mathbf{W} \tag{9}$$

where the Cartesian mass matrix $\mathbf{M} \in \mathbb{R}^{6\times 6}$ can be defined as a combination of the mass matrix $\mathbf{M_e}$ and the inertia matrix $\mathbf{I_e}$:

$$\mathbf{M} = \begin{bmatrix} \mathbf{M_e} & 0 \\ 0 & \mathbf{I_e} \end{bmatrix} \tag{10}$$

The resultant $\mathbf{W}$ can be expressed as the sum of two contributes: the forces exerted by the cables $\mathbf{W_{tens}}$ and the external wrench applied to the end effector $\mathbf{W_{ext}}$:

$$\mathbf{W} = \mathbf{W_{tens}} + \mathbf{W_{ext}} \tag{11}$$

where $\mathbf{W_{ext}}$ is the external wrench.

The relationship between the cable tension vector $\mathbf{T} = [T_1, \dots, T_N]^T$ and $\mathbf{W_{tens}}$ can be defined as follows [42]:

$$\mathbf{W_{tens}} = \mathbf{S}\ \mathbf{T} \tag{12}$$

where $\mathbf{S}$ is a $n \times N$ matrix called structure matrix and is defined as:

$$\mathbf{S} = \begin{bmatrix} -\hat{\mathbf{u}}_1 & -\hat{\mathbf{u}}_2 & \dots & -\hat{\mathbf{u}}_N \\ -\hat{\mathbf{u}}_1 \wedge \mathbf{r}_1 & -\hat{\mathbf{u}}_2 \wedge \mathbf{r}_2 & \dots & -\hat{\mathbf{u}}_N \wedge \mathbf{r}_N \end{bmatrix} \tag{13}$$

As a result, cable tensions and motor-torques are related by the equation:

$$\tau_i = r_{p_i} \cdot T_i \tag{14}$$

Finally, we can calculate the vector of torques exerted by the motors considering the combined motor shaft/cable pulley dynamics:

$$\boldsymbol{\kappa} = \mathbf{J_m}\ddot{\boldsymbol{\theta}} + \mathbf{C_m}\dot{\boldsymbol{\theta}} + \boldsymbol{\tau} r_p \tag{15}$$

where $\mathbf{C_m}$ and $\mathbf{J_m}$ are diagonal matrices with rotational inertia and rotational viscous damping coefficients on the diagonal. The angular acceleration $\ddot{\boldsymbol{\theta}}$ can be derived as follows:

$$\ddot{\boldsymbol{\theta}} = \frac{d}{dt}\left(\frac{\partial \boldsymbol{\theta}}{\partial \mathbf{x}}\right)\dot{\mathbf{x}} + \frac{\partial \boldsymbol{\theta}}{\partial \mathbf{x}}\ddot{\mathbf{x}} \tag{16}$$

The overall system dynamics model can be derived by combining the Cartesian dynamic equation (Eq. 9) and the actuator dynamic equation (Eq. 15). By substituting (Eq. 15) in (Eq. 16) we obtain:

$$\boldsymbol{\tau} = \frac{1}{r_p}\left(\boldsymbol{\kappa} - \mathbf{J_m}\left(\frac{d}{dt}\left(\frac{\partial \boldsymbol{\theta}}{\partial \mathbf{x}}\right)\dot{\mathbf{x}} + \frac{\partial \boldsymbol{\theta}}{\partial \mathbf{x}}\ddot{\mathbf{x}}\right) - \mathbf{C_m}\frac{\partial \boldsymbol{\theta}}{\partial \mathbf{x}}\dot{\mathbf{x}}\right) \tag{17}$$

Finally, by combining (9), (12) and (17) we obtain the overall dynamics equations of motions, expressed in a standard Cartesian form for robotic systems:

$$\mathbf{M_{eq}}(\mathbf{x})\,\ddot{\mathbf{x}} + \mathbf{N}(\mathbf{x},\dot{\mathbf{x}}) = \mathbf{S}(\mathbf{x})\,\boldsymbol{\tau} \tag{18}$$

where:

$$\mathbf{M_{eq}}(\mathbf{x}) = r_p\mathbf{M} + \mathbf{S}(\mathbf{x})\,\mathbf{J}\frac{\partial \boldsymbol{\theta}}{\partial \mathbf{x}} \tag{19}$$

$$\mathbf{N}(\mathbf{x},\dot{\mathbf{x}}) = \mathbf{S}(\mathbf{x})\left(\mathbf{J_m}\frac{d}{dt}\frac{\partial \boldsymbol{\theta}}{\partial \mathbf{x}} + \mathbf{C_m}\frac{\partial \boldsymbol{\theta}}{\partial \mathbf{x}}\right)\dot{\mathbf{x}} \tag{20}$$

2.4 MANIPULABILITY

A main issue when designing a cable-based system is to determine appropriate indices able to characterize its performance. Manipulability is a widely adopted index as a measure of the performance of a robotic system in the force domain, usually described by means of an ellipsoid or polytopes [68, 69, 70].

Equation (12) expresses the relationship between the resultant of all forces and moments acting on the end-effector and the cable tensions. To maintain the control of the end-effector, the tension of each cable must be positive. Due to motor torque capabilities, each component T_i of vector $\mathbf{T}$ is constrained by an upper bound T_{max_i}, so that a limited set of vectors $\mathbf{W_{tens}}$ can be obtained at the end effector that, in turn, means a limited $\mathbf{W}$. As a result, an actual system is not able to exert all the possible combinations of forces and moments.

If we consider a planar CDPR with a point-mass end-effector, only pure forces can be exerted, thus a single parameter can conveniently be adopted to characterize its manipulability. This can be the module of the maximum feasible isotropic force. The derivation of this index is straightforward in the case of planar translational CDPRs. Let us consider the cable system shown in Fig. 18 ($n = 2$, $N = 3$): the polygon that describes all the feasible forces at a given position is obtained by drawing along each cable a vector representing the maximum cable tension T_{max_i} and two lines passing by the tip of that vector parallel to the remaining cables. Clearly, the maximum isotropic force is given by the radius of the circle centered in G and tangent to the polygon. Since cable configuration varies as a function of end-effector position, different values are to be expected throughout the workspace. If gravity was present, its contribute would be

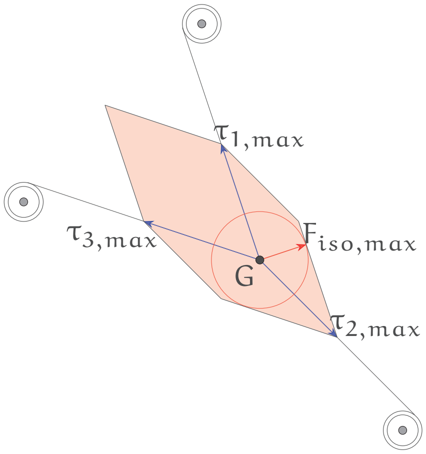

Figure 18: Example of planar CDPR with two DOFs ($n = 2$) and three cables ($N = 3$) with the set of feasible wrenches which is exertable by the robot and the geometric interpretation of the maximum allowable isotropic force.

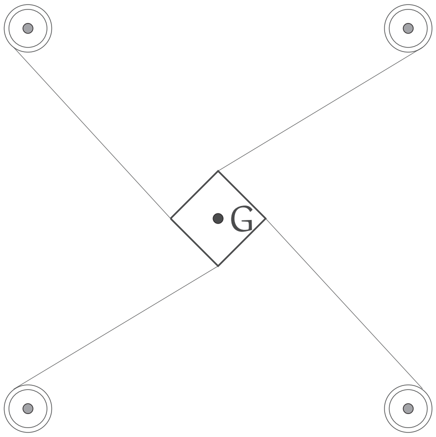

Figure 19: Example of planar CDPR with three DOFs ($n = 3$) and four cables ($N = 4$).

taken into account in the term containing the external wrenches $\mathbf{W_{ext}}$ that must be considered to calculate the set of forces obtainable by the system in the operational space.

In the case of complex CDPRs, with a generic end-effector that is laying inside the workspace, the set of available wrenches is a combination of forces and moments. It can be proved that, giving an arbitrary pure wrench (force or moment) that can be obtained in any available direction, there is only a limited set of wrenches which can be exerted [68].

In order to define the maximum allowable wrench for a CDPR we need to define the linear transformation related to the structure matrix:

$$\phi : \quad \mathbb{R}^{\mathbf{N}} \longrightarrow \mathbb{R}^{\mathbf{6}} \qquad \phi(\mathbf{T}) = \mathbf{ST} + \mathbf{W_{ext}} \tag{21}$$

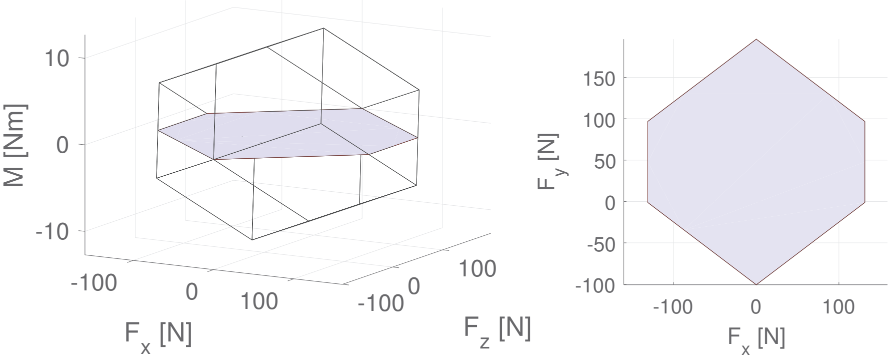

(a) (b)

Figure 20: Force polytope for the CDPR shown in Fig. 19. The wrench set with $M_z = 0$ is highlighted and the available combinations of F_x and F_y are represented (b).

Let $H_{T_{max}}$ be the set of the maximum tensions of the cables that the actuators can generate:

$$H_{T_{max}} = \left\{ \mathbf{T} \in \mathbb{R}^{\mathbf{N}} : \ 0 \leqslant T_i \leqslant T_{max_i} \ \ \forall i \right\} \tag{22}$$

We can calculate the projection of $H_{T_{max}}$ considering the transformation ϕ and obtaining the set of the generalized force that the system can exert to the end effector:

$$P_{\phi,T_{max}} = \left\{ \mathbf{W} \in \mathbb{R}^{\mathbf{6}} : \ \ \mathbf{W} = \phi(\mathbf{T}), \ \ \exists \mathbf{T} \in H_{T_{max}} \right\} \tag{23}$$

$P_{\phi,T_{max}}$ is a convex polytope since it is obtained from a linear transformation of an hypercube.

Figures 20, 21 and 22 illustrate the polytope obtained for the CDPR shown in Fig. 19 and highlight three particular wrench sets. Figures 20 is the set of forces F_x and F_y that can be obtained with a null moment ($M_z = 0$). Figures 21 represents the combination of force F_x and moment $M_z = 0$ that can be obtained with $F_y = 0$. Similarly, Figures 22 represents the combination of force F_y and moment $M_z = 0$ that can be obtained with $F_x = 0$.

The same approach can be used to define the maximum allowable velocities for the end effector of a CDPR [71]. The linear transformation that maps the velocities of the cables to the velocities of the end effector relies on the Jacobian matrix:

$$\psi : \mathbb{R}^{\mathbf{N}} \longrightarrow \mathbb{R}^{\mathbf{6}} \qquad \psi(\dot{\theta}) = \frac{\partial \boldsymbol{x}}{\partial \theta} \dot{\theta} = \mathbf{J} \dot{\theta} \tag{24}$$

where $\mathbf{J}$ is the Jacobian matrix.
Let $H_{\dot{\theta}_{max}}$ be the set of the maximum angular velocities that the actuators can generate:

$$H_{\dot{\theta}_{max}} = \left\{ \dot{\theta} \in \mathbb{R}^{\mathbf{N}} : \ 0 \leqslant \dot{\theta}_i \leqslant \dot{\theta}_{max_i} \ \ \forall i \right\} \tag{25}$$

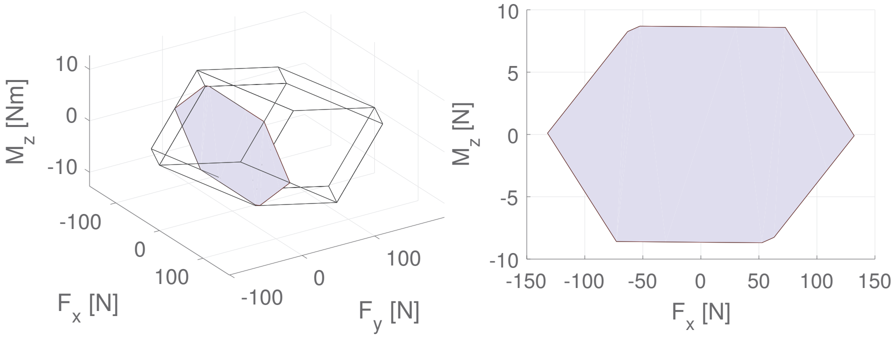

(a) (b)

Figure 21: Force polytope for the CDPR shown in Fig. 19. The wrench set with $F_y = 0$ is highlighted and the available combinations of F_x and M_z are represented (b).

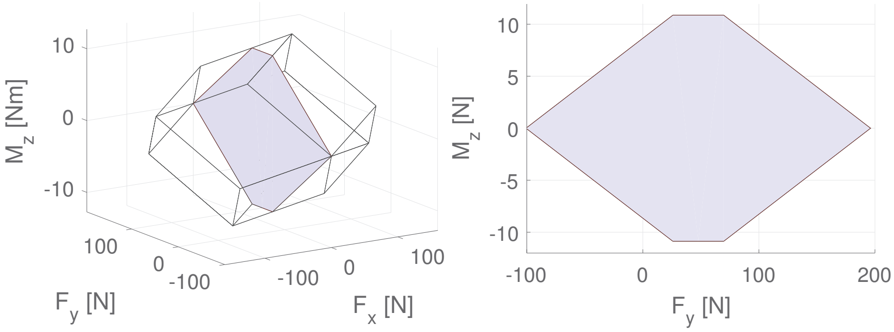

(a) (b)

Figure 22: Force polytope for the CDPR shown in Fig. 19. The wrench set with $F_x = 0$ is highlighted and the available combinations of F_y and M_z are represented (b).

We can calculate the projection of $H_{\dot{\theta}_{max}}$ considering the transformation ψ and obtaining the set of generalized velocities that the system can develop at the end effector:

$$P_{\psi,\theta_{max}} = \left\{ \dot{\mathbf{x}} \in \mathbb{R}^6 : \; \dot{\mathbf{x}} = \psi(\dot{\theta}), \; \exists \dot{\theta} \in H_{\dot{\theta}_{max}} \right\} \tag{26}$$

$P_{\psi,\theta_{max}}$ is a convex polytope since it is obtained from a linear transformation of an hypercube.

It is worth noticing that the maximum allowable forces (and velocities) depend on the pose of the end-effector, on the position of the cable exit points and on the position of the cable anchor points on the end-effector. Thus, the ability to reconfigure the cable-systems, by moving the cable anchor points or the cable exit points, allows the robot to change the force capability for a given pose of the tool center point. The next section aims at introducing a new class of cable systems defined reconfigurable cable robots.

Recently, researchers studied new types of CDPRs which can be reconfigured by changing their cable layout, which is usually intended as on-the-fly changing the position of cable anchor points to the environment. Reconfigurability offers more versitile choices to the end-user and should improve the performances of the system.

Rosati and Zanotto [72, 73] proposed a novel approach for the optimal design of adaptive cable-based system. To validate the approach empirically, the first prototype of Semi-adaptive device, called Sophia-3, was designed and developed (Fig. 23). This device was conceived as a cost-effective planar rehabilitation device to be employed in the decentralized health-care treatment of chronic post-stroke patients. Zhou et al. [74] enhanced the manipulability of a planar cable robot by the addition of base mobility to spooling winches and analyzed optimal strategies for tension distribution problems. Nguyen and Gouttefarde [75] presented an optimal reconfiguration strategy, based on the cable tensions and the robot energy consumption, for a suspended CDPR for conventional gantry nacelles that carry workers in an airplane maintenance workshop. Gagliardini et al. [76] introduced a reconfigurable CDPR able to change the locations of its cable exit points and presented a reconfiguration strategy based on the Dijkstra's algorithm.

An interesting point to address when a reconfigurable CDPR is specifically designed for pick and place applications regards the choice of the best cable configuration to make optimally the task required. In a standard scenario, pick and place movements consist of two main phases: the pick/release of a part, which particularly requires interaction with the environment such as a worker that waits the part or an obstacle; the robot transfer between two locations, which requires high performance in terms of movement time and quality. This means that when approaching an operator or an obstacle, the CPDR has to allow for a configuration of the cables that avoids collisions with the environment. On the other hand, during the transfer movement, the cables must exert the maximum performance. In fact, industrial automation aims at increaseing productivity throughout manipulators able to track the desired trajectory, with some possible constraints, in the shortest time [77, 78, 79, 80].

The next section aims at introducing two innovative designs of end-effector able to modify their configuration to reduce the cable interference, avoid obstacles and maximize the performance.

2.6 INNOVATIVE DESIGN OF END-EFFECTOR FOR CABLE ROBOTS

To date, no contributions are present in literature with the aim of studying end-effector for under-constrained suspended CDPRs whose

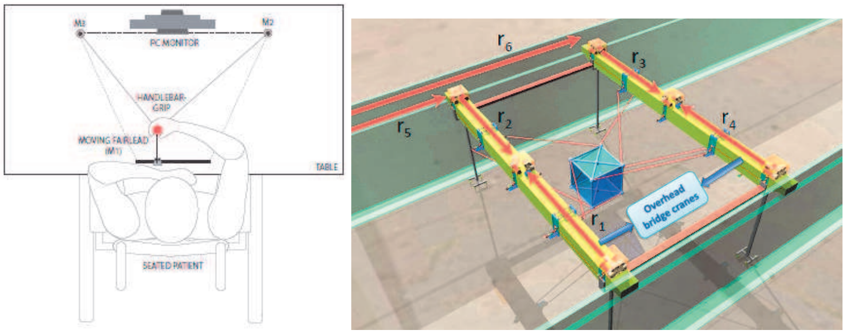

(a) (b)

Figure 23: Layout of Sophia-3 (a), large-dimension reconfigurable suspended CDPR (b).

target is the interaction with workers, the reduction of collision between cables and obstacles and the maximization of the performance.

Two innovative solutions are proposed in this work. The first solution is presented in Chapter 3 and it consists of a cable-suspended parallel robot with a reconfigurable end-effector. The second solution is illustrated in Chapter 4 and it is an innovative model of a cable-driven micro-macro robot. The approach followed for each solution is the following:

1. Derivation of the kinematic and dynamic models for a planar mechanism;
2. Analysis of the performance, comparison with a traditional CDPR and optimal trajectory planning;
3. Derivation of the kinematic and dynamic models for a spatial mechanism.
4. Analysis of the performance and comparison with a traditional CDPR;

3

RECONFIGURABLE CABLE-SUSPENDED PARALLEL ROBOT

In this chapter, a new Cable-Suspended Parallel Robot (CSPR) with reconfigurable end-effector is presented. This robot has been conceived for pick and place operations in industrial environments. For such applications, the possibility to change the configuration of the cables at the end-effector level is a promising way to avoid collisions with obstacles in the approaching phases, while reducing at the same time the duration of motion in the remaining part of the trajectory. An optimized trajectory planning algorithm is proposed, which implements a pick and place operation in the operational space with dynamic on-line reconfiguration of the end-effector. The results on a simplified scenario demonstrate the ability of the system to obtain reduced movement times together with obstacle avoidance. The kinematic and dynamic model of a 6-DOF CSPR with a reconfigurable end-effector is derived and an optimal design is proposed.

3.1 DESIGN OF RECONFIGURABLE END-EFFECTOR

The ability to reconfigure the cable anchor points during a robot movement can increase the reachable workspace, allows for better performance in terms of movement times (increased accelerations/velocities) and avoid collisions between cables and obstacles. As example, consider the possibility to pick parts inside boxes (bin picking) or to serve parts to operators avoiding collisions. The different configurations of the anchor points on the end-effector of a CDPR as well as their effects on the system performance depend on the specific cable system and reconfigurable end-effector.

In this section, we introduce the model of a Cable-Suspended Parallel Robot (CSPR) for pick and place applications that has the capability of modifying the position of the anchor points of the cables to the end-effector. The possibility of on-the-fly adapting cable anchor points to the end-effector is the first novelty introduced. Figure 24 shows a sketch of the system proposed, during an approaching phase (pick or release). In this phase, the CDPR interacts with a worker by using a configuration with the cables anchored at the top of the end-effector to avoid collisions and increase safety. On the other hand, when the end-effector is far from humans and obstacles, the cable anchor points on the end-effector must be reconfigured to maximize performance.

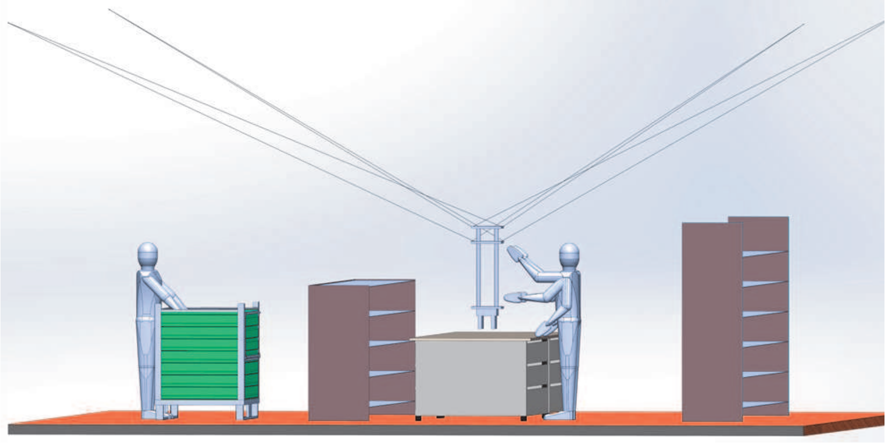

Figure 24: Example of pick and place application with under-constrained CSPR.

3.2 THREE-DOF UNDER-CONSTRAINED CSPR WITH RECONFIGURABLE END-EFFECTOR

Let us consider a simple case of CDPR with reconfigurable anchor points on the end-effector with the following properties:

- under-constrained system with $n = 3$ DOFs ($\mathbf{x} = [x_G, z_G, \beta]^T$) and $N = n + 1 = 4$ cables. It relies on gravity to determine the pose of the end-effector as shown in Fig. 25;
- suspended system that can exert forces along two directions ($\mathbf{F_x}$,$\mathbf{F_z}$) on a vertical plane, and a moment ($\mathbf{M_y}$) normal to the plane;
- reconfigurable end-effector designed with the possibility to change the position of the lower cable anchor points (B_2, B_4), by means of a further translational degree of freedom as shown in Fig. 26.

Figure 25 shows the CDPR whereas Fig. 26 details the reconfigurable end-effector. Table 1 and 2 report the value of the system parameters for respectively the cable system and the end-effector.

As shown in Fig. 26, the model of the end-effector consists of three rigid bodies: the main supporting structure (distributed mass M_1 with inertia I_1 and center of mass G_1), the mobile platform (lumped mass M_2 in G_2), and the load to carry (lumped mass M_L in $G_L \equiv P$). The lower cables are connected to the mobile platform that can move along the vertical direction, with respect to the tool center point; the higher cables are connected to the main structure of the end-effector.

With respect to a CDPR with a non-reconfigurable end-effector, the relative position (${}^G\mathbf{r_i}$) of the anchor points B_i can change with time (see Eq. 3). The reconfigurability of cable anchor points ($\mathbf{r_i}$) on the end-effector can affect the cable vectors $\mathbf{l_i}$ and the position of the center of mass (x_G, y_G, z_G) since the mass distribution can change with respect

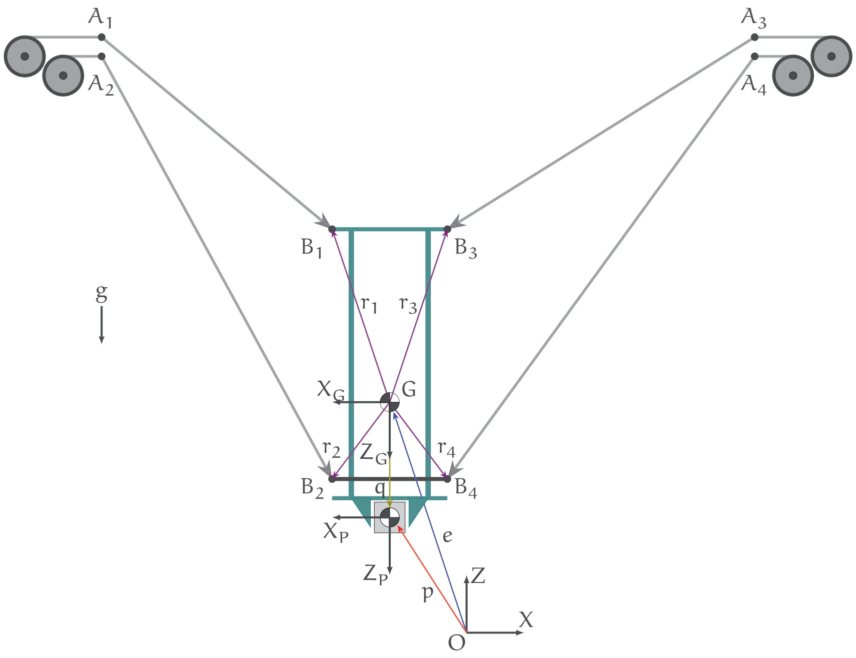

Figure 25: Three-DOF under-constrained CSPR with two reconfigurable anchor points on end-effector. The figure depicts the model of the cable system

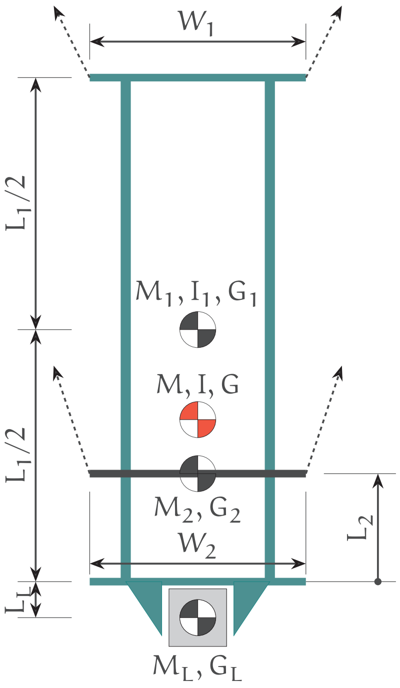

Figure 26: Three-DOF under-constrained CSPR with two reconfigurable anchor points on end-effector. The figure shows the details of the reconfigurable end-effector.

to the pose of the tool center point ${}^{O}\mathbf{p}$. The following section aims at presenting the kinematic model of the reconfigurable end-effector

3.2.1 *Kinematic model*

The kinematic model of the reconfigurable CSPR can be derived from the kinematic model of a generic CDPR presented in Sec. 2.2. Let us define L_2 (see Fig. 26) as the distance from the lower platform to the mobile platform. This length can therefore represent the parameter characterizing the end-effector configurations. By considering the minimum and maximum value of L_2, we can define two limiting configurations:

- case A: configuration with movable anchor points permanently positioned at the lowest extremity of the end-effector (L_2 min);
- case B: configuration with movable anchor points permanently positioned at the highest extremity of the end-effector (L_2 max).

The length L_2 affects the relative position $({}^{G}r_i)$ of the anchor points B_2 and B_4 as well as the position of the center of mass (x_G, z_G). Table 2 shows the effects of these two values of L_2 on the end-effector parameters. A constant orientation of the tool center point ${}^{O}_{G}\mathbf{R}(\alpha, \beta, \gamma) = \mathbf{R_y}(180^\circ)$ is considered for all the poses of the end-effector.

For a fixed position of the tool center point, the structure matrix and the available wrench set vary as a function of the length L_2. As a consequence, the manipulability of the system is strongly affected by the configuration of the end-effector as described in the next section.

3.2.2 *Manipulability*

The possibility to vary the position of the lower anchor points can be very useful in order to pick and place parts inside industrial environments where obstacles must be avoided. However, varying the position of the cable anchor points implies the modification of the maximum wrenches that the cable system can exert on the end-effector.

The wrench closure equation for the under-constrained suspended three-DOF CDPR can be written as:

$$\mathbf{W} = [F_x, F_z, M_y]^T = \mathbf{ST} + \mathbf{W_{ext}} \tag{27}$$

where $\mathbf{S} \in \mathbb{R}^{3\times4}$ and

$$\mathbf{T} = [T_1, T_2, T_3, T_4]^T \tag{28}$$

$$\mathbf{W_{ext}} = [0, -Mg, 0]^T \tag{29}$$

Figure 28 shows the three-dimensional force polytopes, computed in a specified position and by using the data reported in Table 1 and 2, for the two configurations of the end-effector A and B. Consider for instance the case of a moment of magnitude $M_y = 0$ acting on the end-effector. This case can be identified in Fig. 27a and 27b by

Table 1: Parameters of the cable system for the CDPR shown in Fig. 25. The points are expressed in the X-Z plane.

Parameter	Value	Unit
${}^{O}A_1$	$(-2.25, 2.4)$	m
${}^{O}A_2$	$(-2.25, 2.4)$	m
${}^{O}A_3$	$(2.25, 2.4)$	m
${}^{O}A_4$	$(2.25, 2.4)$	m
r_p	0.035	m
τ_{max}	4.0	Nm
T_{max}	114.3	N
$\dot{\theta}_{max}$	3000	rpm
$\dot{l}_{max}$	11.0	m/s
g	9.81	m/s^2

drawing a plane that intersects the polytope for each configuration of the end-effector. The intersection gives a two-dimensional polygon that represents the set of forces F_x and F_z that the CDPR can exert (Fig. 28a and 28b). The maximum allowable force $\mathbf{F_{max}}$ along a generic direction defined in the X-Z plane by the unit vector $\mathbf{u_d} = [d_x, d_z]^T$ is computed as the intersection between the polygon and the given direction. It is worth noticing that the maximum allowable force along the z-negative direction ($\mathbf{u_d} = [0, -1]^T$) depends only on the gravity force, since no cable can exert positive tensions along this direction.

By computing the polytopes for each position of the discretized workspace of the CDPR, a map of the generalized maximum allowable forces can be obtained. Figure 29a illustrates the maximum force along the x-positive ($\mathbf{u_d} = [1, 0]^T$) direction considering a null moment for the configuration A. It is interesting to note that the maximum values are obtained on the north-west region of the workspace since in this region the cables can exert a great component of force along the horizontal direction. On the other hand, Figure 30a illustrates the maximum force along the z-positive ($\mathbf{u_d} = [0, 1]^T$) direction considering a null moment. In this case, the maximum values are obtained in the south region of the workspace since the cables can exert a great component of force along the vertical direction.

The ability of the end-effector to change its configuration increases the complexity of the analysis of manipulability. In fact, for a fixed position of the tool center point, the structure matrix varies as a function of the length L_2. This means that changes of end-effector configuration implicate different set of available wrenches, which vary, in turn, with L_2. Comparing the polytopes obtained for configuration A (Fig. 27a) and B (Fig. 27b), it is clear the reduction in term

Table 2: Parameters of the end-effector for the CDPR shown in Fig. 26. The points are expressed in the X-Z plane.

Parameter	Value		Unit
W_1	0.12		m
L_1	0.3		m
M_1	2.5		kg
I_{G_1}	0.0217		kgm^2
W_2	0.12		m
M_2	0.5		kg
L_L	0.05		m
M_L	1		kg
	Conf. A	Conf. B	
${}^{O}P$	$(0, 0, 0.6)$	$(0, 0.6)$	m
L_2	0.015	0.225	m
M_G	4	4	kg
${}^{P}G$	$(0, -0.133)$	$(0, -0.159)$	m
I_{y_G}	0.061	0.057	kgm^2

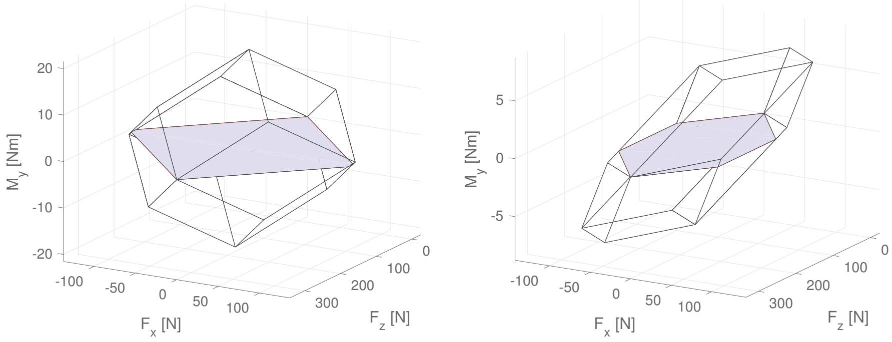

(a) (b)

Figure 27: Three-dimensional force polytope for the three-DOF CSPR shown in Fig. 25 in, respectively, configuration A ($L_2 = 0.015$ m) (left) and configuration B ($L_2 = 0.225$ m) (right).

of manipulability since available forces and moment fall down drastically. For example, the maximum moment decreases from 21.52 Nm for configuration A to 8.77 Nm for configuration B. Similarly, the maximum available force (with $M_y = 0$) along the direction $\mathbf{u_d}$ decreases from 251 N to 172 N (Fig. 28a and 28b). Configuration A, as shown in Fig. 27a and 28a, aims to maximize the performance in terms of manipulability of the system, which in turn means capability to supply higher accelerations and velocities, since higher forces and

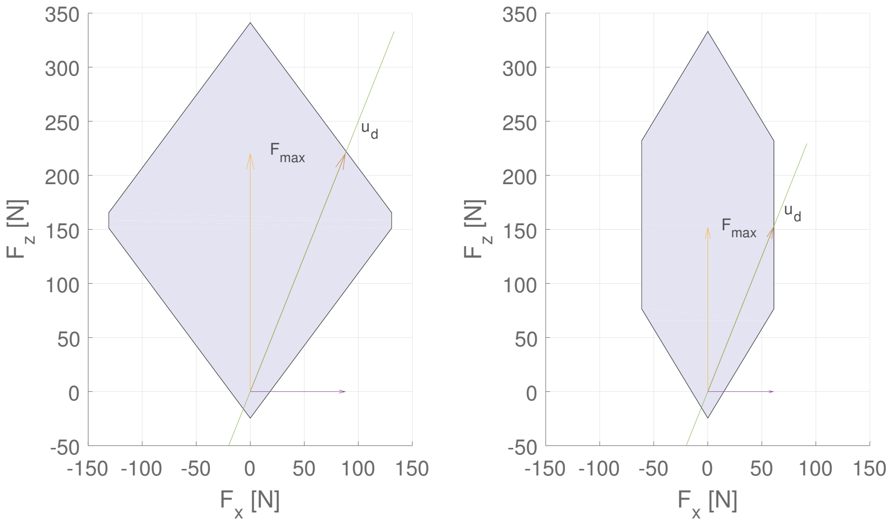

(a)

(b)

Figure 28: Two-dimensional force polytope at a given moment ($M_y = 0$) with the maximum force along the direction $\mathbf{u_d} = [0.4, 1]^T$ for the three-DOF CSPR shown in Fig. 25 in, respectively, configuration A ($L_2 = 0.015$ m) (left) and configuration B ($L_2 = 0.225$ m) (right).

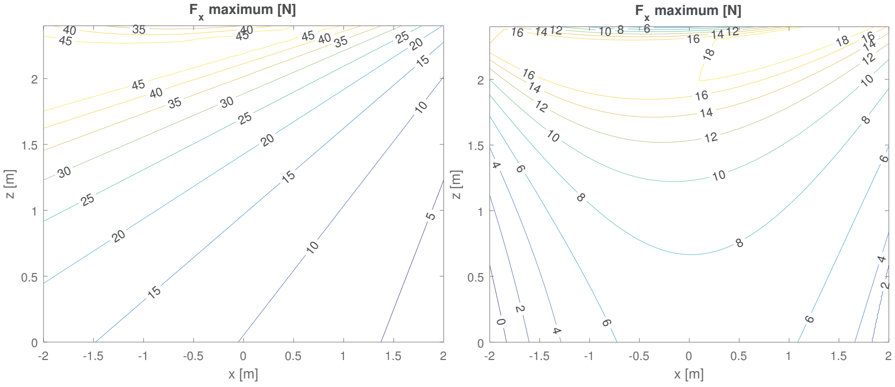

(a)

(b)

Figure 29: Maximum force along the directions $\mathbf{u_d} = [1, 0]^T$ for the CDPR shown in Fig. 25 with $M_z = 0$ and ${}^{O}_{G}\mathbf{R}(\alpha, \beta, \gamma) = \mathbf{R_y}(180^\circ)$. Configuration A($L_2 = 0.015$ m) (a) and configuration B($L_2 = 0.225$ m) (b)

moment can be exerted. On the other hand, it is clear as this configuration of the end-effector tends to maximize cable obstruction. In fact, with the cables positioned so low, the risk of contact between cables and a worker or obstacles disseminated in the environment becomes higher. On the contrary, configuration B maximizes the capability of the end-effector to reach particular positions of the workspace without colliding with surrounding obstacles but at the expense of low manipulability (see Fig. 27b and 28b).

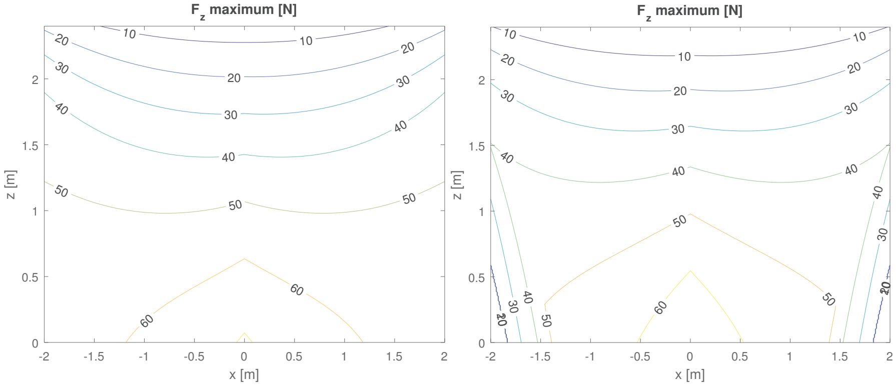

(a) (b)

Figure 30: Maximum force along the directions $\mathbf{u_d} = [0, 1]^T$ for the CDPR shown in Fig. 25 with $M_z = 0$ and ${}^O_G\mathbf{R}(\alpha, \beta, \gamma) = \mathbf{R_y}(180^\circ)$. Configuration A($L_2 = 0.015$ m) (a) and configuration B($L_2 = 0.225$ m) (b)

Figures 29 and 30 represent the maximum force along the x-positive ($\mathbf{u_d} = [1, 0]^T$) and z-positive ($\mathbf{u_d} = [0, 1]^T$) directions considering a null moment for the configuration A and B. As expected, the ability to exert forces along the x-positive direction is strongly reduced whereas small changes appears in the maximum force along the z-positive direction.

With the aim of exploiting the effects of the reconfigurability on CDPR and to maximize the system performance, we define in the following section a simple pick and place task and introduce an algorithm to optimize the trajectory with the aim of reducing the movement time. The algorithm is based on the computation of the force polytope to determine the maximum forces that can be applied on the end-effector along the path.

3.3 OPTIMIZED TRAJECTORY PLANNING OF CDPRS FOR PICK AND PLACE APPLICATIONS

Consider a generic robotic task of pick and place. This type of operation can be considered as typically composed by three movements:

- a vertical depart movement after the picking of the part, which is required to take the end-effector out of the space where it could collide with nearby obstacles;
- a transfer movement (no horizontal in general) to carry the part from an initial to a final position;
- a vertical approach movement before the placing of the part, which is required to avoid collisions with nearby obstacles.

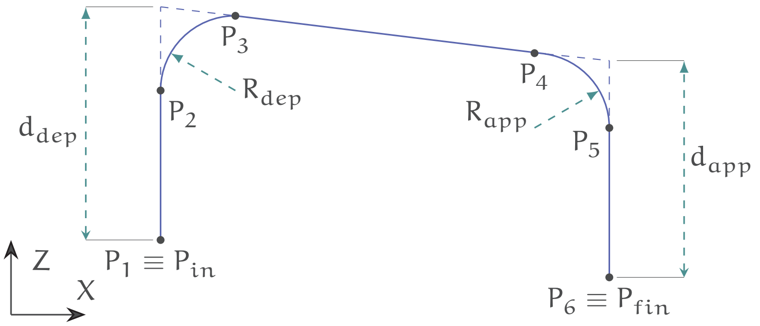

Figure 31: Description of the pick and place movement through four parameters: P_{in}, P_{fin}, d_{dep}, d_{app}.

Assume that P_{in} and P_{fin} are respectively the pick and the release point, expressed in the global reference frame (operational space). Hypothesizing that the CSPR must avoid obstacles, we chose to plan the path of the end-effector (point P) in the operational space. The basic path for the three robot movements is a linear segment. Two arc segments (the depart arc and the approach arc) connect the two vertical movements to the transfer movement (point-to-point straight motions), defined by the radii R_{dep} and R_{app}. Figure 31 shows the pick and place movement path in the $X - Z$ plane of the global frame. Depart movement starts from $P_1 = P_{in}$ and terminates in P_2 while approach movement starts from P_5 and terminates in $P_6 = P_{fin}$. The transfer motion consists in the segment between P_3 and P_4. The first arc connects the points P_2 and P_3, while the second one P_4 and P_5.

The trajectory planning problem consists in generating a trajectory $\mathbf{p}(t)$, where $\mathbf{p}$ is the vector describing the position of the point P of the end-effector in the workspace (Fig. 17) that satisfies for each segment the following constraints:

- initial and final positions;
- initial and final velocities;
- initial and final accelerations;
- acceleration bounded all along the path;
- velocity bounded all along the path.

We propose here to compute the acceleration and velocity constraints by using the N-dimensional polytopes generated by the structure matrix and by the Jacobian matrix of the CDPR.

To set proper velocity and acceleration constraints, and to optimize the time law, we analyze arc and linear segments separately. For the linear segments, we propose a modified version of time-jerk optimal planning by Gasparetto et al. [81], which is used here for operational space planning and with variable constraints for the first time.

Trajectory planning on arc segments

To simplify the model, we assume null values of the tangential accelerations along the depart and approach arcs. We discretize the arcs into r points, and for each intermediate point we compute the maximum value of the force that the cables can exert towards the center of the curve, by using the polytope of the CDPR. Converting the maximum force into acceleration by means of the dynamic model of the CDPR, we compute the maximum allowable centripetal acceleration along the entire arc, which we impose constant:

$$\ddot{p}_{dep} = \min\left(\max\left(\ddot{p}_{dep_i}\right)\right)\Big|_{i=1,\dots,r} = \text{const.} \tag{30}$$

$$\ddot{p}_{app} = \min\left(\max\left(\ddot{p}_{app_i}\right)\right)\Big|_{i=1,\dots,r} = \text{const.} \tag{31}$$

Finally, since the centripetal accelerations are related to the tangential velocities as:

$$\ddot{p}_{dep} = \frac{\dot{p}_{dep}^2}{r_{dep}} \tag{32}$$

$$\ddot{p}_{app} = \frac{\dot{p}_{app}^2}{r_{app}} \tag{33}$$

we can calculate $\dot{p}_{dep}$ that is the final velocity of the depart movement, and $\dot{p}_{app}$ that is the initial velocity of the approach movement respectively. Clearly, $\dot{p}_{dep}$ and $\dot{p}_{app}$ represent also respectively the initial and the final velocity of the transfer motion between P_3 and P_4. The calculation of the trajectory of point P along the arcs is then straightforward.

Trajectory planning on linear segments

The parametric description of each linear segment is given by:

$$\mathbf{p}(\mathbf{t}) = f(s(t)) \tag{34}$$

where s is the arc length along the path. If we consider a linear segment connecting point $\mathbf{p_i}$ to point $\mathbf{p_f}$, the parametric representation of the path is:

$$\mathbf{p}(s) = \mathbf{p_i} + \frac{s}{\|\mathbf{p_f} - \mathbf{p_i}\|}(\mathbf{p_f} - \mathbf{p_i}) \tag{35}$$

$$\frac{d\mathbf{p}(s)}{ds} = \frac{s}{\|\mathbf{p_f} - \mathbf{p_i}\|} \tag{36}$$

$$\frac{d^2\mathbf{p}(s)}{ds^2} = 0 \tag{37}$$

We propose here to apply to the function $s(t)$ a modified version of the algorithm for time-jerk optimal planning proposed by Gasparetto

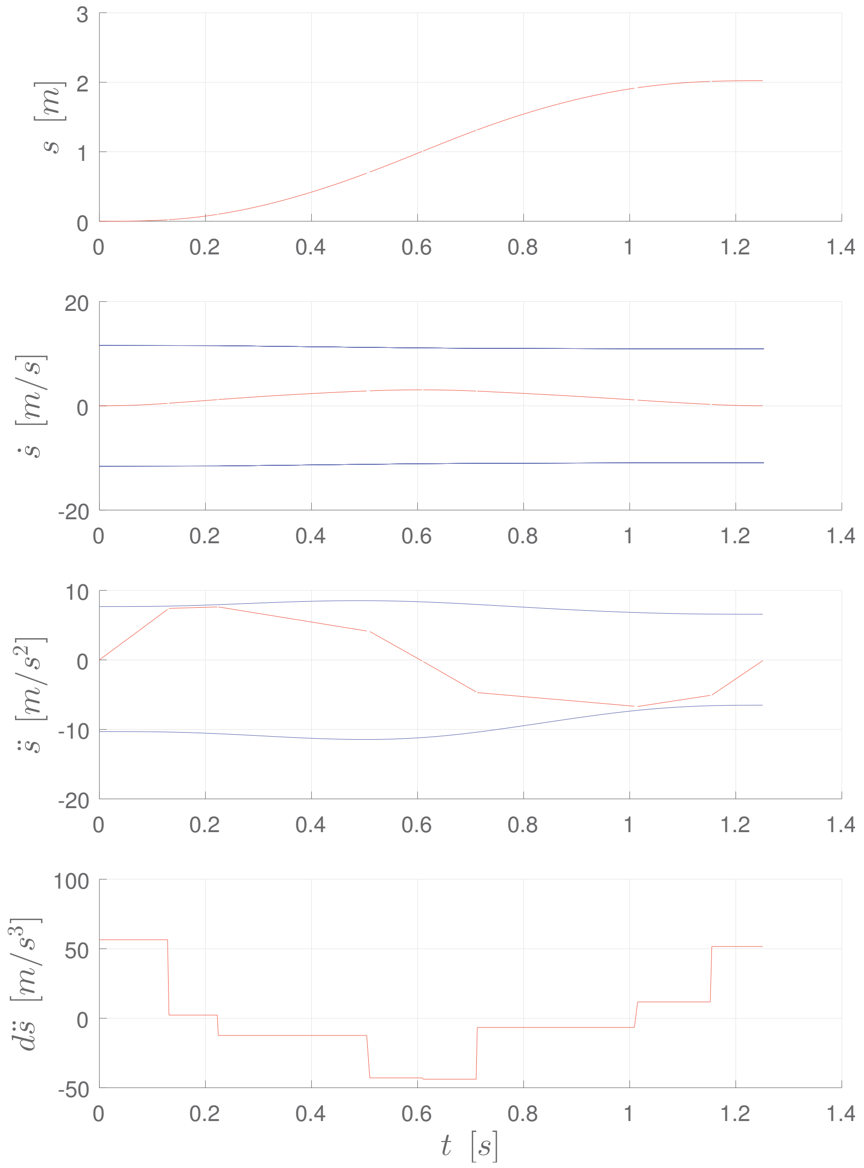

Figure 32: Example of trajectory optimization with different weights of α_T and α_J. Dashed lines represent the maximum velocities and accelerations allowable for the CDPR, computed by the polytopes. The optimized linear movement are obtained with the reconfigurable end-effector presented in Sec. 3.2.

et al. [81]. To achieve this, we discretize each linear segment into $m-1$ sections and, for each section, the function $s_i(t)$ is planned with a third-order polynomial time law (spline). Via points are equally-spaced along s, whereas the duration of motion in each section can be modified to optimize a cost function.

Let us define $h_i = t_{i+1} - t_i$ with $i = 1, \dots, m+1$ as the time required to reach s_{i+1} from s_i. Since the generic polynomial for each

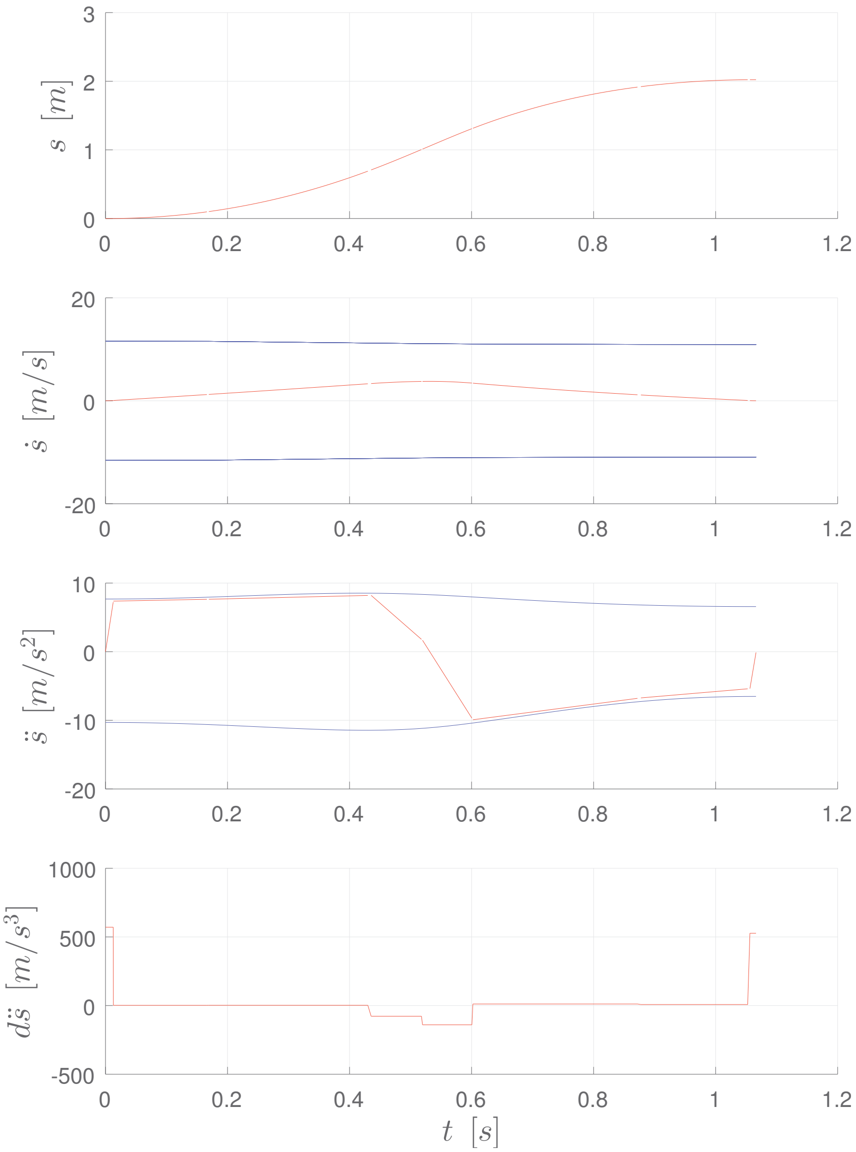

Figure 33: Example of trajectory optimization with different weights of α_T and α_J. Dashed lines represent the maximum velocities and accelerations allowable for the CDPR, computed by the polytopes. The optimized linear movement are obtained with the reconfigurable end-effector presented in Sec. 3.2.

section $s_i(t)$ is a cubic function, its second derivative is a linear function of time which can be written as follows:

$$\begin{aligned} \ddot{s}_i(t) = {} & \frac{\ddot{s}_i(t_i)}{h_i}\Big(t_{i+1} - t\Big) + \\ & + \frac{\ddot{s}_i(t_{i+1})}{h_i}\Big(t - t_i\Big) \quad i = 1, \dots, m+1 \end{aligned} \tag{38}$$

As a consequence the expression of the generic third-order polynomial is given by integrating Eq. 38:

$$\begin{aligned} s_i(t) = \frac{\ddot{s}_i(t_i)}{6h_i}\Big(t_{i+1} - t\Big)^3 + \frac{\ddot{s}_i(t_{i+1})}{6h_i}\Big(t - t_i\Big)^3 + \\ + \Big(\frac{s_i(t_{i+1})}{h_i} - \frac{h_i \ddot{s}_i(t_{i+1})}{6}\Big)(t - t_i) + \\ + \Big(\frac{s_i(t_i)}{h_i} - \frac{h_i \ddot{s}_i(t_i)}{6}\Big)(t_{i+1} - t) \quad i = 1, \dots, m+1 \end{aligned} \tag{39}$$

The linear system to solve consists of m equations [40]:

$$\begin{cases} \dot{s}_1(t_2) = \dot{s}_2(t_2) \\ \vdots \\ \dot{s}_m(t_{m+1}) = \dot{s}_{m+1}(t_{m+1}) \end{cases} \tag{40}$$

where the m unknowns are the accelerations in the via points $\ddot{s}_i(t_i)$. The system can be also expressed in a matrix form as:

$$\mathbf{A}\Big[\ddot{s}_2(t_2) \dots \ddot{s}_{m+1}(t_{m+1})\Big]^T = \mathbf{b} \tag{41}$$

where $\mathbf{b}$ is the vector of the known terms whereas $\mathbf{A}$ is a non-singular coefficient matrix with tridiagonal structure. The solution of the system has to satisfy the following boundary constraints:

$$\begin{cases} \ddot{s}_{i,min} \leqslant \ddot{s}_i(t) \leqslant \ddot{s}_{i,max} & i = 1, \dots, m+2 \\ \dot{s}_{i,min} \leqslant \dot{s}_i(t) \leqslant \dot{s}_{i,max} & i = 1, \dots, m+2 \end{cases} \tag{42}$$

The value of the boundary constraints is computed for each point by using the force and velocity polytopes of the CDPR, respectively. The optimal trajectory planning problem consists in finding, for each linear segment, the function $s(t)$ that minimizes the following objective function:

$$\Omega = \alpha_T \; T + \alpha_J \int_0^T (s^{(3)}(t))^2 \, dt \tag{43}$$

where

$$T = \sum_{i=1}^{m} h_i \quad \text{with} \quad h_i \geqslant 0 \qquad i = 1, \dots, m+1 \tag{44}$$

The optimization variables are h_i. By varying the weights α_T and α_J it is possible to find the desired trade-off between quickness and smoothness. Since the constraints (42) are defined by calculating the polytopes in a set of points along the path, we will obtain a trajectory tailored to the effective force and velocity capabilities of the CDPR along the whole path.

Figure 32 and Fig. 33 show two examples of trajectory optimization with different weights of α_J and α_T. Figure 32 represents position, velocity, acceleration, and jerk obtained for a smoother trajectory ($\alpha_J \gg \alpha_T$). On the other hand, Fig. 33 shows the same parameters calculated for quicker trajectory ($\alpha_T \gg \alpha_J$). The dashed lines represent the boundary values of acceleration and velocity calculated considering the polytope and the direction of movement along the path.

3.3.1 *Trajectory optimization for CDPRs with reconfigurable anchor points on end-effector*

When a CDPR is equipped with a reconfigurable end-effector, the configuration of the cables can vary also due to a change of the position of the movable anchor points on the end-effector (reconfiguration). As explained in Sec. 2.4, a new configuration of the end-effector generates a new set of maximum velocities and forces that the robot can exert for the same pose of the tool center point. The application of the proposed algorithm to optimally plan the trajectory of a reconfigurable CDPR has therefore to take into account that reconfigurability affects the boundary values of velocity and acceleration, which are inputs of the algorithm. By iterating this procedure, we can therefore plan optimal trajectories with the end-effector that changes its configuration to achieve and maintain a target. For example, in the case of pick and place operations, several reconfiguration strategies are possible but we focus here on the ability to operate without colliding with operators and obstacles. In other words, we define the configuration of the end-effector which minimizes the risk of collisions between the cables and the surrounding environment, and we use the optimization algorithm to plan the trajectory which minimizes the total movement time.

This section illustrates the application of the proposed trajectory planning method (Sec. 3.3) to the reconfigurable CDPR considered.

A way to both optimize movement performance and avoiding obstacles could be to plan the trajectory for the pick and place task with a on-line reconfiguration of the end-effector (case C). In this way, the anchor points could be moved as function of the movement segment that the CDPR must travel, but keeping the reconfiguration movement in hidden time. An optimal combination could be:

- depart: from configuration B to A;
- transfer: configuration A;
- approach: from configuration A to B;

This case with on-line reconfiguration aims to have a system able to maximize the performance during the transfer motion but maintaining the ability to avoid collision with obstacles during the depart and

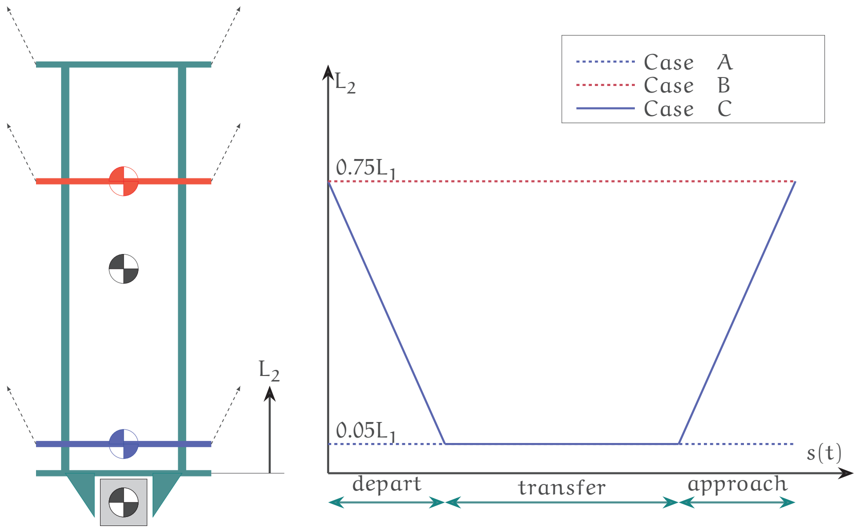

Figure 34: Reconfigurability of the end-effector during the pick and place movement. The end-effector has one DOF represented by the variable L_2.

approach phases. Figure 34 shows the three cases considered: the two static relevant configurations A and B, and case C with the on-line reconfiguration of the end-effector as function of the arc length s along the path.

The algorithm of optimal trajectory planning can be therefore applied to these three cases. By neglecting the translational DOF of the reconfigurable end-effector and the inertial effects of the lumped mass representing the mobile platform, the acceleration boundaries can be derived from the force polytopes by using the mass matrix of the system $\mathbf{M}$:

$$\ddot{\mathbf{x}} = \mathbf{M}^{-1}\ \mathbf{W} = \begin{bmatrix} M_G & 0 & 0 \\ 0 & M_G & 0 \\ 0 & 0 & I_{y_G} \end{bmatrix}^{-1} \mathbf{W} \tag{45}$$

3.3.2 *Simulation tests and results*

In order to evaluate the effects of the end-effector reconfigurability on the system performance of a reconfigurable CSPR for pick and place applications, simulation tests were implemented and performed on the reconfigurable CDPR presented in Sec. 3.2. Table 1 and 2 show the values of the parameters used for the CDPR.

The task is the pick and place movement as described in Sec. 3.3. Table 3 reports the values of the movement task used in the simulations, with reference to Fig. 31.

These simulations aim specifically to compare the motion executed by, respectively, keeping configuration A, configuration B or with on-

Table 3: Trajectory parameters for the movement task. The points are expressed in the X-Z plane. The rotations are expressed in terms of yaw-pitch-roll angles.

Parameter	Value	Unit
${}^{O}P_{in}$	$(-1, 0.3)$	m
${}^{O}P_{fin}$	$(1, 0)$	m
d_{dep}	1.5	m
d_{app}	1.5	m
α_z	0	°
β_y	180	°
γ_z	0	°
R_{dep}	0.3	m
R_{app}	0.3	m

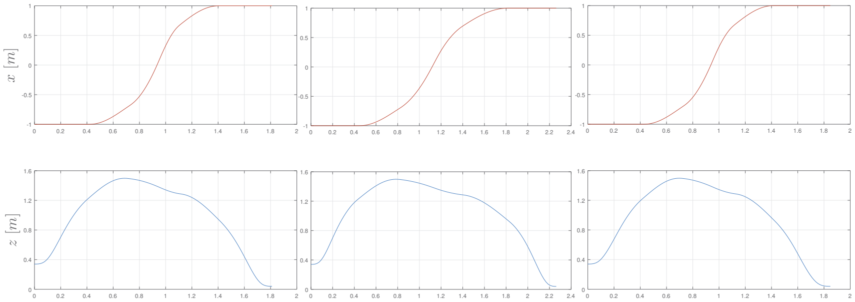

(a) (b) (c)

Figure 35: Position profiles calculated using the optimized trajectory with the end-effector in different configurations: (a) configuration A ($L_2 = 0.015$ m), configuration B ($L_2 = 0.225$ m) and configuration C (L_2 is variable as shown in Fig. 34). Red lines depict the component along the horizontal direction x while blue lines represent the component along the vertical direction z.

line reconfiguration (case C), as shown in Fig. 34. The value assumed by L_2 during the movement is fixed for the two configurations A and B (see Table 2). Case C is characterized by the hidden on-line reconfigurations from B to A and A to B during the vertical movements, described by the variable value of L_2.

Figure 35, 36 and 37 show the results in terms of position, velocity and acceleration of the trajectory planning for the end-effector tool center point for the three configurations considered. The contributes along x and z are illustrated in order to completely define the trajectory in the operational space and to better understand the dynamics of the movement. We reported the maximum values of acceleration and deceleration achievable by the system during the movement. As

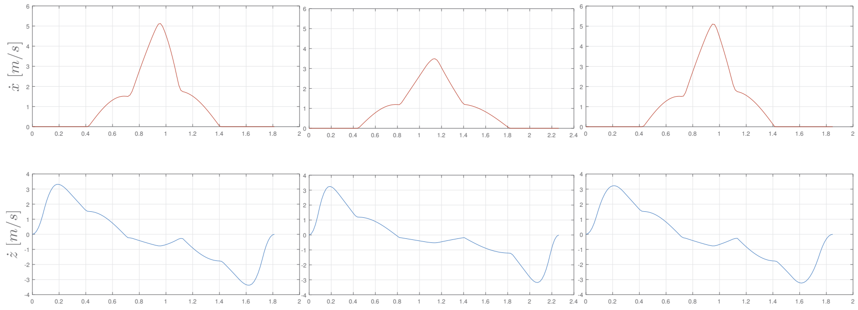

(a) (b) (c)

Figure 36: Velocity profiles calculated using the optimized trajectory with the end-effector in different configurations: (a) configuration A ($L_2 = 0.015$ m), configuration B ($L_2 = 0.225$ m) and configuration C (L_2 is variable as shown in Fig. 34). Red lines depict the component along the horizontal direction x while blue lines represent the component along the vertical direction z.

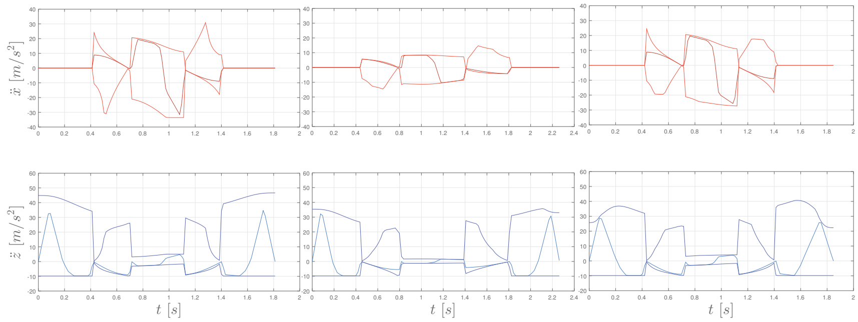

(a) (b) (c)

Figure 37: Acceleration profiles calculated using the optimized trajectory with the end-effector in different configurations: (a) configuration A ($L_2 = 0.015$ m), configuration B ($L_2 = 0.225$ m) and configuration C (L_2 is variable as shown in Fig. 34). Red lines depict the component along the horizontal direction x while blue lines represent the component along the vertical direction z. Dashed lines and dashed-dot lines represent the maximum acceleration and the maximum deceleration along the horizontal and vertical directions. The combination of the maximum acceleration (as well as the maximum deceleration) along horizontal and vertical directions represents the maximum acceleration along the arc length of the prescribed path used for the optimization of linear movements.

expected, the maximum values of acceleration and deceleration vary along the path as described in Sec 3.2. The figures representing the acceleration profiles reveal the ability of the algorithm to exploit the maximum accelerations achievable by the cable robot.

Comparing Fig. 35 and 36 it can be seen that there is a great difference in term of total movement time. Configuration A presents a total movement time $T_A = 1.80$ s while $T_B = 2.26$ s. It is interesting to point out that the most important difference in term of acceleration is obtained during the intermediate phase where the configuration of the cable strongly influences the maximum force that the cables can exert on the end-effector. In fact, the maximum value of $\ddot{x}_P$ for configuration A is about 20 m/s^2 against a maximum acceleration of 10 m/s^2 for configuration B. These results demonstrate the fundamental role of the cable configuration and how strongly it affects the performance of the system.
During the vertical movement there is a small difference in term of maximum acceleration so that the depart and approach movement times are very similar. It is interesting to point out that the maximum acceleration towards the z-negative direction is 9.81 m/s^2 (gravity acceleration) since the cables can exert force only towards the z-positive direction.

Figure 37 depicts the trajectory profiles of the configuration C that is characterized by an on-line reconfiguration. The ability to change the configuration during the movement allows the system to minimize the movement time through the intermediate phase preserving the ability to reduce the interference with the surrounding obstacles during the depart and approach phases. The total time of movement is $T_c = 1.84$ s that is 2.2 % greater than T_A but 26 % lower than T_B.

As a conclusion, considering a pick and place task composed by three linear segments connected by two arc segments, our results show that a trajectory designed to find an optimal trade-off between movement time and smoothness allows the CDPR to achieve values of acceleration and velocity nearer to the maximum allowable values, defined by the polytopes of the CDPR. This translates into optimal performance in term of total movement time. Furthermore, a on-line reconfiguration of the anchor points on the end-effector results to be able to combine the advantages of configurations that maximize the system manipulability (movement time) with others that increase the free space under the end-effector (obstacle avoidance).

The next section aims at presenting the kinematic and dynamic model of a 6-DOF CSPR with a reconfigurable end-effector. A linear actuator is used to move the mobile platform and, as a result, the system has a total of 7 DOF.

In this section, we introduce the model of a 7-DOF reconfigurable CSPR for pick and place applications that has the capability of modifying the position of the cable anchor points on the end-effector using a linear actuator. As discussed in the previous sections, the possibility of adapting the position of the cable anchor points on the end-effector is a promising solution to reduce the risk of collisions between cables and obstacles.

3.4.1 *Kinematic model*

Let us consider the model of a reconfigurable CSPR with 7-DOF and 8 cables as shown in Fig. 38. The end-effector consists of two rigid bodies: the main supporting structure, here defined as *Body 1*, and the translating platform, here defined as *Body 2*. The upper cables are connected to the main structure of the end-effector; the lower cables are connected to the translating platform, which can slide along a linear axis through a prismatic joint. As a result, the position of the lower anchor points with respect to the upper anchor points can be modified dynamically. The configuration of the cable anchor points is based on the optimal layout presented by Lamaury et al. [61]. This layout guarantees very good orientation capabilities and increases the stiffness of the robot.

Let ${}^{\mathbf{O}}\mathbf{p_1} = [x, y, z]^T$ be the position vector of the center of mass $\mathbf{C_1}$ of *Body 1* relative to the base frame $\{O\} = \mathbf{O} - \mathbf{XYZ}$. The orientation of the reference frame $\{C_1\} = \mathbf{C_1} - \mathbf{x_1 y_1 z_1}$ can be expressed by means of the rotational matrix ${}^{\mathbf{O}}_{\mathbf{C_1}}\mathbf{R}(\alpha, \beta, \gamma)$ where α, β and γ are rotations about the fixed axes of the base frame $\{O\}$. The linear velocity of *Body 1* is ${}^{\mathbf{O}}\mathbf{v_1} = [\dot{x}, \dot{y}, \dot{z}]^T$ whereas the angular velocity is ${}^{O}\omega_1 = [\dot{\alpha}, \dot{\beta}, \dot{\gamma}]^T$. Let d be the relative position of the reference frame $\{C_2\} = \mathbf{C_2} - \mathbf{x_2 y_2 z_2}$ of *Body 2* with respect to $\{C_1\}$. Position and velocity of *Body 2* can be defined as follows:

$$ {}^{\mathbf{O}}\mathbf{p_2} = {}^{\mathbf{O}}\mathbf{p_1} + {}^{\mathbf{O}}_{\mathbf{C_1}}\mathbf{R}(\alpha, \beta, \gamma)[0, 0, d]^T \tag{46} $$

$$ {}^{\mathbf{O}}\mathbf{v_2} = {}^{\mathbf{O}}\mathbf{v_1} + {}^{\mathbf{O}}_{\mathbf{C_1}}\mathbf{R}(\alpha, \beta, \gamma)[0, 0, \dot{d}]^T + {}^{\mathbf{O}}\omega_1 \times ({}^{\mathbf{O}}\mathbf{p_2} - {}^{\mathbf{O}}\mathbf{p_1}) \tag{47} $$

The configuration of the end-effector can be described by the set of independent variables $\mathbf{q} = [x, y, z, \alpha, \beta, \gamma, d]^T$. The position of the tool center point P (to be used for the trajectory planning) can be calculated as follows:

$$ {}^{\mathbf{O}}\mathbf{p} = {}^{\mathbf{O}}\mathbf{p_1} + {}^{\mathbf{O}}_{\mathbf{C_1}}\mathbf{R}(\alpha, \beta, \gamma)[0, 0, -(l_1 + l_L)]^T \tag{48} $$

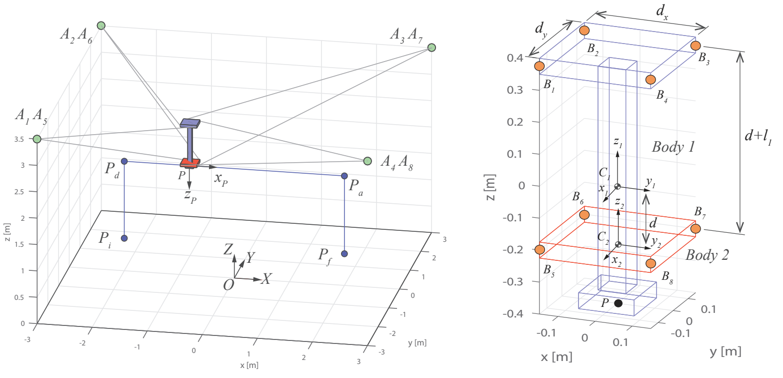

Figure 38: (a) Layout of the CSPR. The path used for the trajectory planning is composed by three linear movements (blue dashed line). (b) Layout of the reconfigurable end-effector. The lower anchor points B_5, B_6, B_7, B_8 can translate along z_2.

3.4.2 *Dynamic model*

The dynamic model of the reconfigurable CSPR presented in the following has been developed based on [41], which was modified to account for the additional degree of freedom. The resultant wrench exerted by the four upper cables on *Body 1* is $\mathbf{w_{t1}}$, whereas $\mathbf{w_{t2}}$ is the wrench exerted by the four lower cables on *Body 2*:

$$\mathbf{w_{t1}} = [\mathbf{f_{t1}}, \mathbf{n_{t1}}]^T = \mathbf{S_1 t_1} \quad \text{and} \quad \mathbf{w_{t2}} = [\mathbf{f_{t2}}, \mathbf{n_{t2}}]^T = \mathbf{S_2 t_2} \tag{49}$$

where $\mathbf{S_1}$, $\mathbf{S_2} \in \mathbb{R}^{6\times4}$ are the structure matrices [82] relative to the center of mass of *Body 1* and *Body 2*, respectively. $\mathbf{t_1} = [\tau_1, \tau_2, \tau_3, \tau_4]^T$ and $\mathbf{t_2} = [\tau_5, \tau_6, \tau_7, \tau_8]^T$ are the vectors of the cable tensions applied to the bodies. Since the end-effector is suspended, the component of the force exerted by the cables on the translating platform along the upward direction must be non negative. To counteract the force applied by the cables on *Body 2*, a spring is inserted between *Body 1* and *Body 2*. *Body 1* and *Body 2* can be modeled as two rigid bodies having mass matrices $\mathbf{M_1} = m_1\mathbf{I_3}$ and $\mathbf{M_2} = m_2\mathbf{I_3}$ and inertia tensors ${}^{C_1}\mathbf{I_1}$ and ${}^{C_2}\mathbf{I_2}$ written in the reference frames $\{C_1\}$ and $\{C_2\}$. The payload is considered as a part of *Body 1*.

Using Newton-Euler approach, the general form of the equations of motion for the reconfigurable CSPR can be obtained in Cartesian space [40]. The force-balance and moment-balance equations can be expressed as follows:

$$\begin{cases} \mathbf{M_1}\,{}^{O}\dot{\mathbf{v}}_\mathbf{1} = {}^{O}\mathbf{f_{t1}} + {}^{O}\mathbf{f_{g1}} - {}^{O}\mathbf{f_2} - {}^{O}\mathbf{f_k} \\ {}^{O}\mathbf{I_1}\,{}^{O}\dot{\omega}_1 + {}^{O}\omega_1 \times {}^{O}\mathbf{I_1}\,{}^{O}\omega_1 = {}^{O}\mathbf{n_{t1}} - {}^{O}\mathbf{n_2} - ({}^{O}\mathbf{p_2} - {}^{O}\mathbf{p_1}) \times {}^{O}\mathbf{f_2} \end{cases} \tag{50}$$

and

$$\begin{cases} \mathbf{M_2}\,{}^{O}\dot{\mathbf{v}}_2 = {}^{O}\mathbf{f}_2 + {}^{O}\mathbf{f}_k + {}^{O}\mathbf{f}_{t2} + {}^{O}\mathbf{f}_{g2} \\ {}^{O}\mathbf{I}_2\,{}^{O}\dot{\omega}_2 + {}^{O}\omega_2 \times {}^{O}\mathbf{I}_2\,{}^{O}\omega_2 = {}^{O}\mathbf{n}_2 + {}^{O}\mathbf{n}_{t2} \end{cases} \tag{51}$$

where the inertia tensors with respect to the base frame are ${}^{O}\mathbf{I}_1 = {}^{O}_{C_1}\mathbf{R}\,{}^{C_1}\mathbf{I}_1\,{}^{O}_{C_1}\mathbf{R}^{T}$ and ${}^{O}\mathbf{I}_2 = {}^{O}_{C_1}\mathbf{R}\,{}^{C_2}\mathbf{I}_2\,{}^{O}_{C_1}\mathbf{R}^{T}$. The gravity forces are $\mathbf{f}_{g1}$ and $\mathbf{f}_{g2}$ whereas $\mathbf{f}_k$ is the force exerted by the spring along $\mathbf{z}_2$. The magnitude of $\mathbf{f}_k$ can be modeled by the linear law $f_k = k \cdot (d_0 + d)$ where d_0 is the free length of the spring and k is the spring constant. $\mathbf{f}_2$ and $\mathbf{n}_2$ represent the force and moment that *Body 1* exerts on *Body 2*, respectively. Combining the equations above, we obtain:

$$\begin{cases} \mathbf{M_1}\,{}^{O}\dot{\mathbf{v}}_1 + \mathbf{M_2}\,{}^{O}\dot{\mathbf{v}}_2 = {}^{O}\mathbf{f}_{t1} + {}^{O}\mathbf{f}_{t2} + {}^{O}\mathbf{f}_{g1} + {}^{O}\mathbf{f}_{g2} \\ {}^{O}\mathbf{I}_1\,{}^{O}\dot{\omega}_1 + {}^{O}\omega_1 \times {}^{O}\mathbf{I}_1\,{}^{O}\omega_1 + {}^{O}\mathbf{I}_2\,{}^{O}\dot{\omega}_2 + {}^{O}\omega_2 \times {}^{O}\mathbf{I}_2\,{}^{O}\omega_2 = \\ = {}^{O}\mathbf{n}_{t1} + {}^{O}\mathbf{n}_{t2} - ({}^{O}\mathbf{p}_2 - {}^{O}\mathbf{p}_1) \times \left[\mathbf{M_2}\,{}^{O}\dot{\mathbf{v}}_2 - {}^{O}\mathbf{f}_{t2} - {}^{O}\mathbf{f}_{g2} - {}^{O}\mathbf{f}_k\right] \end{cases} \tag{52}$$

The force required by the linear actuator is found by taking the component of the force applied by *Body 1* on *Body 2* along $\mathbf{z}_2$:

$$f_d = {}^{O}\mathbf{f}_2 \cdot {}^{O}\mathbf{z}_2 = \left[\mathbf{M_2}\,{}^{O}\dot{\mathbf{v}}_2 - {}^{O}\mathbf{f}_{t2} - {}^{O}\mathbf{f}_{g2} - {}^{O}\mathbf{f}_k\right] \cdot {}^{O}\mathbf{z}_2 \tag{53}$$

3.5 OPTIMAL DESIGN OF A 6-DOF CSPR WITH RECONFIGURABLE END-EFFECTOR

Pick and place operations are very common in many industrial applications and CSPRs can be a valid alternative to conventional crane systems [75]. Let P_i and P_f be the pick and the release point expressed in the base frame, respectively. Since the CSPR must avoid obstacles, the best option is to plan the path of the tool center point in the operational space. To simplify the pick and place operation, we consider three movements, each represented by a linear segment: vertical depart, transfer movement and vertical approach. We combine the ability to avoid obstacles during the approach/depart movements with the ability to exert high wrenches during the transfer motion by dynamically reshaping the configuration of the lower anchors points as shown in Fig. 38a. Once the task has been defined in terms of planned trajectory, we can optimize the design of the reconfigurable end-effector.

The optimal design aims at minimizing the size of the linear actuator required to dynamically reconfigure the lower anchor points of the end-effector. Using the planned trajectory as input for the inverse dynamics, we calculate the cable tensions and the force required by the linear actuator f_d. We identify three design variables that affect the linear force f_d: the mass distribution (expressed as the ratio

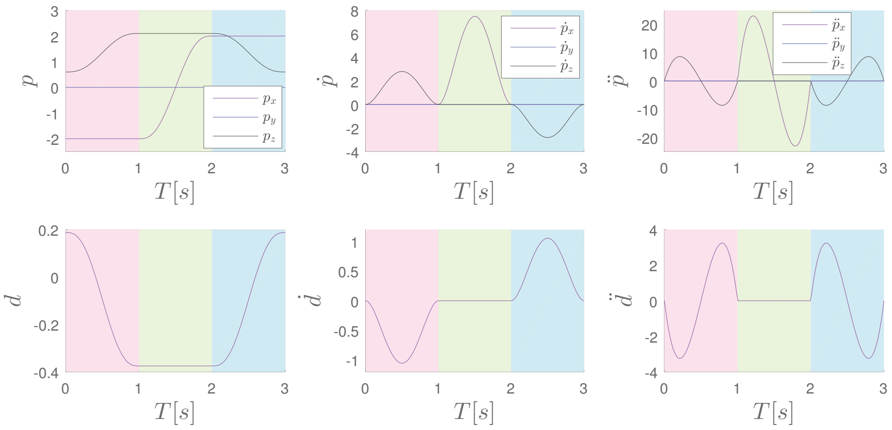

Figure 39: Trajectory profiles of *Body 1* and *Body 2* in terms of position of the tool center point $\mathbf{p}$ and relative position d. The three parts of the movement are highlighted.

$r_m = m_2/(m_1 + m_2)$), the spring constant (k) and the free length of the spring (d_0). The optimization problem consists in finding the optimal set of design variables $x = [r_m, k, d_0]^T$ that minimizes the following objective function during the pick and place movement:

$$\phi = \sqrt[2]{\frac{1}{T}\int_0^T [f_d(t)]^2\,dt} \qquad \text{subject to} \qquad \begin{cases} 0 < r_m < 1 \\ k \geqslant 0 \\ d_0 \geqslant 0 \end{cases} \tag{54}$$

where the sum of the masses m_1 and m_2 is fixed and T is the total time of the movement.

The layout of the reconfigurable CSPR is shown in Fig. 38a and 38b. Table 4 reports the position of the cable exit points (A_i) and the cable anchor points (B_i). The parameters describing initial and final positions of the tool center point as well as the orientation of *Body 1* (assumed constant along the path) are listed in Table 5. The trajectory profiles of *Body 1* and *Body 2* are obtained with three linear movements in the operational space where position is planned with a fifth-order polynomial time law. The total time of the movement is: $T = T_{dep} + T_{trans} + T_{app}$. This trajectory ensures continuity and assigned initial and final position, velocities and accelerations. Position, velocity and acceleration are shown in Fig. 39. The optimization problem was solved by using the GlobalSearch Algorithm proposed by Ugray et al. [83]. The optimal set of design variables that minimizes the objective function ϕ is $x_{opt} = [0.584, 0.0024\ \text{N/m}, 99.8\ \text{m}]^T$. The value of the objective function for the optimal design is $\phi = 3.205$ N.

To compare the effect of the design variables on the objective function, we define two sub-optimal designs:

- *Design 1*: $r_m = 0.171$, $k = 0$ N/m, $d_0 = 0$ m;

Table 4: (a) Cable exit points A_i and cable anchor points B_i. (b) Kinematic and inertial parameters of the reconfigurable end-effector.

Parameter	Value [m]
${}^{O}A_1, {}^{O}A_5$	$(-3, -3, 3.5)$
${}^{O}A_2, {}^{O}A_6$	$(3, -3, 3.5)$
${}^{O}A_3, {}^{O}A_7$	$(3, 3, 3.5)$
${}^{O}A_4, {}^{O}A_8$	$(-3, 3, 3.5)$
${}^{C_1}B_1$	$(d_x, -d_y, L_1)$
${}^{C_1}B_2$	(d_x, d_y, L_1)
${}^{C_1}B_3$	$(-d_x, d_y, L_1)$
${}^{C_1}B_4$	$(-d_x, -d_y, L_1)$
${}^{C_1}B_5$	$(-d_x, d_y, d)$
${}^{C_1}B_6$	$(-d_x, -d_y, d)$
${}^{C_1}B_7$	$(d_x, -d_y, d)$
${}^{C_1}B_8$	(d_x, d_y, d)

(a)

Parameter	Value	Unit
$m_1 + m_2$	7	kg
$I_{1_{xx}}, I_{1_{yy}}$	$m_1[0.050, 0.050]$	kgm^2
$I_{1_{zz}}$	$m_1[0.007]$	kgm^2
$I_{1_{xy}}, I_{1_{xz}}, I_{1_{yz}}$	0	kgm^2
$I_{2_{xx}}, I_{2_{yy}}$	$m_2[0.003, 0.003]$	kgm^2
$I_{2_{zz}}$	$m_2[0.007]$	kgm^2
$I_{2_{xy}}, I_{2_{xz}}, I_{2_{yz}}$	0	kgm^2
d_x	0.2	m
d_y	0.2	m
l_1	0.4	m
l_L	0.05	m

(b)

Table 5: Trajectory parameters for the movement task.

Parameter	Value	Unit
${}^{O}P_{in}$	$(-2, 0, 0.6)$	m
${}^{O}P_{d}$	$(-2, 0, 2.1)$	m
${}^{O}P_{a}$	$(2, 0, 2.1)$	m
${}^{O}P_{fin}$	$(2, 0, 0.6)$	m
α	0	deg
β	0	deg
γ	0	deg
T_{dep}	1.0	s
T_{trans}	1.0	s
T_{app}	1.0	s

- *Design 2*: $r_m = 0.171$, $k = 30$ N/m, $d_0 = 1.15$ m.

Design 1 represents a sample design with a low value of r_m and null values of k and d_0. With respect to *Design 1*, *Design 2* is obtained with the same value of r_m and optimized values of k and d_0. The root mean square (RMS) of the linear actuator force f_d obtained with the optimal design is 91.6% lower than *Design 1* and 76.2% lower than *Design 2*. Fig. 54 represents the cable tensions corresponding the planned movements for the optimal design. The results show a non-negative and continuous tension distribution along the whole trajectory. Figure 41 illustrates the linear actuator force (Eq. 53). Since

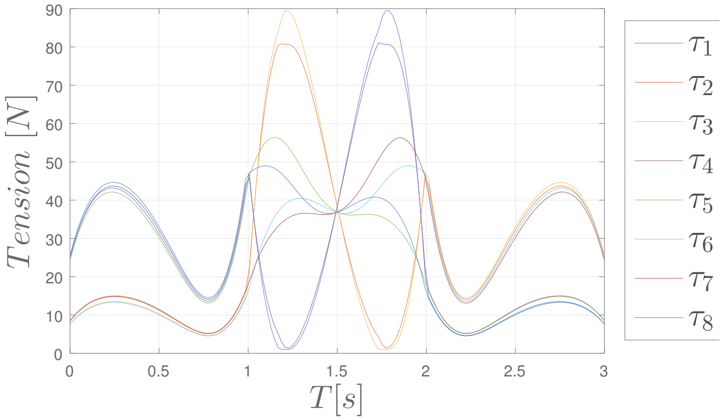

Figure 40: Cable tensions for the planned trajectory.

the end-effector is suspended, the upward component of the force exerted by the cables on *Body 2* must be non negative. Furthermore, the value of $\mathbf{f_{t2}}$ must satisfy Eq. 52. On the other hand, the force of gravity (f_{g2}) and the spring force (f_k) can be optimized to counteract the force exerted by the lower cables $\mathbf{f_{t2}}^T \cdot \mathbf{z_2}$ (green dashed line in Fig. 41) and minimize the force of the linear actuator (f_d). These observations explain the high values of r_m and d_0 obtained with the optimization. High values of r_m reduce the amplitude of the linear actuator force and shift the curve towards a null average value as shown by the green line in Fig. 41. For a fixed value of r_m, the spring allows to reduce the RMS of the force f_d as shown by the yellow and purple lines in Fig. 41. Furthermore, the higher r_m, the higher the maximum tension exerted by the cables during the movement. For example, the maximum cable tension with the optimal design is 20.2% greater than the maximum cable tension calculated for *Design 1* and *Design 2*. The final solution will be a trade-off between the RMS of the linear actuator force and the maximum cable tensions.

3.6 CONCLUSIONS

The motivation behind this work was to present a novel subclass of Cable-Driven Parallel Robots featuring a reconfigurable end-effector. This design shows promises in pick and place applications.

The chapter introduced a model of CDPR with movable anchor points on the end-effector (reconfigurable end-effector) and analyzed the simplified case of a three-DOF under-constrained Cable-Suspended Parallel Robot for pick and place applications in industrial environments. We considered an under-constrained CSPR with $n = 3$ DOFs and $N = n + 1 = 4$ cables which relies on gravity to obtain a stable pose of the end-effector. The end-effector can adaptively change the position of the two lower anchor points of the cables.

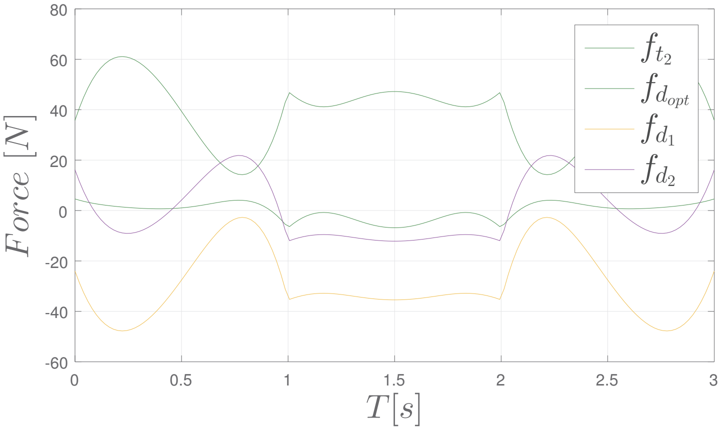

Figure 41: Linear actuator force for the planned trajectory. Green solid line represents the force f_{d} for the optimal layout. Yellow and purple lines represent the force f_{d} for *Design 1* and *Design 2*, respectively. Green dashed lines is the force exerted by the cables to *Body 2* for the optimal layout.

The possibility to change the configuration of the cables in the end-effector is a promising way to avoid collisions with obstacles, augment the ability to interact with the environment and increase the movement performance of the system. In fact, varying the configuration of the cables implies the modification of the maximum allowable wrenches that the cables can exert on the end-effector.

For such reasons, an optimized trajectory planning with a on-line reconfiguration of the end-effector is necessary in order to obtain reduced movement times together with the ability to avoid obstacles. Considering a pick and place task composed by three linear segments connected by two arc segments, our results show that a trajectory designed to find an optimal trade-off between movement time and smoothness allows the CDPR to achieve values of acceleration and velocity nearer to the maximum allowable values, defined by the polytopes of the CDPR. This translates into optimal performance in term of total movement time. Furthermore, a on-line reconfiguration of the anchor points on the end-effector results to be able to combine the advantages of configurations that maximize the system manipulability (movement time) with others that increase the free space under the end-effector (obstacle avoidance).

From the planar mechanism, we developed a system with 7-DOFs and 8 cables which has the capability of modifying the position of the cable anchor points on the end-effector using a linear actuator. The model of the reconfigurable end-effector consists of a main structure and a translating platform which can slide along a linear axis. A simple pick and place task composed of three linear movements was defined and the design of the end-effector was optimized to minimize the linear actuator force. Among the design variables that affect the linear actuator force, mass distribution was found to be the most significant one. Moreover, the use of a spring between the mobile platform and the tool platform allows to further reduce the force required by the linear actuator.

Future works will extend the current optimization framework by considering arbitrary paths where the orientation of the end-effector can be fixed or varying. The pose of the reconfigurable end-effector can affect the kinematic and dynamic behavior of the system influencing the cable tensions and the linear actuator force. Different strategies for trajectory planning and cable tension distribution will also be analyzed and tested.

4

CABLE-SUSPENDED MICRO-MACRO ROBOTS

In this chapter, a new model of a planar under-actuated Cable-Driven Micro Macro Robot (CDMMR) is presented. The system consists of a Cable-Suspended Parallel Robot (CSPR) whose end-effector is a two-link passive serial manipulator. The system is conceived for applications requiring point-to-point motions inside large workspaces and aims at increasing the versatility of CSPRs. The kinematic and dynamic models are presented and the differential flatness framework is applied to make the system controllable for point-to-point movements. A multi-objective optimization framework for the design of u-CDMMRs is proposed. Once the target movements are defined, a multi-objective optimization is applied to minimize two conflicting objective functions: the movement time and the control effort. The objective functions are evaluated using the optimal trajectory obtained applying a time-energy optimal control. This novel approach allows designer to infer useful information about the influence of the design parameters on the dynamic performance of the system.

4.1 MICRO-MACRO ROBOT

Micro-Macro robotic systems [84, 85] are a promising solution to improve the versatility of CSPRs. The idea consists in combining the ability of a CSPR to generate large but coarse motions with the ability of a micro manipulator to perform high-precision, small-range motions. In [86], the authors proposed the dynamic model of a hybrid cable-suspended planar manipulator composed of a two-cable platform connected to a two-link manipulator. This solution enables a potentially large workspace but the dimensions of the links in the proposed system are too small to be effective in practice. Furthermore, the system performance are strongly limited by the cable configuration, since the ability to exert moment is heavily reduced.

Trevisani et al. [87] presented a novel planar translational cable-driven robot with a passive planar two-degree-of-freedom SCARA-type serial robot. The system consists of a hybrid parallel/serial architecture composed by a CDPR and a serial manipulator. The proposed robot has a high payload-to-weight ratio and it allows to increase the performance of the system.

Pigani et al. [88] proposed a novel CDPR with a 3-link passive serial support. This hybrid structure combines positive features of both parallel and serial architectures, and prevents out-of-plane movements without the necessity for the robot to be supported on the motion plane. The adoption of a 3-link serial manipulator ensures a greater workspace area compared with similar structures that adopt a smaller number of links, and improves specific characteristics of their dynamics. However, the presence of the cables increases the risk of collisions with the obstacles located inside the working environment.

In this section, the model of a planar under-actuated Cable-Driven Micro-Macro Robot (u-CDMMR) is introduced. The system consists of a micro-macro manipulator where the macro manipulator is a CSPR with 4 actuated cables, whereas the micro manipulator is a two-link passive serial arm. The passive serial link allows to increase the reachable workspace of the CSPR and reduce the risk of collisions between cables and obstacles since the cable obstruction is significantly diminished.

Studies on under-actuated systems featuring fewer actuators than degrees of freedom have received increasing interest in recent years [89, 43]. Applications of under-actuated mechanical systems include robots for manufacturing [90, 44], inspection [91] and space applications [92]. Greenhouse operations like precise fertilization, spraying and inspection are potential applications of u-CDMMRs [93]. In fact, agricultural environment is typically less friendly for robots than the well structured industrial environments. It is not possible to have fixed position references and the object, with which machines have to interact, have irregular size, location and shape. The available solutions are insufficiently robust, not versatile and expensive. u-CDMMRs have the potential to be a disruptive technology in the agricultural field because of its robustness, simplicity, versatility and accuracy.

Furthermore, under-actuated robots are good candidates for applications involving human-robot cooperation where the robot mass is a major safety concern [94]. In fact, in case of collision between robot and workers, under-actuated robots are intrinsically safer than fully actuated robot since because of their compliant joints and reduced mass.

Controllable under-actuated systems allow point-to-point motions [95, 96] offering, at the same time, an agile, lightweight and simple mechanism. Furthermore, considering the advantages of cable robots, the system is capable of high speed movements inside large workspaces. On the other hand, while fully-actuated systems can execute any continuous trajectory in their workspace, following an arbitrary joint trajectory is generally unfeasible for an under-actuated system. The *differential flatness* framework provides a systemic approach to plan and control feasible trajectories for under-actuated systems [97, 98]. Once the *differential flatness* property of a system is established, the initial and final states can be mapped into corresponding points in the flat output space via diffeomorphism. Then, a smooth trajectory can be planned passing through these points and the corresponding control inputs can be determined.

A general model of CSPR consists of an end-effector which is connected to a fixed frame by n cables. The characteristics of the end-effector affect the reachable workspace, the performance of the system and the ability to avoid obstacles. For example, the possibility to pick parts inside boxes (bin picking) or to serve parts to operators while avoiding collisions between cables and workers. The possibility to design an end-effector able to change configuration is a promising solution to improve the versatility and the performance of the system. In the following, the kinematic and dynamic models of a planar CSPR are derived and compared with the models of an under-actuated cable-suspended parallel robot whose end-effector is a two-link serial manipulator.

4.2.1 *CSPR*

Let us consider the model of a CSPR with 3-DOF and 4 cables as shown in Fig. 42a. The four cables wrap around a suspended spool, which allows to convert the cable tensions into forces (F_x, F_y) and moment (M_z). Each cable wraps around an independent pulley, which can rotate around the two fixed points. *Cable 1* and *cable 2* rotate around A whereas *cable 3* and *cable 4* rotate around B. Let ${}^{\mathbf{0}}\mathbf{p_0} = [x,\ y,\ 0]^T$ be the position vector of the center of mass relative to base frame $\{O\} = \mathbf{O} - \mathbf{XYZ}$. The position of the tool center point is ${}^{\mathbf{0}}\mathbf{p_T} = {}^{\mathbf{0}}\mathbf{p_1} = [x + a_1 \cos\theta_1,\ y + a_1 \sin\theta_1, 0]^T$.

The dynamic model of the planar CSPR can be developed based on [41]:

$$\begin{bmatrix} m, 0, 0 \\ 0, m, 0 \\ 0, 0, I \end{bmatrix} \begin{bmatrix} \ddot{x} \\ \ddot{y} \\ \ddot{\theta} \end{bmatrix} - \begin{bmatrix} 0 \\ -mg \\ 0 \end{bmatrix} = \mathbf{S}\boldsymbol{\tau} \tag{55}$$

The control input of the CSPR is the vector of the cable tensions $\boldsymbol{\tau} = [\tau_1, \tau_2, \tau_3, \tau_4]^T$, which can be converted into the resultant wrench through the structure matrix $\mathbf{S} \in \mathbb{R}^{3\times 4}$:

$$\mathbf{S} = \begin{bmatrix} \mathbf{s_1}, \mathbf{s_2}, \mathbf{s_3}, \mathbf{s_4} \\ r, -r, r, -r \end{bmatrix} \tag{56}$$

where $\mathbf{s_1}, \mathbf{s_2}, \mathbf{s_3}$ and $\mathbf{s_4}$ are the unit vectors describing the cable directions, whereas r is the radius of the spool and the pulleys.

Traditional CSPRs have low versatility. In fact, when obstacles are present inside the working environment, the reachable workspace is strongly reduced. As example, the target points highlighted in Fig. 44 cannot be reached by the tool of the CSPR.

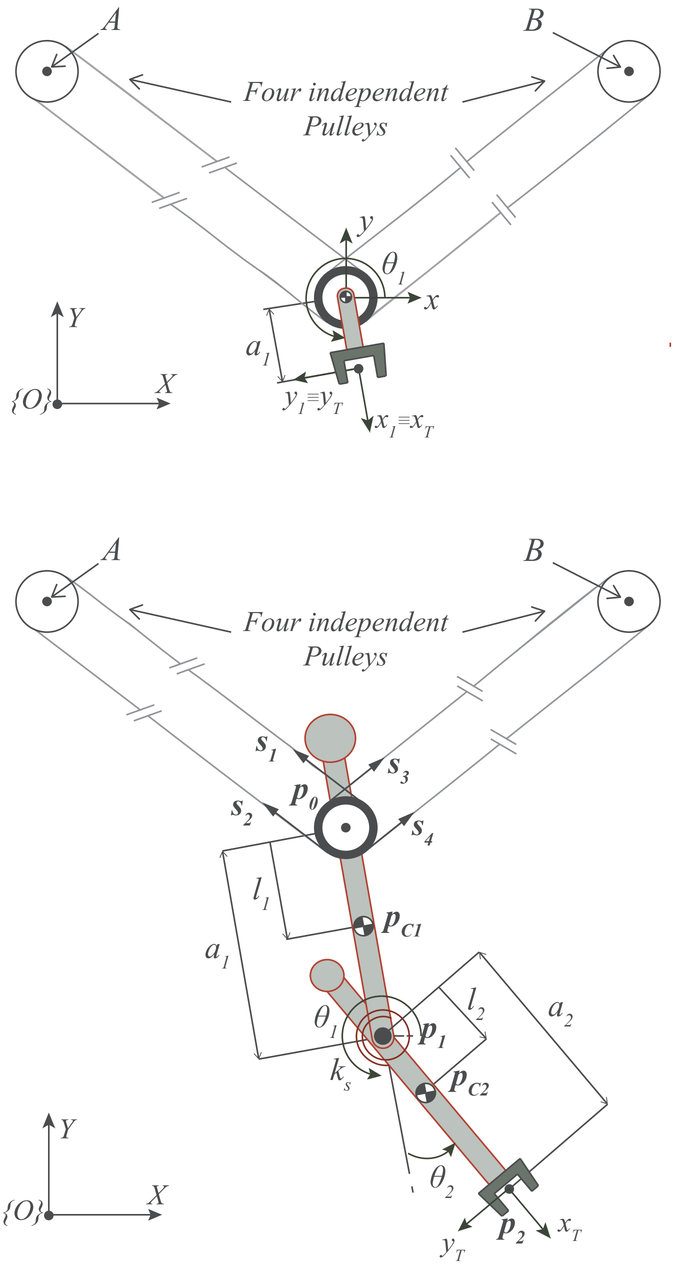

Figure 42: (a) Model of the CSPR. (b) Model of the u-CDMMR.

4.2.2 *Under-actuated CDMMR*

The u-CDMMR, shown in Fig. 42b, consists of a CSPR whose end-effector is a two-link serial manipulator. The system has 4-DOF, namely, $\mathbf{q} = [x, y, \theta_1, \theta_2]^T$. The proximal link is actuated by the cables whereas the distal link is passive. Thus, the system is under-actuated. The links are coupled by a torsional spring whose constant is k_s. Com-

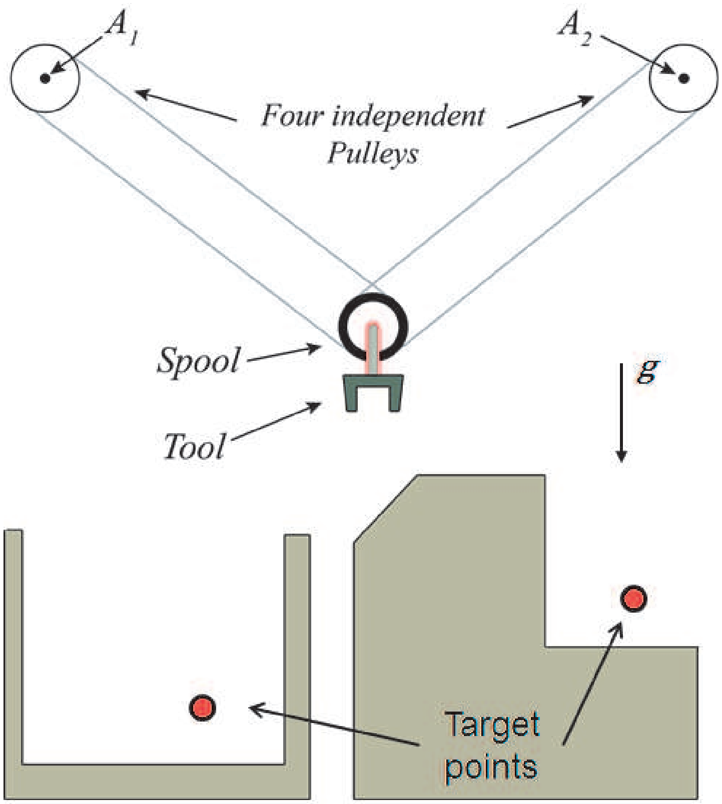

Figure 43: Example of target points that are impossible to reach for a traditional CSPR.

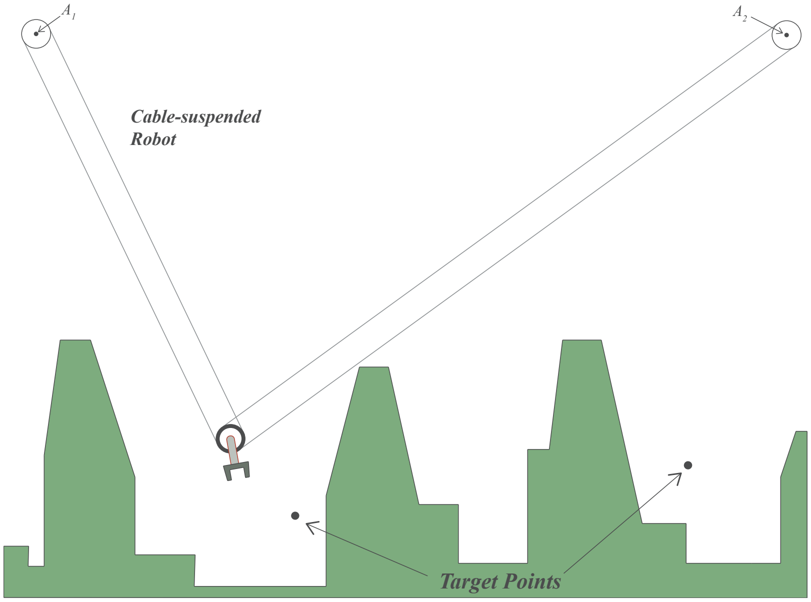

Figure 44: Example of unstructured environment (such as a greenhouse) where target points are impossible to reach for a traditional CSPR.

pared to a traditional CSPR, CDMMR can increase the reachable workspace as shown in Fig. 45

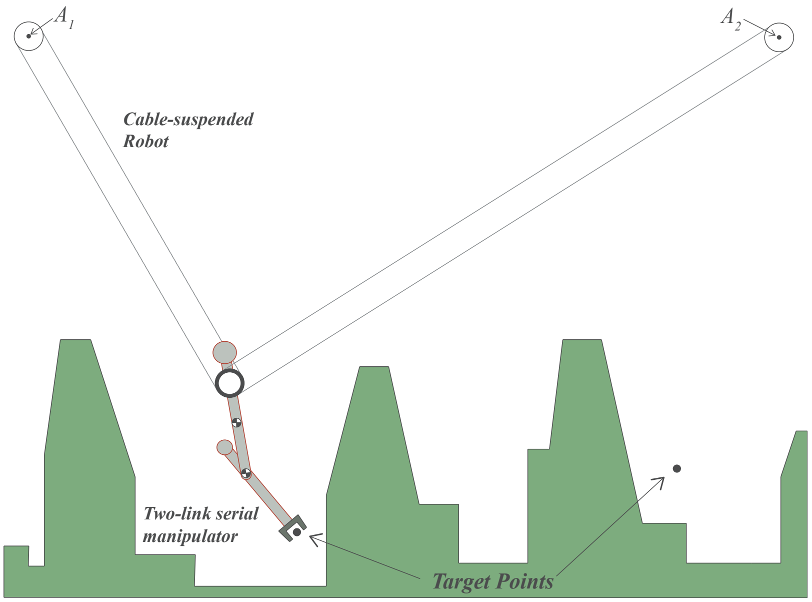

Figure 45: Example of unstructured environment (such as a greenhouse) where the target points can be reached by a CDMMR.

Let us define the following positions relative to the base frame $\{O\} = \mathbf{O} - \mathbf{XYZ}$:

$$ {}^{\mathbf{o}}\mathbf{p}_{\mathbf{0}} = [x,\ y,\ 0]^T \tag{57}$$

$$ {}^{\mathbf{o}}\mathbf{p}_{\mathbf{C1}} = [x + l_1 \cos\theta_1,\ y + l_1 \sin\theta_1, 0]^T \tag{58}$$

$$ {}^{\mathbf{o}}\mathbf{p}_{\mathbf{C2}} = \begin{bmatrix} x + a_1 \cos\theta_1 + l_2 \cos\theta_{12} \\ y + a_1 \sin\theta_1 + l_2 \sin\theta_{12} \\ 0 \end{bmatrix} \tag{59}$$

$$ {}^{\mathbf{o}}\mathbf{p}_{\mathbf{1}} = [x + a_1 \cos\theta_1,\ y + a_1 \sin\theta_1, 0]^T \tag{60}$$

$$ {}^{\mathbf{o}}\mathbf{p}_{\mathbf{2}} = \begin{bmatrix} x + a_1 \cos\theta_1 + a_2 \cos\theta_{12} \\ y + a_1 \sin\theta_1 + a_2 \sin\theta_{12} \\ 0 \end{bmatrix} \tag{61}$$

where $\theta_{12} = \theta_1 + \theta_2$. The position of the tool center point is ${}^{\mathbf{o}}\mathbf{p}_{\mathbf{T}} \equiv {}^{\mathbf{o}}\mathbf{p}_{\mathbf{2}}$. For the same position of the spool, the u-CDMMR allows to increase the reachable workspace compared to the CSPR. Alternatively, the system can reach a specified tool pose in multiple configurations.

The velocities are:

$$ {}^{\mathbf{o}}\dot{\mathbf{p}}_{\mathbf{o}} = [\dot{x},\ \dot{y},\ 0]^{T} \tag{62} $$

$$ {}^{\mathbf{o}}\dot{\mathbf{p}}_{\mathbf{C1}} = \begin{bmatrix} \dot{x} - l_1\dot{\theta}_1 \sin\theta_1 \\ \dot{y} + l_1\dot{\theta}_1 \cos\theta_1 \\ 0 \end{bmatrix} \tag{63} $$

$$ {}^{\mathbf{o}}\dot{\mathbf{p}}_{\mathbf{C2}} = \begin{bmatrix} \dot{x} - a_1\dot{\theta}_1 \sin\theta_1 - l_2\dot{\theta}_2 \sin\theta_{12} - l_2\dot{\theta}_1 \sin\theta_{12} \\ \dot{y} + a_1\dot{\theta}_1 \cos\theta_1 + l_2\dot{\theta}_2 \cos\theta_{12} + l_2\dot{\theta}_1 \cos\theta_{12} \\ 0 \end{bmatrix} \tag{64} $$

$$ {}^{\mathbf{o}}\mathbf{!}_{\mathbf{1}} = [0,\ 0,\ \dot{\theta}_1]^{T} \tag{65} $$

$$ {}^{\mathbf{o}}\mathbf{!}_{\mathbf{2}} = [0,\ 0,\ \dot{\theta}_{12}]^{T} \tag{66} $$

Using Lagrangian's approach, the general form of the equations of motion for the CSMMR can be obtained in Cartesian space [40]. The kinetic energy is:

$$ KE = \frac{1}{2}m_1\dot{\mathbf{p}}_{\mathbf{C1}}^{T}\dot{\mathbf{p}}_{\mathbf{C1}} + \frac{1}{2}m_2\dot{\mathbf{p}}_{\mathbf{C2}}^{T}\dot{\mathbf{p}}_{\mathbf{C2}} + \frac{1}{2}I_1\omega_1{}^{T}\omega_1 + \frac{1}{2}I_2\omega_2{}^{T}\omega_2 \tag{67} $$

where m_1, I_1, m_2, I_2 are the masses and the moments of inertia of the the links w.r.t. their centers of mass. The potential energy is:

$$ PE = m_1\mathbf{g_o}^{T}\mathbf{p}_{\mathbf{C1}} + m_2\mathbf{g_o}^{T}\mathbf{p}_{\mathbf{C2}} + \frac{1}{2}k_s\theta_2^2 \tag{68} $$

where $\mathbf{g_o} = [0, -g, 0]^{T}$.

The control input of the under-actuated system is the vector of the cable tensions $\boldsymbol{\tau} = [\tau_1, \tau_2, \tau_3, \tau_4]^{T}$ which can be mapped into the resultant wrench $\mathbf{u} = [u_1, u_2, u_3]^{T}$ through the structure matrix $\mathbf{S} \in \mathbb{R}^{3\times 4}$.

The state-space equation is given by:

$$ \mathbf{M}(\mathbf{q})\ddot{\mathbf{q}} + \mathbf{V}(\mathbf{q}, \dot{\mathbf{q}}) + \mathbf{G}(\mathbf{q}) = \mathbf{u} = \begin{bmatrix} \mathbf{S} & \mathbf{0}_{3\times 1} \\ 0 & 1 \end{bmatrix} \begin{bmatrix} \boldsymbol{\tau} \\ 0 \end{bmatrix} \tag{69} $$

The coefficients of the mass matrix $\mathbf{M} \in \mathbb{R}^{4\times 4}$ are:

$$ \begin{aligned} M_{11} &= M_{22} = m_1 + m_2 \\ M_{12} &= M_{21} = 0 \\ M_{13} &= M_{31} = -k_1 \sin\theta_1 - m_2 l_2 \sin\theta_{12} \\ M_{14} &= M_{41} = -m_2 l_2 \sin\theta_{12} \\ M_{23} &= M_{32} = k_1 \cos\theta_1 + m_2 l_2 \cos\theta_{12} \\ M_{24} &= M_{42} = m_2 l_2 \cos\theta_{12} \\ M_{33} &= I_1 + I_2 + a_1^2 m_2 + k_2 + k_3 + 2m_2 a_1 l_2 \cos\theta_2 \\ M_{34} &= M_{43} = I_2 + k_3 + m_2 a_1 l_2 \cos\theta_2 \\ M_{44} &= I_2 + k_3 \end{aligned} \tag{70} $$

where $k_1 = l_1 m_1 + a_1 m_2$, $k_2 = m_1(a_1^2 - 2a_1 l_1 + 2l_1^2)$ and $k_3 = m_2(a_2^2 - 2a_2 l_2 + 2l_2^2)$. The vector including the centrifugal and Coriolis terms $\mathbf{V} \in \mathbb{R}^{4\times 1}$ is:

$$\mathbf{V}(\mathbf{q}, \dot{\mathbf{q}}) = \begin{bmatrix} -m_2 l_2(\dot\theta_1 + \dot\theta_2)^2 \cos\theta_{12} - k_1 \dot\theta_1^2 \cos\theta_1 \\ -m_2 l_2(\dot\theta_1 + \dot\theta_2)^2 \sin\theta_{12} - k_1 \dot\theta_1^2 \sin\theta_1 \\ -a_1 m_2 l_2 \dot\theta_2(\dot\theta_2 + 2\dot\theta_1) \sin\theta_2 \\ m_2 l_2 a_1 \dot\theta_1^2 \sin\theta_2 \end{bmatrix} \tag{71}$$

The gravity term $\mathbf{G} \in \mathbb{R}^{4\times 1}$ is:

$$\mathbf{G}(\mathbf{q}) = \begin{bmatrix} 0 \\ g(m_1 + m_2) \\ g(m_2 l_2 \cos\theta_{12} + k_1 \cos\theta_1) \\ g m_2 l_2 \cos\theta_{12} + k_s \theta_2 \end{bmatrix} \tag{72}$$

4.3 DIFFERENTIAL FLATNESS

In general, for an under-actuated robot, not all the outputs can be controlled arbitrarily. The *differential flatness* paradigm allows the determination of those outputs that can be controlled arbitrarily for an under-actuated system, called the *flat outputs*. The number of those outputs equals the number of inputs and the transformation between these flat outputs and the system states is called *diffeomorphism*. As a consequence, a trajectory between any two points in the differentially flat output space is feasible and can be shown to be consistent with the dynamics of the under-actuated system. Agrawal *et al.* [99, 100, 101] presented a technique to design n-DOF under-actuated planar manipulators that are differentially flat. The design method relies on two sufficient conditions: (i) inertia distribution and (ii) spring placement. Considering the mass distribution derived by assuming $l_2 = 0$ and the effect of a spring positioned between *Link 1* and *Link 2*, the new state-space equation for the under-actuated system can be derived from (117-72).

The system is flat and the flat outputs can be selected as $\nu = [\nu_1,\ \nu_2,\ \nu_3] = [x,\ y,\ \theta_{12}]$. Indeed, from (117) we can derive:

$$M_{34}\ddot\theta_1 + M_{44}\ddot\theta_2 + k_s\theta_2 = 0 \tag{73}$$

thus:

$$\theta_2 = -\frac{M_{44}(\ddot\theta_1 + \ddot\theta_2)}{k_s} = -\frac{M_{44}\ddot\nu_3}{k_s} \tag{74}$$

As a consequence, the *diffeomorphism* between the states inputs, the flat outputs and their derivatives is given by:

$$\begin{cases} x = v_1 \\ y = v_2 \\ \theta_1 = v_3 + \frac{M_{44}\ddot{v}_3}{k_s} \\ \theta_2 = -\frac{M_{44}\ddot{v}_3}{k_s} \\ \dot{x} = \dot{v}_1 \\ \dot{y} = \dot{v}_2 \\ \dot{\theta}_1 = \dot{v}_3 + \frac{M_{44}v_3^{(3)}}{k_s} \\ \dot{\theta}_2 = -\frac{M_{44}v_3^{(3)}}{k_s} \end{cases} \qquad \begin{cases} \ddot{x} = \ddot{v}_1 \\ \ddot{y} = \ddot{v}_2 \\ \ddot{\theta}_1 = \ddot{v}_3 + \frac{M_{44}v_3^{(4)}}{k_s} \\ \ddot{\theta}_2 = -\frac{M_{44}v_3^{(4)}}{k_s} \end{cases} \tag{75}$$

thus:

$$\begin{bmatrix} x \\ y \\ \theta_1 \\ \theta_2 \\ \dot{x} \\ \dot{y} \\ \dot{\theta}_1 \\ \dot{\theta}_2 \end{bmatrix} = \begin{bmatrix} 1 & 0 & 0 & 0 & 0 & 0 & 0 & 0 \\ 0 & 1 & 0 & 0 & 0 & 0 & 0 & 0 \\ 0 & 0 & 1 & 0 & 0 & 0 & \frac{M_{44}}{k_s} & 0 \\ 0 & 0 & 0 & 0 & 0 & 0 & -\frac{M_{44}}{k_s} & 0 \\ 0 & 0 & 0 & 1 & 0 & 0 & 0 & 0 \\ 0 & 0 & 0 & 0 & 1 & 0 & 0 & 0 \\ 0 & 0 & 0 & 0 & 0 & 1 & 0 & \frac{M_{44}}{k_s} \\ 0 & 0 & 0 & 0 & 0 & 0 & 0 & -\frac{M_{44}}{k_s} \end{bmatrix} \begin{bmatrix} v_1 \\ v_2 \\ v_3 \\ \dot{v}_1 \\ \dot{v}_2 \\ \dot{v}_3 \\ \ddot{v}_3 \\ v_3^{(3)} \end{bmatrix} \tag{76}$$

The control inputs derived from (117) are:

$$u_1 = M_{11}\ddot{x} - (k_1 \sin\theta_1)\ddot{\theta}_1 - k_1\dot{\theta}_1^2 \cos\theta_1 \tag{77}$$

$$\begin{aligned} u_2 = {} & M_{22}\ddot{y} + (k_1 \cos\theta_1)\ddot{\theta}_1 - k_1\dot{\theta}_1^2 \sin\theta_1 \\ & + g(m_1 + m_2) \end{aligned} \tag{78}$$

$$\begin{aligned} u_3 = {} & -(k_1 \sin\theta_1)\ddot{x} + [k_1 \cos\theta_1]\ddot{y} + \\ & + M_{33}\ddot{\theta}_1 + M_{34}\ddot{\theta}_2 + gk_1 \cos\theta_1 \end{aligned} \tag{79}$$

by applying the *diffeomorphism* (75) we get:

$$
\begin{aligned}
u_1 = {} & M_{11}\ddot{v}_1 - k_1\left(\dot{v}_3 + \frac{M_{44}v_3^{(3)}}{k_s}\right)^2 \cos\left(v_3 + \frac{M_{44}\ddot{v}_3}{k_s}\right) \\
& - \left[k_1 \sin\left(v_3 + \frac{M_{44}\ddot{v}_3}{k_s}\right)\right]\left[\ddot{v}_3 + \frac{M_{44}v_3^{(4)}}{k_s}\right]
\end{aligned} \tag{80}
$$

$$
\begin{aligned}
u_2 = {} & M_{22}\ddot{v}_2 - k_1\left(\dot{v}_3 + \frac{M_{44}v_3^{(3)}}{k_s}\right)^2 \sin\left(v_3 + \frac{M_{44}\ddot{v}_3}{k_s}\right) \\
& + \left[k_1 \cos\left(v_3 + \frac{M_{44}\ddot{v}_3}{k_s}\right)\right]\left[\ddot{v}_3 + \frac{M_{44}v_3^{(4)}}{k_s}\right] + g(m_1 + m_2)
\end{aligned} \tag{81}
$$

$$
\begin{aligned}
u_3 = {} & -\left[k_1 \sin\left(v_3 + \frac{M_{44}\ddot{v}_3}{k_s}\right)\right]\ddot{v}_1 + M_{34}\left[-\frac{M_{44}v_3^{(4)}}{k_s}\right] \\
& + \left[k_1 \cos\left(v_3 + \frac{M_{44}\ddot{v}_3}{k_s}\right)\right]\ddot{v}_2 + M_{33}\left[\ddot{v}_3 + \frac{M_{44}v_3^{(4)}}{k_s}\right] \\
& + g k_1 \cos\left(v_3 + \frac{M_{44}\ddot{v}_3}{k_s}\right)
\end{aligned} \tag{82}
$$

The new state-space equation is:

$$
\mathbf{M}'(v_3, \ddot{v}_3)\begin{bmatrix} \ddot{v}_1 \\ \ddot{v}_2 \\ v_3^{(4)} \end{bmatrix} + \mathbf{V}'(v_3, \dot{v}_3, \ddot{v}_3, v_3^{(3)}) + \mathbf{G}'(v_3, \ddot{v}_3) = \mathbf{u} = \mathbf{S}\boldsymbol{\tau} \tag{83}
$$

where the coefficients of the mass matrix $\mathbf{M}' \in \mathbb{R}^{3\times3}$ are:

$$
\begin{cases}
M'_{11} & = M'_{22} = m_1 + m_2 \\
M'_{12} & = M'_{21} = 0 \\
M'_{13} & = M'_{31} = -k_1 \sin\left(v_3 + \frac{M_{44}\ddot{v}_3}{k_s}\right)\frac{M_{44}}{k_s} \\
M'_{23} & = M'_{32} = k_1 \cos\left(v_3 + \frac{M_{44}\ddot{v}_3}{k_s}\right)\frac{M_{44}}{k_s} \\
M'_{33} & = \frac{M_{33}M_{44}}{k_s} - \frac{M_{34}M_{44}}{k_s}
\end{cases} \tag{84}
$$

The term $\mathbf{V}' \in \mathbb{R}^{3\times1}$ is:

$$
\mathbf{V}' = k_1 \begin{bmatrix} -\sin\left(v_3 + \frac{M_{44}\ddot{v}_3}{k_s}\right)\ddot{v}_3 - \left(\dot{v}_3 + \frac{M_{44}v_3^{(3)}}{k_s}\right)^2 \cos\left(v_3 + \frac{M_{44}\ddot{v}_3}{k_s}\right) \\ \cos\left(v_3 + \frac{M_{44}\ddot{v}_3}{k_s}\right)\ddot{v}_3 - \left(\dot{v}_3 + \frac{M_{44}v_3^{(3)}}{k_s}\right)^2 \sin\left(v_3 + \frac{M_{44}\ddot{v}_3}{k_s}\right) \\ M_{33}\ddot{v}_3/k_1 \end{bmatrix} \tag{85}
$$

and the term $\mathbf{G}' \in \mathbb{R}^{3\times1}$ is:

$$
\mathbf{G}' = \begin{bmatrix} 0 \\ g(m_1 + m_2) \\ g k_1 \cos\left(v_3 + \frac{M_{44}\ddot{v}_3}{k_s}\right) \end{bmatrix} \tag{86}
$$

As a result, the system is fully controllable and can follow any flat output trajectory which satisfies the boundary constraints of the control inputs. Thus, once the flat outputs and its diffeomorphism are established, point-to-point movements can be planned by mapping the states of the system into the flat output space.

A useful task for a robot is to traverse through a given sequence of state points at specified time instants. For the ideal differentially flat system, any output trajectory is consistent with the dynamics. The following steps are necessary to plan a trajectory as shown in Fig. 46:

1. Select the initial and final states ($\mathbf{q}_i$ and $\mathbf{q}_f$) in term of position and velocity.
2. Using the inverse of the diffeomorphism $v = f(q)$ obtained from (75), the initial and final states are transformed into the flat outputs ($\mathbf{v}_i$ and $\mathbf{v}_f$) and their derivatives.
3. Plan the trajectory using a trajectory planning algorithm such as trapezoidal, interpolated polynomials or optimal control.
4. Use the reference trajectory obtained to control the system.

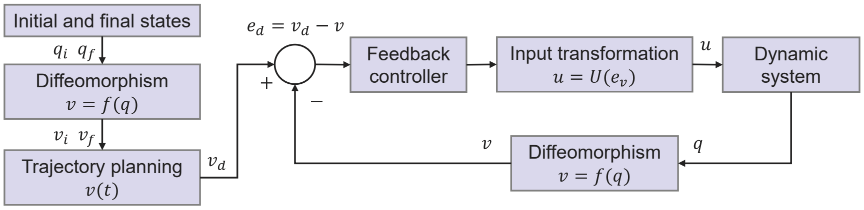

Figure 46: A flatness based controller.

4.4 OPTIMAL DESIGN OF U-CSMMRS

A designer may be interested in finding the optimal set of parameters such as link dimensions, mass distributions and spring constant that can optimize the performance of the u-CDMMR for a set of point-to-point movements of interest. In this work, we minimize the movement time and the control effort required by the actuators. These objectives are typically conflicting, so that no unique optimum can be determined. Rather, a more interesting approach consist in determining a set of optimal design solutions using multi-objective optimization (MOO) and optimal control.

4.4.1 *Design optimization*

There are two general approaches to MOO [102]. One is to combine the objectives into a single function using weight coefficients. However, the determination of the most appropriate coefficients can be difficult and the solution can be strongly affected. The second approach is to determine an entire Pareto optimal set which is a set of solutions that are non-dominated with respect to each other. MOO can be described as follows:

$$\min\big[F_1(\mathbf{x_g}), F_2(\mathbf{x_g})\big] \qquad with \qquad \mathbf{x_g} \in \mathbf{X_g} \tag{87}$$

where $\mathbf{X_g}$ is the feasible set of decision variables and $\mathbf{x_g}$ is a feasible solution. In this work, $F_1(\mathbf{x_g}) = T$ and $F_2(\mathbf{x_g}) = \int_0^T \boldsymbol{\tau}^T \boldsymbol{\tau}\, dt$ are the objective functions to be minimized. $F_1(\mathbf{x_g})$ is the total time required for the movement whereas $F_2(\mathbf{x_g})$ represents the integral of the control efforts required by the actuators during the movement. Clearly, these objective functions are strictly correlated to the trajectory planning technique considered for the point-to-point movements.

Among all the techniques proposed in the literature, optimal control is a powerful approach for computing an optimal trajectory considering the system dynamics [103] and the boundary constraints of the control inputs. Pontryagin *et al.* [104] proved that time-optimal control minimize the movement time generating trajectories where, at any point, at least one of the actuators loads is maximum or minimum (bang-bang control). On the other hand, time optimal control is difficult to follow due to discontinuities in the actuator torques [105]. Time-energy optimal control is an alternative approach which results in smoother trajectories and reduces the actuators load. It consists in minimizing a cost function that combines the movement time and the actuators control efforts and it has been successfully applied in previous works [105, 106, 107].

Figure 47 summarizes the optimization framework used in this work. The Matlab embedded function *gamultiobj* [1] has been used to find the set of optimal design variables which simultaneously minimize the objective functions F_1 and F_2. The fitness functions have been evaluated solving the time-energy optimal control problem which is explained in details in the following section.

4.4.2 *Time-energy optimal control*

The minimum time-energy optimal control consists in finding an admissible set of control inputs able to transfer the system from an initial to a final pose [107]. Equation 83 can be formulated as a system of first order differential equations:

$$\dot{\mathbf{x}}(t) = \mathbf{a}\big(\mathbf{x}(t), \mathbf{x}(\tau), t\big) \tag{88}$$

where $\mathbf{x}$ is:

$$\begin{aligned} \mathbf{x} &= [x_1,\ x_2,\ x_3,\ x_4,\ x_5,\ x_6,\ x_7,\ x_8]^T \\ &= [v_1,\ \dot{v}_1,\ v_2,\ \dot{v}_2,\ v_3,\ \dot{v}_3,\ \ddot{v}_3,\ v_3^{(3)}]^T \end{aligned} \tag{89}$$

---

[1] The MathWorks, Natick, MA, USA.

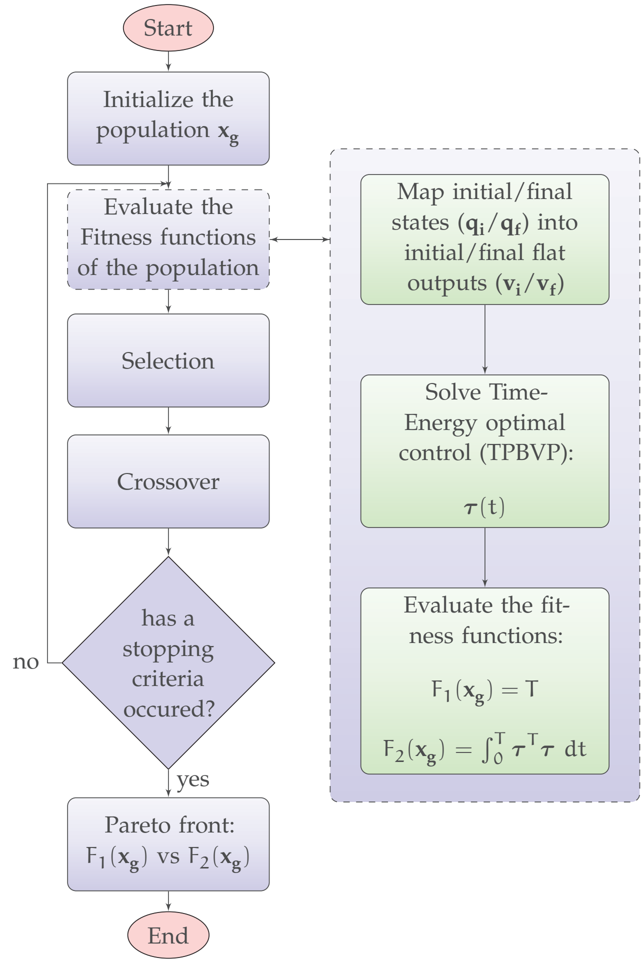

Figure 47: Multi-objective optimization. Time-energy optimal control is used to evaluate the objective functions.

The performance measure is:

$$J = \int_{t_0}^{t_f} 1 + \left[\boldsymbol{\tau}^T \boldsymbol{\tau}\right] dt \tag{90}$$

while the admissible controls, i.e., the cable tensions, are constrained to $\tau_{min} \leqslant \tau_i \leqslant \tau_{max}$, with $i = 1, 2, 3, 4$. The boundary conditions are:

$$\mathbf{x}(t_0) = \mathbf{x}_0, \quad \mathbf{x}(t_f) = \mathbf{x}_f, \tag{91}$$

The problem can be solved using the variational approach [103] which requires the formulation of the Hamiltonian function:

$$H(\mathbf{x}(t), \boldsymbol{\tau}(t), \mathbf{p}(t)) = J + \mathbf{p}^T(t)\left[\mathbf{a}(\mathbf{x}(t), \mathbf{x}(\mathbf{fi}), t)\right] \tag{92}$$

The optimal solution (indicated here by *) must satisfy the following conditions:

$$\begin{cases} \dot{\mathbf{x}}^*(t) = \frac{\partial H(\mathbf{x}^*(t), \mathbf{fi}^*(t), \mathbf{p}^*(t), t)}{\partial \mathbf{p}} \\ \dot{\mathbf{p}}^*(t) = -\frac{\partial H(\mathbf{x}^*(t), \mathbf{fi}^*(t), \mathbf{p}^*(t), t)}{\partial \mathbf{x}} \\ H(\mathbf{x}^*(t), \boldsymbol{\tau}^*(t), \mathbf{p}^*(t)) \leqslant H(\mathbf{x}^*(t), \boldsymbol{\tau}(t), \mathbf{p}^*(t)) \end{cases} \tag{93}$$

Differentiating (92) with respect to **fi** and equating to zero yields the unconstrained (interior) optimal control τ_{int}, which is the optimal control if none of the control constraints is active [105]:

$$\boldsymbol{\tau}_{\mathbf{int}}(t) = \frac{\partial H(\mathbf{x}^*(t), \mathbf{fi}^*(t), \mathbf{p}^*(t), t)}{\partial \mathbf{fi}} \tag{94}$$

If, at some point, one control constraint becomes active, then the optimal control switches to the upper or lower bounds, τ_{max} or $\tau_{min} = 0$, respectively. The structure of the optimal control $\boldsymbol{\tau}^*(t)$ is thus given by:

$$\tau_i{}^*(t) = \begin{cases} \tau_{max}(t) & \text{if} \quad \tau_{int} > \tau_{max} \\ \tau_{int}(t) & \text{if} \quad \tau_{min} \leqslant \tau_{int} \leqslant \tau_{max} \\ \tau_{min}(t) & \text{if} \quad \tau_{int} < \tau_{min} \end{cases} \tag{95}$$

As a result, the vector of control inputs $\tau_i{}^*(t)$ is continuous at the junction points.

The set of differential equations (93), the control law (95), and the boundary conditions (91) define the standard form of Two Point Boundary Value Problem (TPBVP). The standard form of a TPBVP can be solved by Matlab using the *Bvp4c* solver, which is a finite difference algorithm based on Simpson method [108]. This is a collocation formula and the collocation polynomial provides a C^1 continuous solution based on mesh selection and error control of the residuals The result is a trajectory which features the minimum movement time with the minimum control effort during the whole movement and it is strongly related to the dynamics of the system.

4.5 ILLUSTRATIVE EXAMPLE

In this section, we present an illustrative example of the optimization framework for the design of the u-CDMMR (42b). The set of design variables considered in the multi-objective optimization is $\mathbf{x_g} = [a_1, a_2, k_s, l_1/a_1]^T$. The links are modeled as uniform rods with counter masses positioned to obtain the desired mass distribution. The ranges of the design variables as well as the constant parameters of the u-CDMMR are listed in Table 7a. A representative point-to-point movement was defined and the initial and final pose of the tool center point are outlined in Table 7a. The initial and final states $\mathbf{q_i} = [x_i, y_i, \theta_{1_i}, \theta_{2_i}]^T$ and $\mathbf{q_f} = [x_f, y_f, \theta_{1_f}, \theta_{2_f}]^T$ can be easily determined using the inverse kinematics of the two-link manipulator [40].

Figure 48 shows the Pareto front obtained with the multi-objective optimization. As expected, the objective functions representing the movement time and the control effort (87) are inversely related. The total time of the movement (F_1) ranges between 1.0 s and 1.65 s whereas the control effort of the actuators (F_2) varies between 216 N^2s and 380 N^2s. Two optimal design solutions are highlighted: solution

Table 6: (a) Design variables and parameters of the u-CDMMR. (b) Parameters describing the CSPR.

	Value	Unit
${}^{O}A$	$(-2, 2, 0)$	m
${}^{O}B$	$(2, 2, 0)$	m
r	0.15	m
g	9.81	m/s^2
m_1	8	kg
m_2	3	kg
I_1	$[0.5, 1]$	kgm^2
I_2	$[0.25, 0.5]$	kgm^2
a_1	$[0.45, 0.75]$	m
a_2	$[0.45, 0.75]$	m
k_s	$[1, 6]$	Nm/rad
l_1/a_1	$[-0.375, 0.5]$	$-$

(a)

	Value	Unit
${}^{O}A$	$(-2, 2, 0)$	m
${}^{O}B$	$(2, 2, 0)$	m
r	0.15	m
g	9.81	m/s^2
m	11	kg
a_1	0.45	m
I	0.5	kgm^2

(b)

Table 7: Parameters defining the point-to-point movement.

	Value	Unit
τ_{max}	100	N
τ_{min}	0	N
${}^{O}\mathbf{p}_{Ti}$	$(-1.5, -2, 0)$	m
θ_{1_i}	240	deg
θ_{2_i}	60	deg
${}^{O}\mathbf{p}_{Tf}$	$(1.5, 0, 0)$	m
θ_{1_f}	300	deg
θ_{2_f}	-60	deg

S_1 represents the optimal set of design variables that minimizes F_1, whereas S_2 represents the optimal solution that minimizes F_2. In addition, a further design solution, S_3, is shown. This does not belong to the Pareto front but allows us to better understand the behavior of the system.

For comparison with the performance of the CDPRs presented in Sec. 4.2.1, Fig. 48 also shows the results of the optimal trajectory obtained for the CSPR, whose parameters are listed in Table 7b. The optimal values of F_2 were computed using an optimal energy control approach [103] where the input movement times were the values of F_1 obtained with the design optimization of the u-CDMMR. It is interesting to note that the CSPR provides trajectories with lower control effort when the movement time is larger than 1.3 s. On the other hand, u-CDMMR allows for high speed movements with lower control efforts.

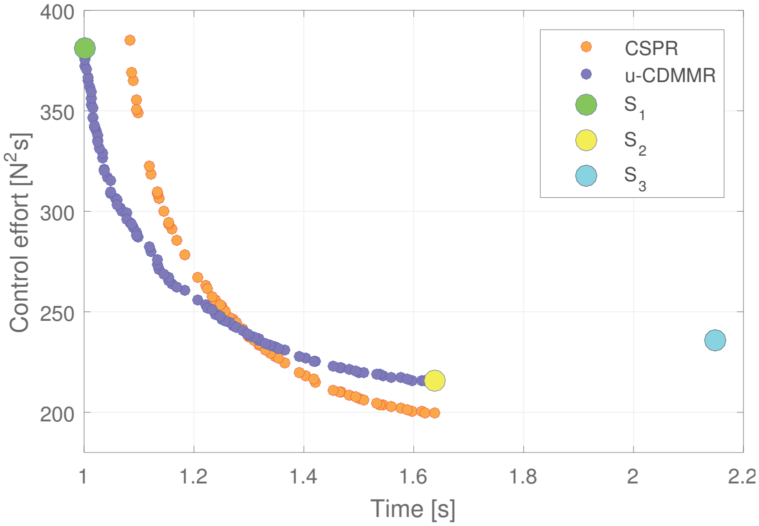

Figure 48: Pareto front of the objective functions F_1, the time of the movement, and F_2, the control effort of the actuators.

Figures 49 and 50 illustrates the values of F_1 and F_2 as functions of the design variables. These plots provide insight into the effects of the design variables on the objective functions. Figure 49 reports the effects of the link dimensions a_1 and a_2. The value of a_2 tends to assume values close to the lower bound whereas the length a_1 has a strong influence on F_1 and F_2. High values of a_1 are related to high speed movements whereas low values provide lower control efforts. When the length of *Link 1* is large, the spool can take more favorable positions relative to the tool center point, allowing the generation of higher forces and moment. In this case, the higher the position of the spool, the larger the horizontal component of the force that can be exerted by the cables.

Similarly, Fig. 50 shows the effects of k_s and l_1/a_1. The former has a great influence on the objective functions and a clear trend is recognizable. High stiffness corresponds to high speed movement while low stiffness minimizes the control effort. Lower stiffness allows to pump energy into the system through the oscillation of *Link 2*. On the other hand, exploiting the oscillation of *Link 2* implies higher movement times. The position of the center of mass of *Link 1* tends to reach the lower bound ($l_1/a_1 = -0.375$), that is, a design where the center of mass of the whole system is located at the center of the spool ($k_1 = l_1 m_1 + a_1 m_2 = 0$).

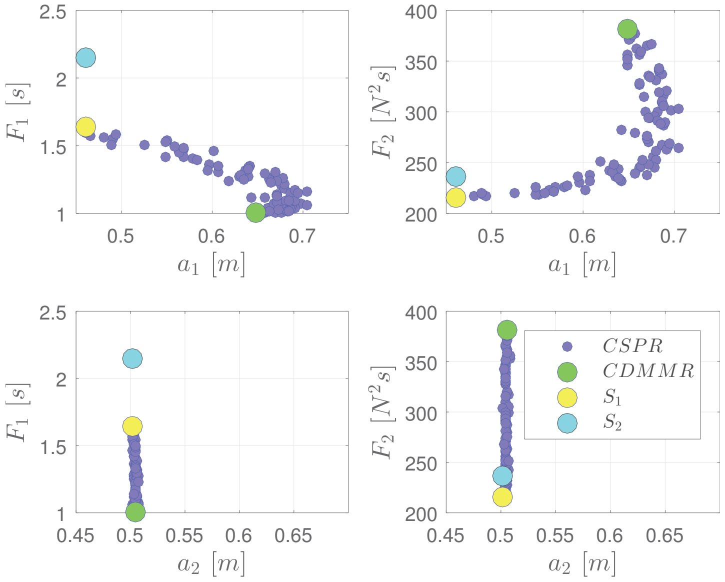

Figure 49: Influence of the design variables a_1 and a_2 on the objective functions F_1 and F_2

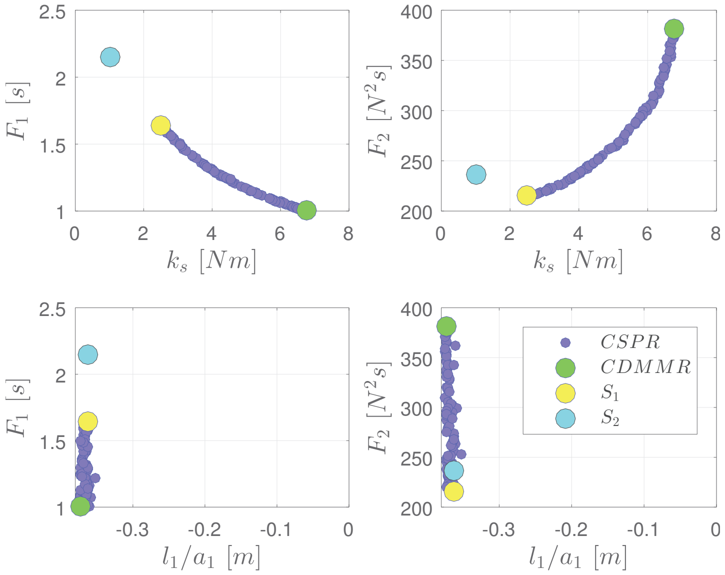

Figure 50: Influence of the design variables k_s and l_1/a_1 on the objective functions F_1 and F_2.

Figure 51 and Fig. 52 show the flat outputs for the optimal sets of design variables S_1 and S_2. The initial and final boundary conditions are satisfied and an interesting dynamic behavior can be observed. The optimal trajectory obtained for Solution S_1 (Fig. 51) tends to assume a trapezoidal profile for $\dot{v}_1$ and v_2. On the other hand, The optimal trajectory obtained for solution S_2 (Fig. 52) presents a cubic

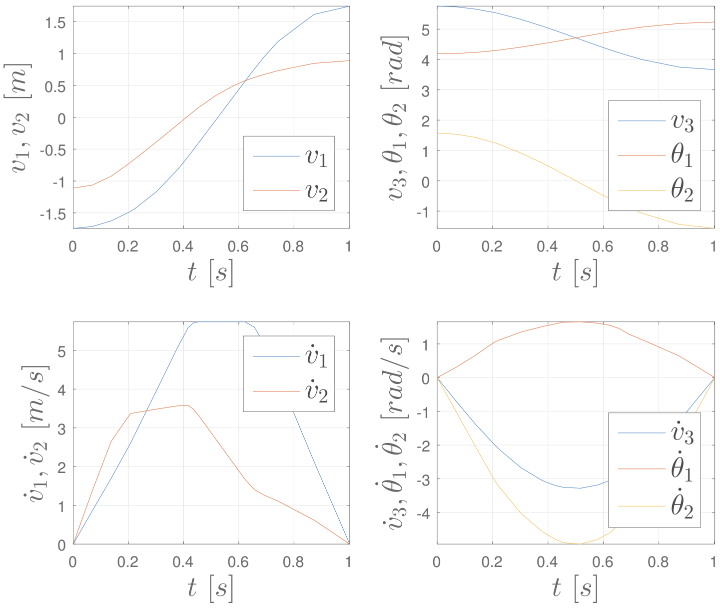

Figure 51: Flat outputs for two optimal set of design variable: solution S_1.

profile which is a well-known solution to minimize the control effort [40].

Solution S_2, which minimizes the control effort during the point-to-point movement, exploits the swinging energy of *Link 2* during the first part of the movement and then accelerates to the vertical upward direction. This behavior would be even more significant with lower values of the spring constant as shown in Fig. 56 and 54d, where solution S_3 clearly exploits the swinging of *Link 2* [95]. However, the solutions featuring low spring constant is excluded from the Pareto front (Fig. 48) because long motion times are required to swing the manipulator.

A clear difference in terms of cable tensions can be observed by comparing Fig. 54a, 54b and 54c representing solutions S_1, S_2 and S_3, respectively. Solution S_1 saturates the actuators, confirming the fundamental role of the control input constraints defined by Eq. 95. On the contrary, solutions S_2 and S_3 reduce the cable tensions.

4.6 3D U-CSMMR

The planar mechanism can be generalized to the three dimensional case. The u-CSMMR, shown in Fig. 55, consists of a CSPR whose end-effector is a two-link serial manipulator. The system has 8-DOF, namely, $\mathbf{q} = [x, y, z, \alpha, \beta, \gamma, \theta_1, \theta_2]^T$. The main frame is actuated by the cables, the proximal link is actuated by a motor, the distal link is passive. The possibility to control the orientation of *Link 1* with a redundant motor (θ_1) allows to increase the range of motion of the

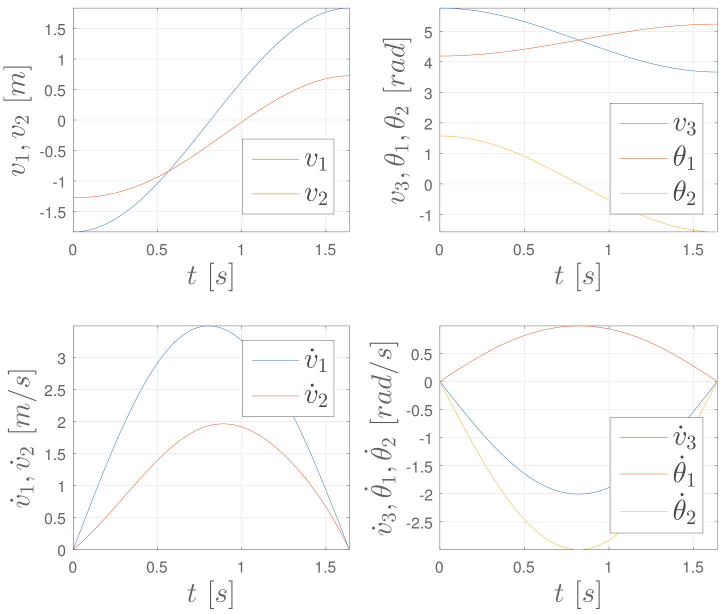

Figure 52: Flat outputs for two optimal set of design variable: solution S_2.

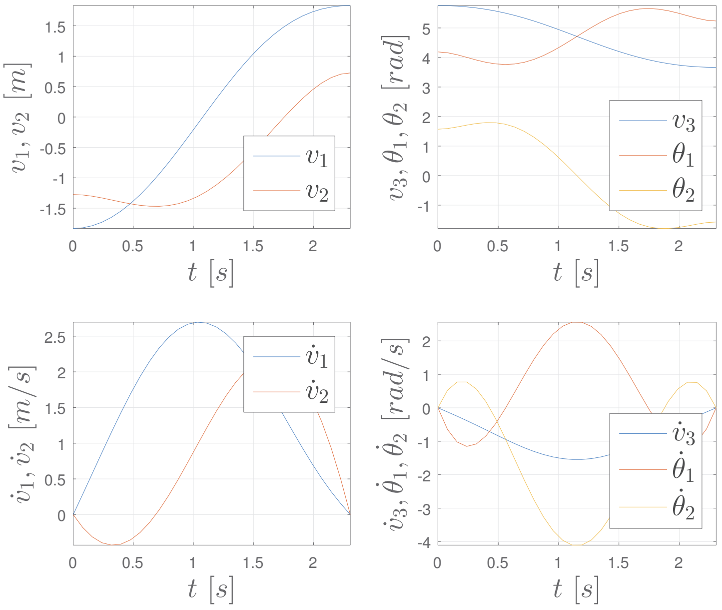

Figure 53: Flat outputs for two optimal set of design variable: solution S_3.

manipulator. In fact, due to cable interference, the orientation capabilities of the frame are limited.

However, the system is under-actuated since no motor can control the orientation of *Link 2* (θ_2). The links are coupled by a torsional spring whose constant is k_s.

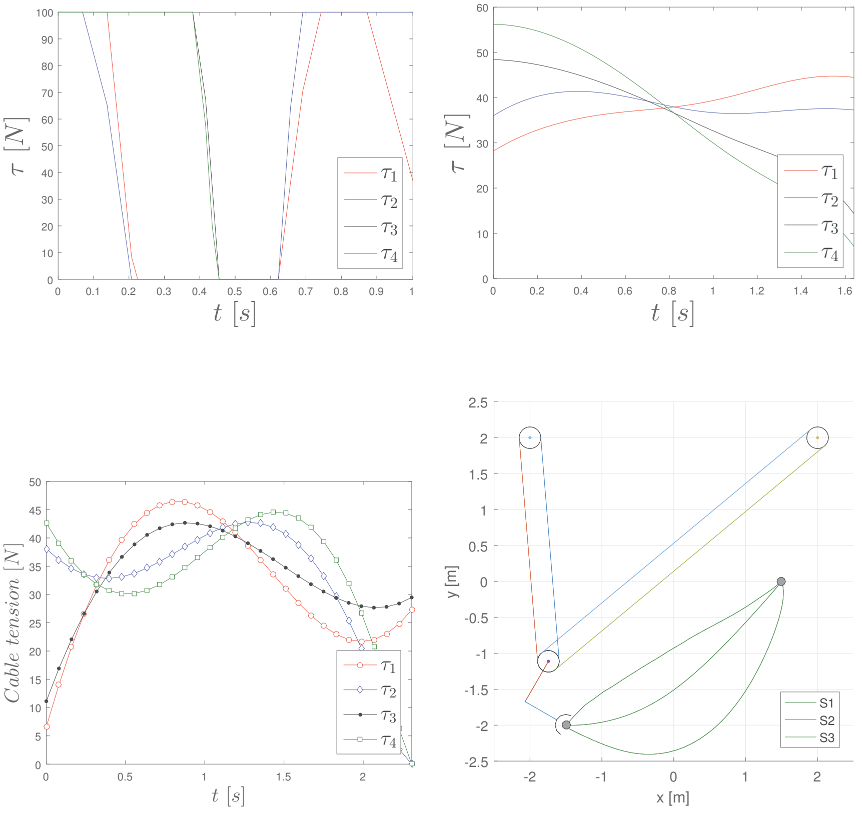

Figure 54: Cable tensions for three sets of design variable: (a) Solution S_1, (b) Solution S_2 and (c) Solution S_3. Optimal paths obtained for design solutions S_1, S_2 and S_3 (d).

Let us define the following transformations relative to the base frame $\{\mathbf{B}\} = \mathbf{O} - \mathbf{XYZ}$. The transformation from $\{\mathbf{B}\}$ to $\{\mathbf{o}\} = \mathbf{O_o} - \mathbf{xyz}$ is:

$$\begin{aligned}\mathbf{T_B^o} &= \mathbf{T_p}(x, y, x)\mathbf{T_z}(\alpha)\mathbf{T_y}(\beta)\mathbf{T_z}(\gamma)\\ &= \begin{bmatrix}1 & 0 & 0 & x\\ 0 & 1 & 0 & y\\ 0 & 0 & 1 & z\\ 0 & 0 & 0 & 1\end{bmatrix}\begin{bmatrix}c\alpha & -s\alpha & 0 & 0\\ c\alpha & c\alpha & 0 & 0\\ 0 & 0 & 1 & z\\ 0 & 0 & 0 & 1\end{bmatrix}\begin{bmatrix}c\beta & 0 & s\beta & 0\\ 0 & 1 & 0 & 0\\ -s\beta & 0 & c\beta & 0\\ 0 & 0 & 0 & 1\end{bmatrix}\begin{bmatrix}c\gamma & -s\gamma & 0 & 0\\ c\gamma & c\gamma & 0 & 0\\ 0 & 0 & 1 & 0\\ 0 & 0 & 0 & 1\end{bmatrix}\end{aligned} \tag{96}$$

$$\begin{aligned}\mathbf{R_B^o} &= \mathbf{R_z}(\alpha)\mathbf{R_y}(\beta)\mathbf{R_z}(\gamma)\\ &= \begin{bmatrix}c\alpha & -s\alpha & 0\\ c\alpha & c\alpha & 0\\ 0 & 0 & 1\end{bmatrix}\begin{bmatrix}c\beta & 0 & s\beta\\ 0 & 1 & 0\\ -s\beta & 0 & c\beta\end{bmatrix}\begin{bmatrix}c\gamma & -s\gamma & 0\\ c\gamma & c\gamma & 0\\ 0 & 0 & 1\end{bmatrix}\\ &= \begin{bmatrix}c\alpha\, c\beta\, c\gamma - s\alpha\, s\gamma & -s\alpha\, c\gamma - c\alpha\, c\beta\, s\gamma & c\alpha\, s\beta\\ c\alpha\, s\gamma + c\beta\, c\gamma\, s\alpha & c\alpha\, c\gamma - s\alpha\, c\beta\, s\gamma & s\alpha\, s\beta\\ -s\beta\, c\gamma & s\beta\, s\gamma & c\beta\end{bmatrix}\end{aligned} \tag{97}$$

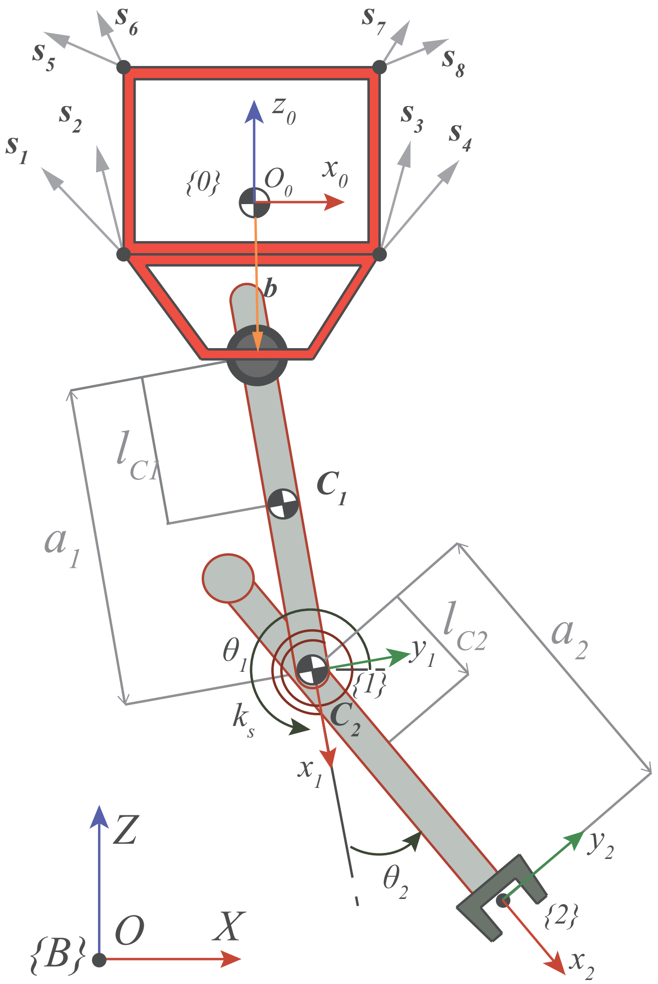

Figure 55: Model of 3D u-CSMMR.

The transformation from $\{\mathbf{B}\}$ to $\{\mathbf{1}\} = \mathbf{O_1} - \mathbf{xyz}$ is:

$$\mathbf{T_B^1} = \mathbf{T_B^0}\mathbf{T_p}(b)\mathbf{T_x}(\pi)\mathbf{T_z}(\theta_1)\mathbf{T_p}(a_1)$$
$$= \mathbf{T_B^0}\begin{bmatrix}1 & 0 & 0 & b_x\\ 0 & 1 & 0 & b_y\\ 0 & 0 & 1 & b_z\\ 0 & 0 & 0 & 1\end{bmatrix}\begin{bmatrix}1 & 0 & 0 & 0\\ 0 & c\pi & -s\pi & 0\\ 0 & s\pi & c\pi & 0\\ 0 & 0 & 0 & 1\end{bmatrix}\begin{bmatrix}c\theta_1 & -s\theta_1 & 0 & 0\\ c\theta_1 & c\theta_1 & 0 & 0\\ 0 & 0 & 1 & 0\\ 0 & 0 & 0 & 1\end{bmatrix}\begin{bmatrix}1 & 0 & 0 & a_1\\ 0 & 1 & 0 & 0\\ 0 & 0 & 1 & 0\\ 0 & 0 & 0 & 1\end{bmatrix} \tag{98}$$

where the position vector $\mathbf{b} = [b_x, b_y, b_z]^T$ represents the position of the actuated joint of *Link 1* respect to the reference $\{\mathbf{0}\}$.

The transformation from $\{\mathbf{B}\}$ to $\{\mathbf{C1}\} = \mathbf{C_1} - \mathbf{xyz}$ is:

$$\begin{aligned}\mathbf{T_B^{C1}} &= \mathbf{T_B^0}\mathbf{T_p}(b)\mathbf{T_x}(\pi/2)\mathbf{T_z}(\theta_1)\mathbf{T_p}(l_{c1}) \\ &= \mathbf{T_B^0}\begin{bmatrix}1 & 0 & 0 & b_x\\ 0 & 1 & 0 & b_y\\ 0 & 0 & 1 & b_z\\ 0 & 0 & 0 & 1\end{bmatrix}\begin{bmatrix}1 & 0 & 0 & 0\\ 0 & c\pi/2 & -s\pi/2 & 0\\ 0 & s\pi/2 & c\pi/2 & 0\\ 0 & 0 & 0 & 1\end{bmatrix}\begin{bmatrix}c\theta_1 & -s\theta_1 & 0 & 0\\ c\theta_1 & c\theta_1 & 0 & 0\\ 0 & 0 & 1 & 0\\ 0 & 0 & 0 & 1\end{bmatrix}\begin{bmatrix}1 & 0 & 0 & l_{c1}\\ 0 & 1 & 0 & 0\\ 0 & 0 & 1 & 0\\ 0 & 0 & 0 & 1\end{bmatrix}\end{aligned} \tag{99}$$

$$\mathbf{R_B^1} = \mathbf{R_{B0}}\mathbf{R_x}(\pi/2)\mathbf{R_z}(\theta_1) = \mathbf{R_{B0}}\begin{bmatrix}1 & 0 & 0\\ 0 & c\pi/2 & -s\pi/2\\ 0 & s\pi/2 & c\pi/2\end{bmatrix}\begin{bmatrix}c\theta_1 & -s\theta_1 & 0\\ c\theta_1 & c\theta_1 & 0\\ 0 & 0 & 1\end{bmatrix} \tag{100}$$

The transformation from $\{\mathbf{B}\}$ to $\{\mathbf{2}\} = \mathbf{O_2} - \mathbf{xyz}$ is:

$$\mathbf{T_B^2} = \mathbf{T_B^1}\mathbf{T_z}(\theta_2)\mathbf{T_p}(a_2) = \mathbf{T_B^1}\begin{bmatrix}c\theta_2 & -s\theta_2 & 0 & 0\\ c\theta_2 & c\theta_2 & 0 & 0\\ 0 & 0 & 1 & 0\\ 0 & 0 & 0 & 1\end{bmatrix}\begin{bmatrix}1 & 0 & 0 & a_2\\ 0 & 1 & 0 & 0\\ 0 & 0 & 1 & 0\\ 0 & 0 & 0 & 1\end{bmatrix} \tag{101}$$

The transformation from $\{\mathbf{B}\}$ to $\{\mathbf{C2}\} = \mathbf{C_2} - \mathbf{xyz}$ is:

$$\mathbf{T_B^{C2}} = \mathbf{T_B^1}\mathbf{T_z}(\theta_2)\mathbf{T_p}(l_{c2}) = \mathbf{T_B^1}\begin{bmatrix}c\theta_2 & -s\theta_2 & 0 & 0\\ c\theta_2 & c\theta_2 & 0 & 0\\ 0 & 0 & 1 & 0\\ 0 & 0 & 0 & 1\end{bmatrix}\begin{bmatrix}1 & 0 & 0 & l_{c2}\\ 0 & 1 & 0 & 0\\ 0 & 0 & 1 & 0\\ 0 & 0 & 0 & 1\end{bmatrix} \tag{102}$$

$$\mathbf{R_B^2} = \mathbf{R_B^1}\mathbf{R_z}(\theta_2) = \mathbf{R_B^1}\begin{bmatrix}c\theta_2 & -s\theta_2 & 0\\ c\theta_2 & c\theta_2 & 0\\ 0 & 0 & 1\end{bmatrix} \tag{103}$$

The pose of the tool center points is $\mathbf{T_T} \equiv \mathbf{T_{B2}}$. For the same position of the spool, the u-CDMMR allows to increase the reachable workspace compared to the CSPR. Alternatively, the system can reach a specified tool pose in multiple configurations.

The velocities relative to the base frame are:

$$\mathbf{v_{C_0}} = [\dot{x},\ \dot{y},\ \dot{z}]^T \tag{104}$$

$$\begin{aligned}\mathbf{v_{C_1}} &= \frac{\partial \mathbf{C_1}}{\partial x}\dot{x} + \frac{\partial \mathbf{C_1}}{\partial y}\dot{y} + \frac{\partial \mathbf{C_1}}{\partial z}\dot{z} + \frac{\partial \mathbf{C_1}}{\partial \alpha}\dot{\alpha} \\ &\quad + \frac{\partial \mathbf{C_1}}{\partial \beta}\dot{\beta} + \frac{\partial \mathbf{C_1}}{\partial \gamma}\dot{\gamma} + \frac{\partial \mathbf{C_1}}{\partial \theta_1}\dot{\theta}_1 + \frac{\partial \mathbf{C_1}}{\partial \theta_2}\dot{\theta}_2\end{aligned} \tag{105}$$

$$\begin{aligned}\mathbf{v_{C_2}} &= \frac{\partial \mathbf{C_2}}{\partial x}\dot{x} + \frac{\partial \mathbf{C_2}}{\partial y}\dot{y} + \frac{\partial \mathbf{C_2}}{\partial z}\dot{z} + \frac{\partial \mathbf{C_2}}{\partial \alpha}\dot{\alpha} \\ &\quad + \frac{\partial \mathbf{C_2}}{\partial \beta}\dot{\beta} + \frac{\partial \mathbf{C_2}}{\partial \gamma}\dot{\gamma} + \frac{\partial \mathbf{C_2}}{\partial \theta_1}\dot{\theta}_1 + \frac{\partial \mathbf{C_2}}{\partial \theta_2}\dot{\theta}_2\end{aligned} \tag{106}$$

The angular velocity of the reference frame {**0**} is:

$$\omega_0^0 = \begin{bmatrix} \dot{\beta}\ s\gamma - \dot{\alpha}\ c\gamma\ s\beta \\ \dot{\beta}\ c\gamma + \dot{\alpha}\ s\beta\ s\gamma \\ \dot{\gamma} + \dot{\alpha}\ c\beta \end{bmatrix} \tag{107}$$

The angular velocities of the reference frames {**1**} and {**2**} can be derived as follows: [40]:

$$\omega_i^i = {\mathbf{R}_{i-1}^{i}}^{T}(\omega_{i-1}^{i-1} + [\phi_x, \phi_y, \phi_z]^T) \tag{108}$$

As a consequence:

$$\omega_1^1 = \mathbf{R_1^0}(\omega_0^0 + \mathbf{R_x}(\pi/2)[0, 0, \dot{\theta}_1]^T) \tag{109}$$
$$\omega_2^2 = \mathbf{R_2^1}(\omega_1^1 + [0, 0, \dot{\theta}_2]^T) \tag{110}$$
$$\tag{111}$$

The angular velocities relative to the base frame are:

$$\omega_0 = \omega_0^B = {\mathbf{R_B^0}}^T \omega_0^0 \tag{112}$$
$$\omega_1 = \omega_1^B = {\mathbf{R_B^1}}^T \omega_1^1 \tag{113}$$
$$\omega_2 = \omega_2^B = {\mathbf{R_B^2}}^T \omega_2^2 \tag{114}$$

Using Lagrangian's approach, the general form of the equations of motion for the CDMMR can be obtained in Cartesian space [40]. The kinetic energy is:

$$\begin{aligned} KE = &\frac{1}{2}m_1\mathbf{v_{C_0}^T}\mathbf{v_{C_0}} + \frac{1}{2}m_1\mathbf{v_{C_1}^T}\mathbf{v_{C_1}} + \frac{1}{2}m_2\mathbf{v_{C_2}^T}\mathbf{v_{C_2}} + \\ &\frac{1}{2}\omega_0^T I_0 \omega_0 + \frac{1}{2}\omega_1^T I_1 \omega_1 + \frac{1}{2}\omega_2^T I_2 \omega_2 \end{aligned} \tag{115}$$

where $I_0 = \mathbf{R_0^B} I_0^0 {\mathbf{R_0^B}}^T$, $I_1 = \mathbf{R_1^B} I_1^1 {\mathbf{R_1^B}}^T$ and $I_2 = \mathbf{R_2^B} I_2^2 {\mathbf{R_2^B}}^T$ are the inertia tensors of the bodies w.r.t. the base frame. The masses of the bodies are m, m_1, m_2 whereas I_0, I_1 and I_2 are the inertia tensors of the bodies w.r.t. their centers of mass. The potential energy is:

$$PE = m{\mathbf{g_0}}^T\mathbf{C_0} + m_1{\mathbf{g_0}}^T\mathbf{C_1} + m_2{\mathbf{g_0}}^T\mathbf{C_2} + \frac{1}{2}k_s\theta_2^2 \tag{116}$$

where $\mathbf{g_0} = [0, -g, 0]^T$.

The control input of the under-actuated system is the vector of the cable tensions $\boldsymbol{\tau} = [\tau_1, \tau_2, \tau_3, \tau_4, \tau_5, \tau_6, \tau_7, \tau_8]^T$ which can be mapped into the resultant wrench $\mathbf{u} = [u_1, u_2, u_3, u_4, u_5, u_6]^T$ through the structure matrix $\mathbf{S} \in \mathbb{R}^{\mathbf{3}\times\mathbf{4}}$. Furthermore, a torque input u_7 is required for the joint angle θ_1.

The state-space equation is given by:

$$\mathbf{M}(\mathbf{q})\ddot{\mathbf{q}} + \mathbf{V}(\mathbf{q}, \dot{\mathbf{q}}) + \mathbf{G}(\mathbf{q}) = \mathbf{u} = \begin{bmatrix} \mathbf{S} & \mathbf{0}_{6\times1} & \mathbf{0}_{6\times1} \\ \mathbf{0}_{1\times6} & 1 & 0 \\ \mathbf{0}_{1\times6} & 0 & 1 \end{bmatrix} \begin{bmatrix} \boldsymbol{\tau} \\ \kappa_1 \\ 0 \end{bmatrix} \tag{117}$$

where k_1 is the torque required by *Link 1*.

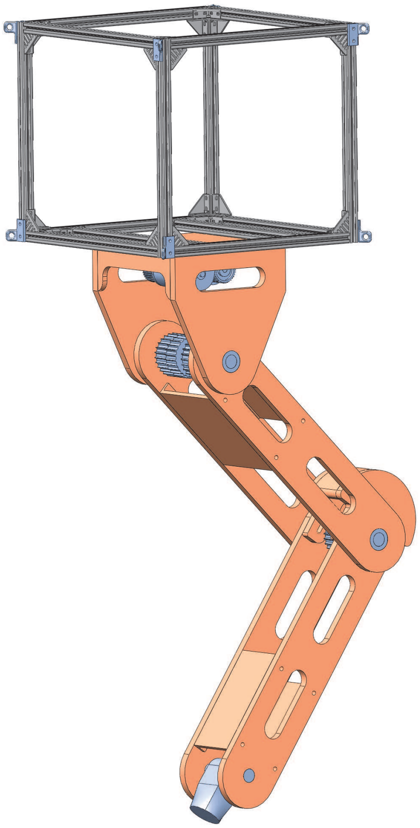

Figure 56: CAD Model of 3D u-CSMMR.

4.6.1 *Differentially flat design*

The system is flat and the flat outputs can be selected as:

$$\begin{aligned} v &= [v_1,\ v_2,\ v_3,\ v_4,\ v_5,\ v_6,\ v_7] \\ &= \Big[x,\ y,\ z,\ \alpha,\ \beta,\ \gamma,\ \theta_1 + \theta_2]\Big] \end{aligned} \tag{118}$$

The value of θ_2 can be expressed as follows:

$$\begin{aligned} \theta_2 &= \Phi(v_4, v_5, v_6, v_7, \dot{v}_4, \dot{v}_5, \dot{v}_6, \ddot{v}_4, \ddot{v}_5, \ddot{v}_7) \\ &= \frac{1}{k_s}\Big[I_{2xx}b_1 + I_{2yy}b_2 + I_{2zz}b_3 + I_{2xy}b_4 + I_{2xz}b_5 + I_{2yz}b_6 \\ &\quad - (A_4\ddot{v}_4 + A_5\ddot{v}_5 + A_6\ddot{v}_6 + A_7\ddot{v}_7)\Big] \end{aligned} \tag{119}$$

where the expression of b_1, b_2, b_3, b_4, b_5, b_6, A_4, A_5, A_6 and A_7 are reported in Appendix A.

The value of θ_1 can be derived as follows:

$$\theta_1 = v_7 - \Phi(v_4, v_5, v_6, v_7, \dot{v}_4, \dot{v}_5, \dot{v}_6, \ddot{v}_4, \ddot{v}_5, \ddot{v}_7) \tag{120}$$

Using the differential flatness proprieties established in this section, it is possible to control the system for a point-to-point movement. However, only an ideal differentially flat system can be perfectly controlled with a trajectory that is consistent with its dynamics. In reality,

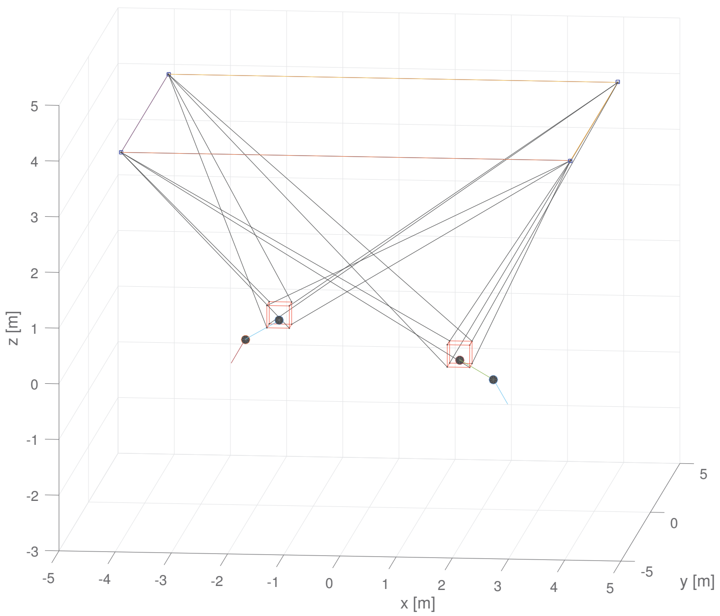

Figure 57: Initial and final position of the micro-macro robot.

the system can be affected by uncertainties that affect the dynamics of the system. Next section aims at analyzing a differential flatness based controlled using the concept of robust control.

4.6.2 *Illustrative example*

In this section, we present an illustrative example that simulate a trajectory for the micro-macro robot. Figure 57 illustrate the initial point, $P_i = [1.5, 1.0, -0.5, 0, 0, -30, -30]$, and the final point, $P_f = [-1.5, -1.0, 0.5, 0, 0, 150, 30]$. Initial and final velocities are null. The total time of the movement is $T = 3$ s. Using the diffeomorphism derived by Eq. (118),(119) and (120) it is possible to compute the initial and final flat output variables. Afterwards, a trajectory in the flat output space can be planned as shown in Fig. 58. The trajectory in the state space variables can be calculated using the inverse of the diffeomorphism. Finally, cable tensions, forces and moments can be computed using the inverse dynamics as shown in Fig. 60.

4.7 CONCLUSION

This chapter presented the model of a planar under-actuated Cable-Driven Micro-Macro Robot (u-CDMMR). The system consists of a Cable-Suspended Parallel Robot whose end-effector is a two-link passive serial manipulator. The kinematic and dynamic models were presented and the *differential flatness* framework was applied to make the system controllable for point-to-point movements. The application of

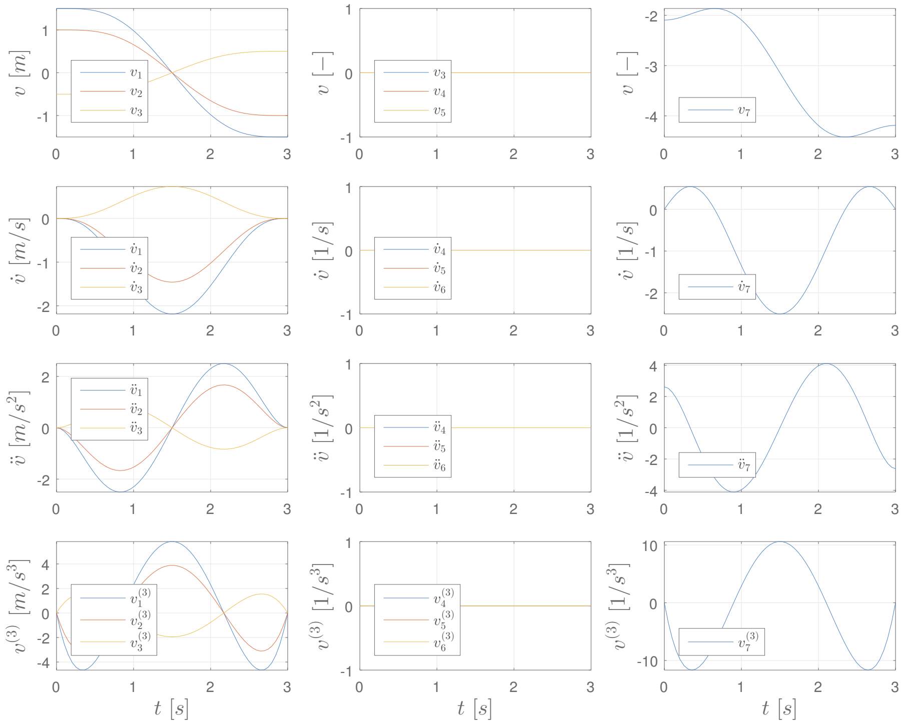

Figure 58: Flat output variables for the planned trajectory.

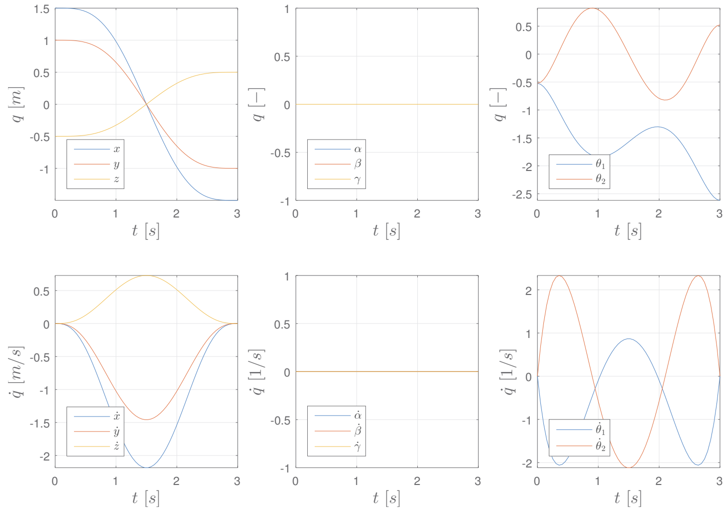

Figure 59: State space variables for the planned trajectory.

differential flatness for an under-actuated end-effector of a cable-driven robots is a first novelty of this work.

The serial manipulator allows to reduce the risk of collision between the cables and the surrounding obstacles. As a consequence, it increase the reachable workspace of a traditional CSPR. Greenhouse operations like precise fertilization, spraying and inspection are potential applications of u-CDMMRs since the do not involve modification of the mass distribution which is a fundamental requirement for the *differential flatness* approach.

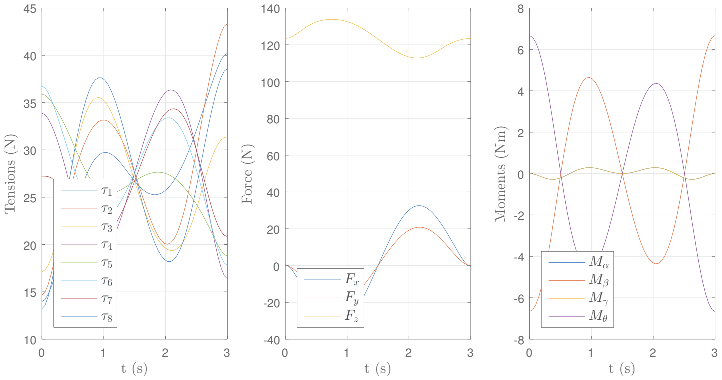

Figure 60: Tensions, forces and moments for the planned trajectory.

The work proposed a novel optimization framework for the design of u-CDMMRs. Given a point-to-point movement to execute, a multi-objective optimization was used to minimize two objective functions simultaneously: the movement time and the control effort required by the actuators. Optimal time-energy control was applied to compute the optimal trajectory. This approach allows to analyze the effect of the design parameters, such as link dimensions, mass distributions, and spring stiffness on the performance of the system.

An illustrative case-study was analyzed for a representative point-to-point movement. The result of the multi-objective optimization allows to define the Pareto front, which is a set of optimal design solutions that minimize simultaneously the objective functions. Compared to the same movement performed by a CSPR, the u-CDMMR allows to reduce the control effort for high-speed movements. Among the selected design variables, the spring constant and the length of *Link 1* have the greatest influence on the objective functions. In particular, the longer the link, the fastest the movement. This is mainly due to a better cable configuration inside the workspace, which allows to exert higher wrenches. Furthermore, the lower the spring constant, the lower the control effort, since the system can exploit the oscillation of *Link 2* to pump energy into it.

Even if the system can be designed for tasks requiring specific point-to-point movements, it is important to point out that the design process for an u-CDMMR must consider a complete set of movements to be effective. Several movements can be tested by comparing the corresponding Pareto fronts obtained from the optimization presented in this work.

Future works will improve the optimization framework considering other design variables which can affect the performance of the system, such as mass distribution, weight coefficients for the time-energy optimal control, and path constraints. Furthermore, the control of under-actuated systems with variable mass distribution (pick and place applications) will be addressed using the concept of robust control.

5

DESIGN OF ICABOT

This chapter illustrates the design of a novel family of Intelligent CAble-driven paralle roBOTs (ICABOTs) whose architecture and control will maximize the robot adaptability to the task to be performed and the environment in which the robot is intended to operate. The results of the ICABOT project, which include software tools for the design and control of cable robots, will have a strong impact on practical applications like pick and place applications

The development of ICABOT has been based on the concept of Concurrent Engineering and all the aspects of the design process are illustrated in details.

5.1 DESIGN OVERVIEW

The aim of the ICABOT project is to develop new methodologies and algorithms for the design and control of a novel family of cable-driven parallel robots (CDPRs), which we call Intelligent CAble-driven paralle roBOTs (ICABOTs), whose architecture and control will maximize the robot adaptability to the task to be performed and the environment in which the robot is intended to operate. ICABOTs are supposed to quickly adapt their geometry to the task at hand, before and/or during task execution, in order to maximize performances and minimize energy consumption. On the one hand, the ICABOT is expected to execute, with respect to a traditional robot, a given trajectory with better cable-tension distribution and reduced power consumption, thus allowing less and/or smaller actuators to be installed. On the other hand, with a given hardware, the ICABOT is expected to achieve higher dynamic performances and be more dexterous. The new robotic technology has three main characteristics:

1. Design software. A design software, developed to derive the optimal configuration of the modular architecture according to the specific tasks to be executed and the environmental limitations resulting from the application (e.g., the geometry and the obstacles in an apartment room). The design software, according to a selectable set of optimization criteria (e.g., minimum task execution time, minimum energy consumption, maximum kinematic accuracy, etc.) and to a user-defined set of motion tasks, will provide indications on the number of cables and moving shuttles to be employed and their disposition within the workspace.

2. Modular mechanical architecture. Simple mechanical design for rapid deployment process: once the geometry configuration pa-

rameters are defined, the designer must be able to build the desired CDPR quickly by choosing among a set of standard modules, and by combining them according to the specifications provided. The standard modules consist of winches, movable pulley blocks and movable anchor points. Cables may be connected one to the other on variable anchor points, thus creating a web-based distributed network, in which cable disposition with respect to the end-effector (EE) may be varied either offline or online. The actuation of selected cables may be enabled/disabled depending on the dynamic performances to be achieved along the required trajectory.

3. Control architecture. A control architecture able to adapt robot geometry and motor input commands in real-time, with the aim of modifying cable configuration and cable-tension distribution (including the enable/disable feature) in order to gain the highest attainable performance during the execution of the motion task. Particular attention will be devoted not only to the management of robot adaptability, which is the main goal of the project, but also to obtaining the desired levels of kinematic and of force accuracy, which is an open and debated problem with cable based robots

The development of ICABOT has been based on the concept of Concurrent Engineering, which is introduced in the section.

5.2 CONCURRENT ENGINEERING

The design process of a mechatronic system requires a multi-disciplinary and holistic development process [109]. Traditional sequential design process can still be considered as a standard in industry but it lacks of integration able to support multi-disciplinary design during the whole design process. This design process has been proven to be unsuitable for modern mechatronic design because it increases the design cost and development leading-time. The development of ICABOT has been based on a different paradigm: *Concurrent Engineering* (CE). Lawson and Karandikart [110] defined CE as a systematic approach to the integrated, concurrent design of products and their related processes, including manufacture and support. This approach is intended to cause the developers, from the outset, to consider all elements of the product life cycle from conception through disposal, including quality, cost, schedule and user requirements. CE is based on the idea that all the elements of a product's life-cycle, from functionality, producibility, assembly, testability, maintenance issues, environmental impact and finally disposal and recycling, should be taken into careful consideration in the early design phases. The method is also called *Simultaneous Engineering* because all the design activities should occur at the same time. The cuncurrent nature of this approach aims at increasing productivity and product quality [111] by discovering issues and making redesigns early in the design process when the project is still flexible. Figure 61 reports the design process of mechatronic systems based on CE. Three main aspects of a mechatronic system are shown: software, electrical/electronic and mechanical. These three aspects must be simultaneously analyzed by the people involved in the project:

- The software development aims at defining the task to be satisfied and how this code is going to interact with the hardware. The interaction between software and hardware is a main aspect since it characterizes the control architecture and it affects the design of the electrical system.
- The electrical/electronic design of the system aims at defining the circuit design, electrical circuit protections, motor definition, etc. The relationship with the mechanical team is fundamental for the implementation of the electro-mechanical system.
- The mechanical design process starts with a conceptual design of the system in order to define the kinematics and dynamics requirements. The possibility to simulate the dynamic system is a powerful tool to characterize the components of the system and allows the designer to select the actuators, perform finite element analysis and define the manufacturing process. Feedback information is adopted into the original configuration to make adjustments in the design.

In the next section, a conceptual design of the system is presented as well as a general layout of the robot. The goal is to characterize the general requirements of the system and illustrate the design process of ICABOT from the mechanical, electrical and software point of view.

5.3 GENERAL LAYOUT OF THE ROBOT

ICABOT is a scaled-prototype of CDPR whose purpose is to validate the design and control methodologies proposed in the previous chapters. The system is conceived to be reconfigurable but a basic layout must be defined in order to characterize the design of the mechanical parts and perform the motor sizing. As a result, the initial layout of ICABOT consists of eight suspended cables connected to an end-effector as shown in Fig. 62. The cables pass through the pulley blocks to be redirected towards the winches. The winches are then driven by rotational motors. The configuration of the cable anchor points is based on the optimal layout presented by Lamaury et al. [61]. This layout can reduce collision risks between cables and obstacles since

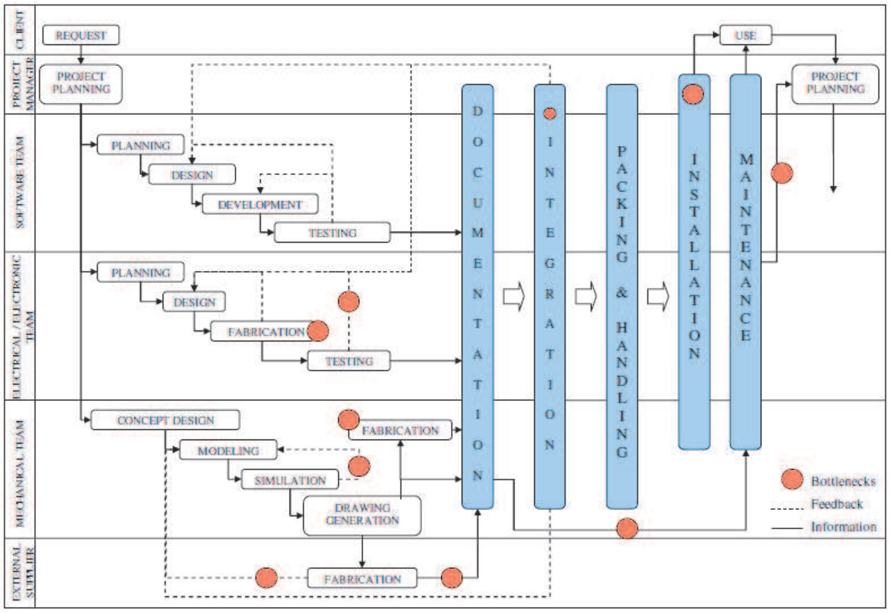

Figure 61: Concurrent Engineering design for mechatronic systems [112]

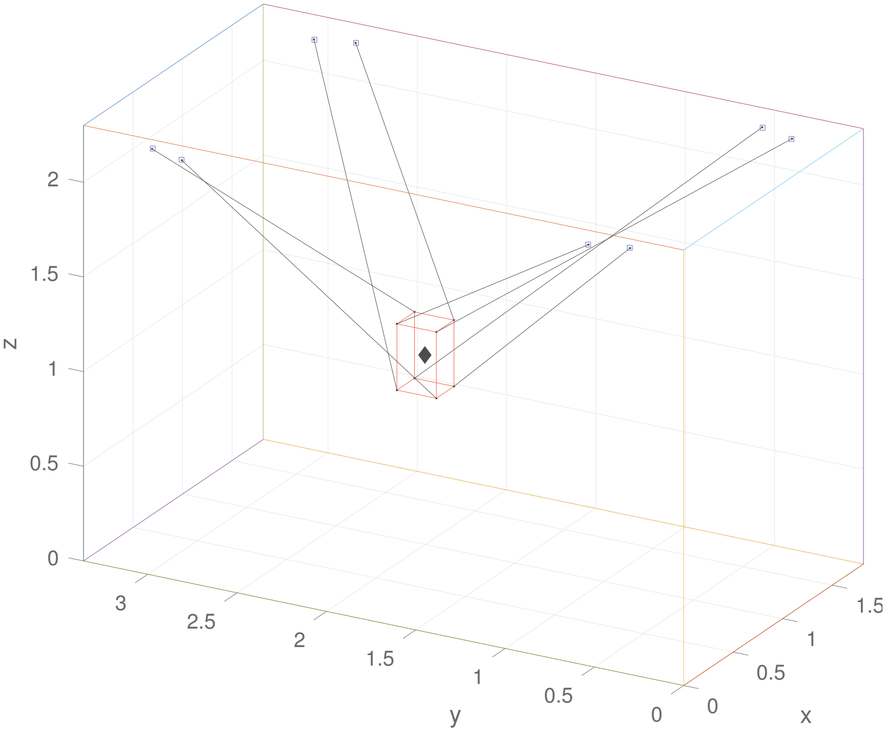

Figure 62: Layout of ICABOT. The system is a Cable-Suspended Parallel Robot.

the mobile platform is suspended with cables connected to the ceiling, making cable-free the workspace below the platform.

Winches, motors and pulley blocks must be reconfigurable in order to be moved inside the workcell. However, to guarantee an optimal

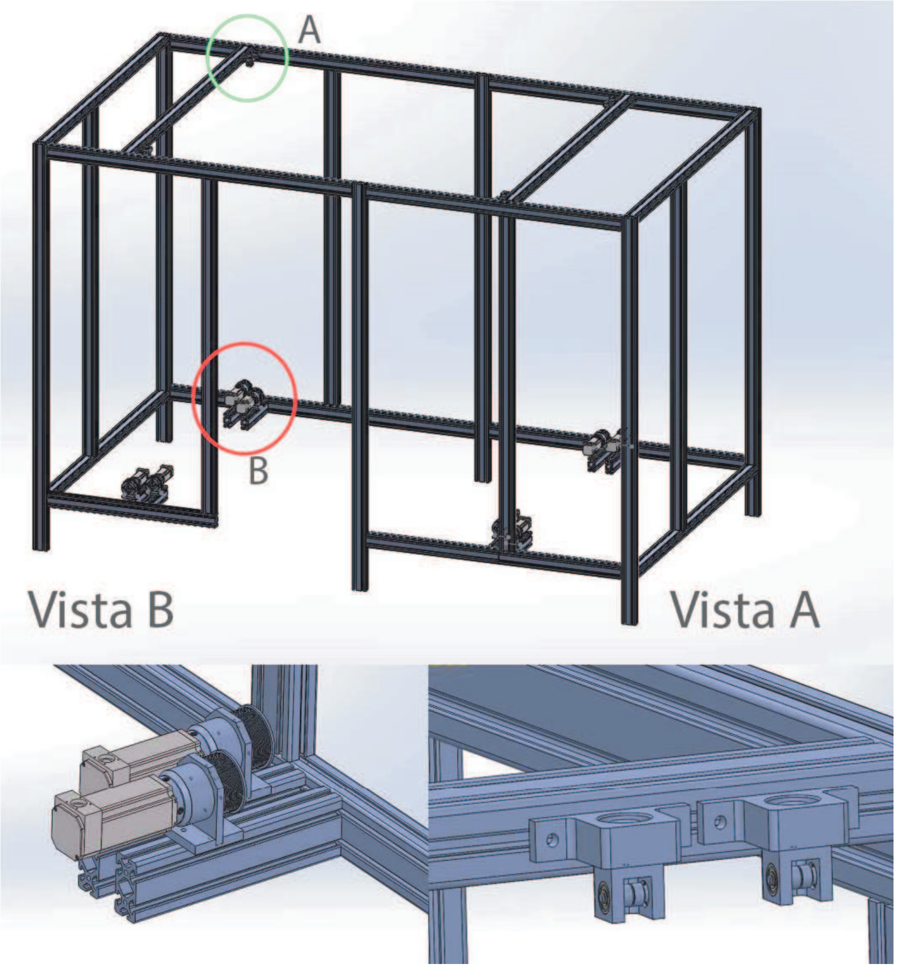

Figure 63: Layout of ICABOT.

wrapping of the cables around the winches, the distance between pulley blocks and winches must not be too small. The maximum dimensions of the available workcell are 1840 × 3200 × 2300 mm. Motors, winches and pulley blocks can be placed inside the workcell as shown in Fig. 63.

A first prototype of ICABOT developed at the Mechatronics laboratory of the University of Padua is shown in Fig. 62. Once defined the general layout of the system, it is possible to perform simulations of its kinematics and dynamics using the CDPR simulator described in the next section.

5.4 CDPR SIMULATOR

The aim of this section is to introduce a software platform for the analysis and simulation of CDPRs. Researchers developed several techniques for the analysis of CDPRs but they are typically implemented and evaluated only on the CDPRs available in the research group. Furthermore, it is difficult and time-consuming to perform different

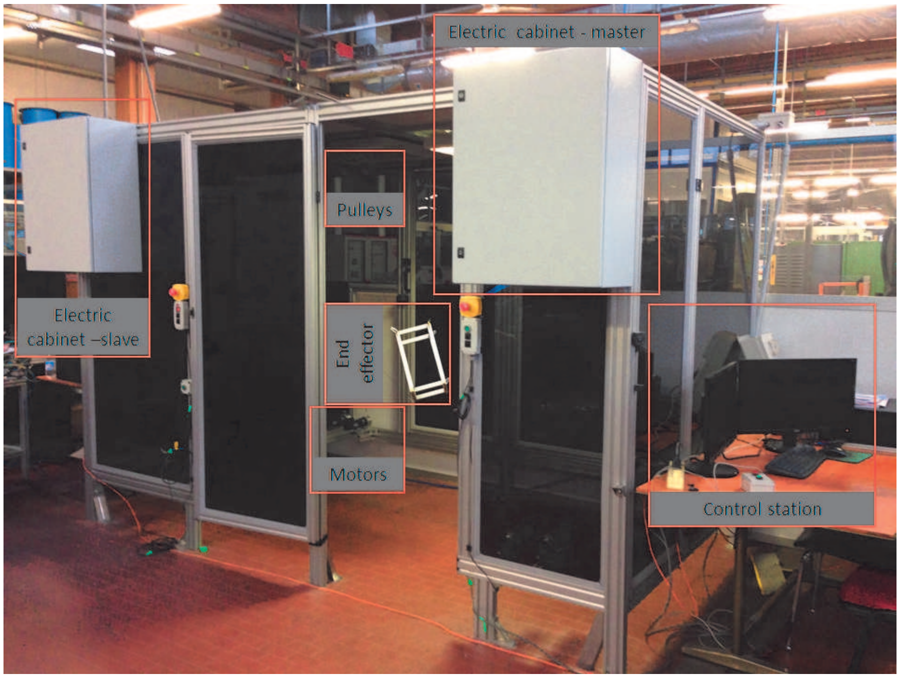

Figure 64: Prototype of ICABOT developed at the University of Padua.

types of analysis and compare different implementations, particularly in the case of CDPRs which are highly reconfigurable. The possibility to simulate and test multiple configurations of a cable robot is a promising way to improve versatility and reduce the design time. In fact, one of the bottlenecks of the design process illustrated in Fig. 61 is the possibility to modify the mechanical model based on dynamic simulations of the robot.

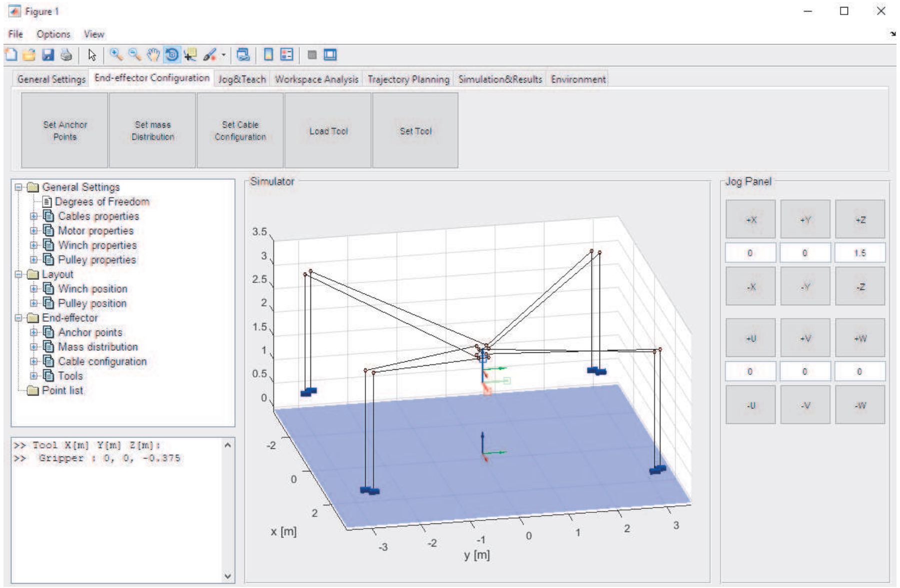

```
>> Tool X[m] Y[m] Z[m]:
>>  Gripper : 0, 0, -0.375
```

Figure 65

The simulator is developed in Matlab [113] using a modular object-oriented programming (OOP) paradigm. The simulators has three main goals:

- provide a graphical user interface (GUI) allowing a simple and intuitive design process;
- allow a quick configuration of a CDPR;
- perform different type of analysis such as forward/inverse kinematics, inverse dynamics, workspace analysis and trajectory planning.

The abstract base class *guiCLASS* allows the user to interact with the simulator through a GUI (Fig. 65) which is developed based on the state-of-the-art software for Computer-Aided Engineering (CAE). The class, *cdpr*, allows to define the model of the cable driven robot. The class is characterized by different types of methods for the configuration of the CDPR, the analysis of the system and the simulation of movements as shown in Fig. 66. The software architecture is conceived to be modular, in the sense that new features can be easily included.

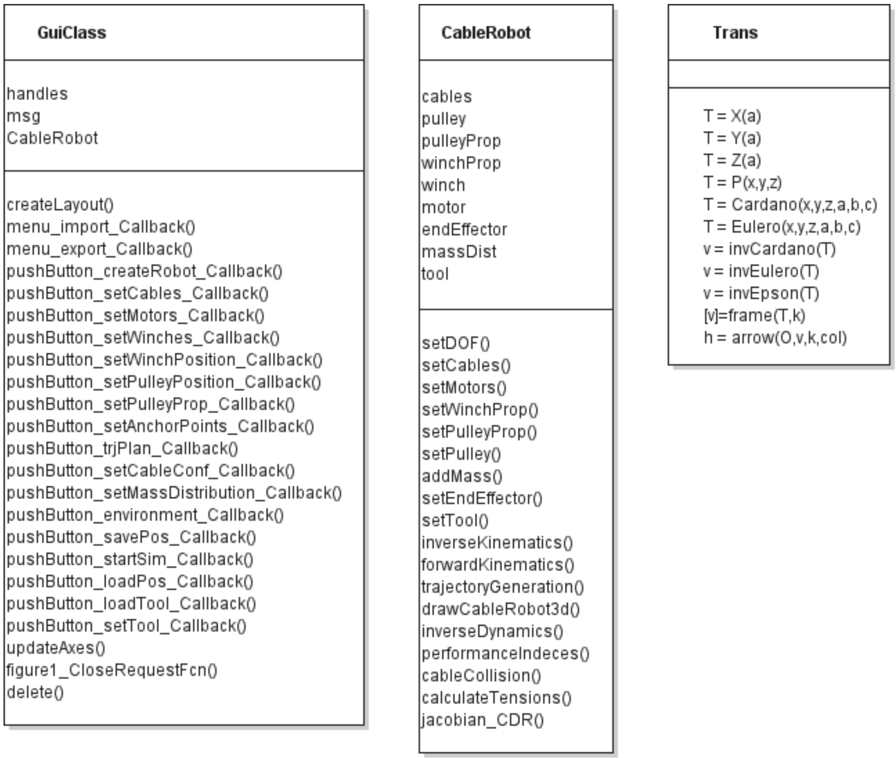

Figure 66: UML diagram of the Cable Robot Simulator.

In order to characterize the mechanical model of a CDPR, the user must define:

- Position and proprieties of the winches;

- Position and proprieties of the pulleys, which define the cable exit points;
- Position of the cable anchor points on the end-effector;
- Mass distribution of the end-effector;
- Reconfigurability of the cable exit points;
- Reconfigurability of the cable anchor points

Currently the software has some limitations. For example, the cables are modeled as ideal cables, which means they are massless rigid cables with infinite stiffness. Only a set of attachment locations and a maximum force bounds for the cables need to be defined. Future work aims at improving the cable model considering the elasticity of the cables using linear spring cables or variable stiffness cables.

Once the mechanical model of the CDPR is defined, it is possible to perform the following analysis:

- Inverse kinematics (IK). The IK problem is stated in Sec. 2.2 and computed using the approach proposed by Williams et al. [63].
- Forward kinemtics (FK). The forward kinemtics consists in computing the pose of the end-effector for a given set of cable lengths. The problem is non-trivial and can be solved suing the approach proposed by Pott et al. [64].
- Inverse dynamics (ID). The ID problem consists in computing a set of cable tensions subjected to constraints (tension must be positive, but lower than a maximum value) to produce a desired trajectory of the end-effector. Due to actuation redundancy of cable-driven systems, several methods are available for the tension distribution [67, 114, 115].
- Manipulability. Manipulability is a widely adopted index as a measure of the performance of a robotic system in the force domain, usually described by means of polytopes [68].

The possibility to simulate the dynamics of the system for a set of linear movements is a powerful tool to evaluate the motor requirements in terms of torque and angular velocity. The procedure for the motor sizing is described in the next section.

5.5 MOTOR SIZING AND SELECTION

The goal of this section is the sizing of the motors required to actuate ICABOT. Once defined a set of target linear movements, it is possible to compute the tension of the cables required to drive the end-effector. The simulation of the movements allows to compute the requirements in terms of torque and angular velocity. Several variables were considered:

- winch radius;
- time law;
- total time of movement;
- position of the initial and final points;
- mass and configuration of the end-effector.

Using the ID algorithms implemented in the simulator, a set of linear movements was tested with the purpose of computing the values of torque (κ), angular velocity (ω) and angular acceleration ($\dot{\omega}$) to apply to the winches. These values allow to characterize the motor requirements in terms of:

- maximum (peak) values: κ_{max}, ω_{max} and $\dot{\omega}_{max}$;
- root mean square values: κ_{max}, ω_{max} and $\dot{\omega}_{max}$.

The peak values are necessary to avoid emergency stops, mechanical failures or excessive control errors. On the other hand, root-mean-square values are necessary to avoid motors overheating. Thus, the motor will be able to withstand the highest estimated loads for long time intervals, without thermal issues.

An initial sensitivity analysis of the results was conducted with the purpose of fixing some parameters and reduce the number of simulations to perform. As a consequence, the following choices were made:

- The winch radius affects the torque and the angular velocity required to drive the cables. In particular, the higher the radius, the higher the torque required to actuate the winch. On the other hand, the higher the radius, the lower the angular velocity. As a result, $r_p = 35\ mm$ was consider an optimal trade-off;
- Trapezoidal acceleration profile was selected to avoid undesired jerk;
- A reasonable total time of movement for a linear movement of $1.5\ m$ was considered to be $T = 1\ s$;
- The total mass of the end-effector was fixed to $10\ kg$. The total mass considers the mass of the main frame and the mass of the load to carry.

5.5.1 *Simulation results*

A set of linear movements was tested to calculate torque (κ_{max}, κ_{rms}), angular velocity (ω_{max}, ω_{rms}) and angular acceleration ($\dot{\omega}_{max}$, $\dot{\omega}_{rms}$) required to actuate the winches. Table 17 defines the layout of the system based on the notation illustrated in Sec. 2.2 whereas Table 10a and Fig. 68 report the trajectory parameters that characterize one of the most demanding movements. Fig. 69, 70, 71 72 illustrate the results of the simulation. Table 10b summarizes the results in terms of torque, angular velocity and angular acceleration.

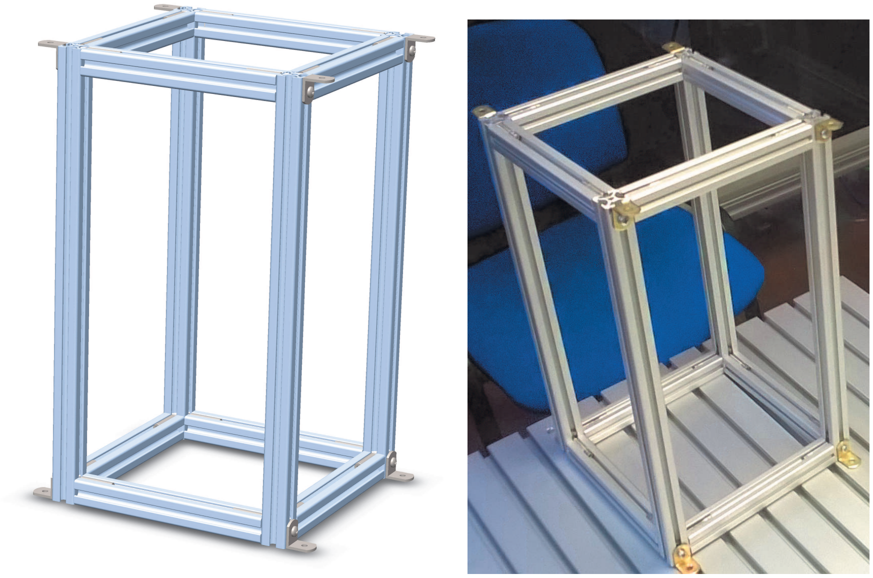

Figure 67: CAD model (a) and prototype (b) of a the end-effector used for the motor sizing and the calibration of the system.

The values of torque and angular speed obtained from the simulations are the requirements to actuate the winches. The *Principle of virtual works* can be used to compute the requirements in terms of torque and angular speed required by the motors:

$$M = J\dot{\omega}k + \frac{\kappa}{\eta k} \qquad \textit{with} \qquad J = J_m + J_{br} + J_f \tag{121}$$

$$n = \omega\, k \tag{122}$$

where κ and ω are the torque and the angular velocity applied to the winch, respectively. k is the gear ratio whereas M and n are the torque and the angular velocity applied by the motor. J_m, J_{br} and J_f are the inertia of the motor, the inertia of the brake and the inertia of the gearbox, respectively. η represents the efficiency of the gearbox. These values can be found in the technical documentation provided by the manufacturer. The model of motor-gearbox-winch is illustrated in Fig. 73.

Table 8: (a) Cable exit points A_i and cable anchor points B_i. (b) Kinematic and inertial parameters of the end-effector shown in Fig. 67.

Parameter	Value [m]
${}^{O}A_1, {}^{O}A_5$	$(0, 0.5, 2.21)$
${}^{O}A_2, {}^{O}A_6$	$(1.815, 0.5, 2.21)$
${}^{O}A_3, {}^{O}A_7$	$(1.815, 2.87, 2.21)$
${}^{O}A_4, {}^{O}A_8$	$(0, 2.87, 2.21)$
${}^{G}B_1$	$(d_x, -d_y, dz)$
${}^{G}B_2$	(d_x, d_y, dz)
${}^{G}B_3$	$(-d_x, d_y, dz)$
${}^{G}B_4$	$(-d_x, -d_y, dz)$
${}^{G}B_5$	$(-d_x, d_y, dz)$
${}^{G}B_6$	$(-d_x, -d_y, dz)$
${}^{G}B_7$	$(d_x, -d_y, dz)$
${}^{G}B_8$	(d_x, d_y, dz)

(a)

Parameter	Value	Unit
m	10	kg
I_{xx}	0.16	kgm^2
I_{yy}	0.16	kgm^2
I_{zz}	0.08	kgm^2
I_{xy}, I_{xz}, I_{yz}	0, 0, 0	kgm^2
d_x	0.178	m
d_y	0.220	m
d_z	0.350	m

(b)

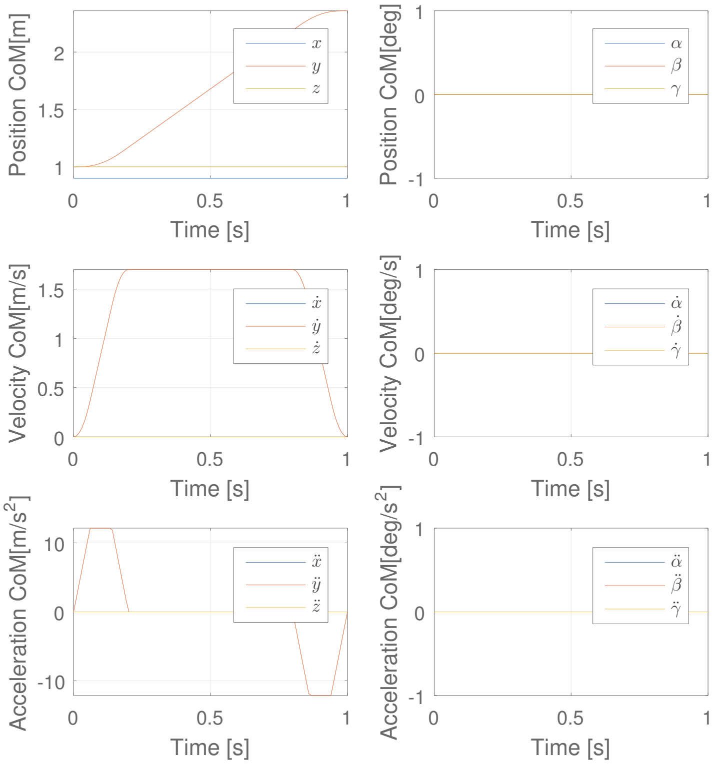

Figure 68: Trajectory for the linear movement tested.

In the next section, the results of the simulation are used to chose the most suitable gear-motor for the robot.

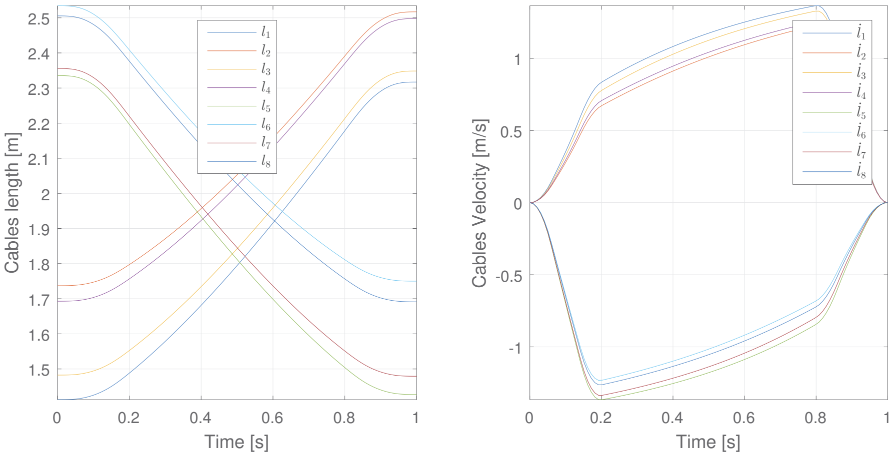

Figure 69: Cables length and cable velocity for the linear movement tested

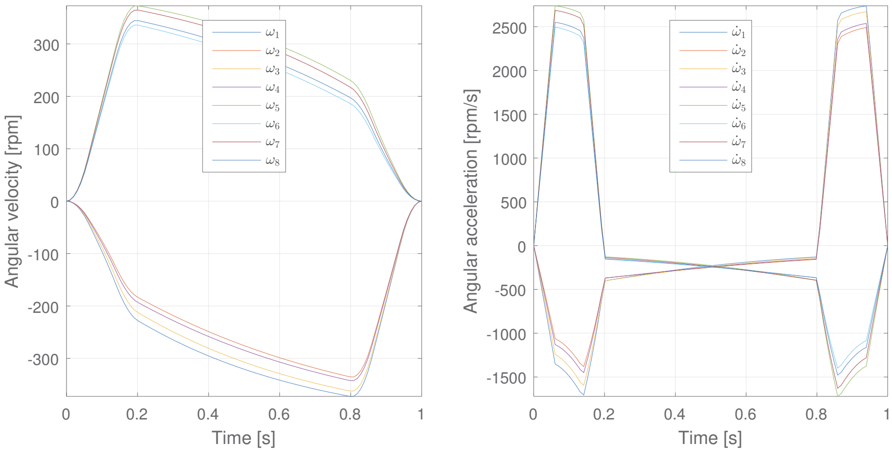

Figure 70: Angular velocity and angular acceleration of the winches for the linear movement tested

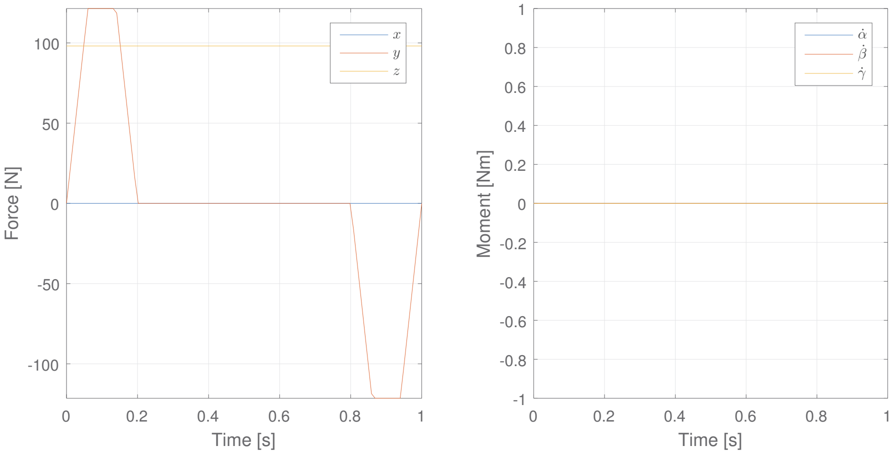

Figure 71: Force and Moments applied by the cable to the CoM of the end-effector.

5.5.2 *Gear-motors sizing*

For economical reasons, B&R was selected as motor provider. The 8LVB motor series with direct-mount gearbox integrates all mechan-

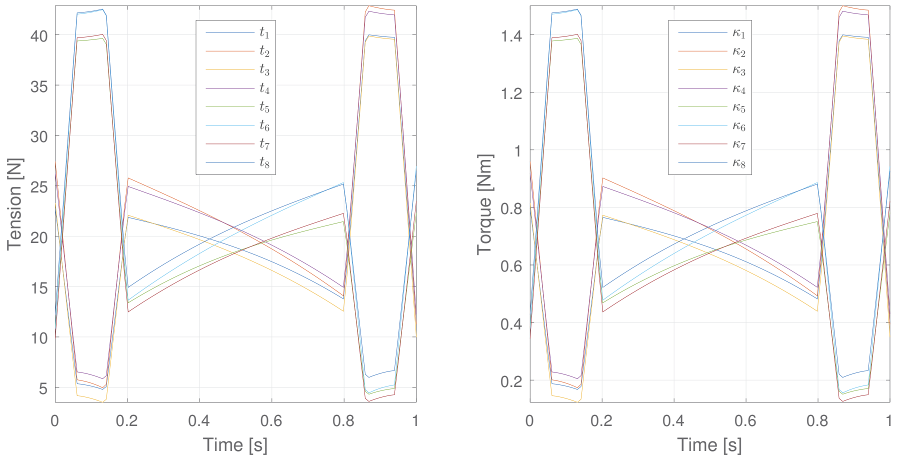

Figure 72: Cable tensions and winch torques for the linear movement tested.

Table 9: (a) Trajectory parameters. (b) Results of the ID.

Parameter	Value	Unit
${}^{O}P_{in}$	$(0.9, 1, 1)$	m
${}^{O}P_{fin}$	$(0.9, 2.36, 1)$	m
α	0	deg
β	0	deg
γ	0	deg
T	1.0	s

(a)

Parameter	Value	Unit
κ_{max}	1.53	Nm
κ_{rms}	0.83	Nm
ω_{max}	374.55	rpm
ω_{rms}	275.43	rpm
$\dot{\omega}_{max}$	2748.5	rpm/s^2
$\dot{\omega}_{rms}$	1109.5	rpm/s^2

(b)

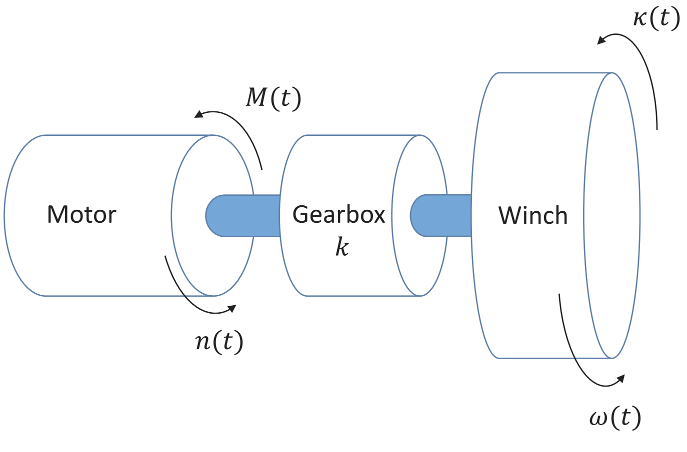

Figure 73: Model of motor, gearbox and winch.

ical and electrical components in the smallest space possible. This makes this series optimally suited for the design of ICABOT.

The choice of the gear motor was conducted on the basis of the following considerations:

- four combinations *size-length* were available to characterize the motor dimensions as shown in Table 10;
- three *speed-classes* were available to characterize the speed of the motors as shown in Table 11;
- two *gearbox-series* were available to characterize the maximum axial and radial forces the shaft can handle as shown in Table 12;
- multiple *gear-ratio* are available;
- two possible configurations of the shaft: smooth shaft or keyed shaft;
- possibility to include a holding brake. It is used to hold the motor shaft when no power is applied to the servo motor.
- two possible encoder systems: resolver or encoder EnDat 2.2

The possibility to include the brake and the keyed shaft were considered mandatory. The other options were analyzed and detailed discussed.

Figure 74 illustrates the speed-torque curves for two *speed-classes* available for the *size-length* 23 at 80VDC operation.

Table 10: *size-length* combinations for the B&R motors, 8LVB series.

Length	Available sizes		
	1	2	3
2	—	Yes	—
3	Yes	Yes	Yes

Table 11: *speed-class* combinations for the B&R motors, 8LVB series.

Size	Available nominal speeds n_N [rpm] at 80VDC operation		
	1500=*speed-class C*	2100=*speed-class D*	3000=*speed-class F*
1	Yes	—	Yes
2	Yes	—	Yes
3	Yes	Yes	—

The models with larger nominal speed does not have lower torques, thus, for all the combinations *size-length*, the fastest model was considered. High-speed motors allow to:

- increase the gear-ratio to reduce the required torque;

Table 12: *gearbox-series* combinations and available *gear-ratio* for the B&R motors, 8LVB series.

Gearbox-series	single stage	double stage
8GM40	3, 4, 5, 8, 10	9, 12, 15, 16, 20, 25, 32, 40, 64, 100
8GM50	3, 4, 5, 8, 10	9, 12, 15, 16, 20, 25, 32, 40, 64, 100

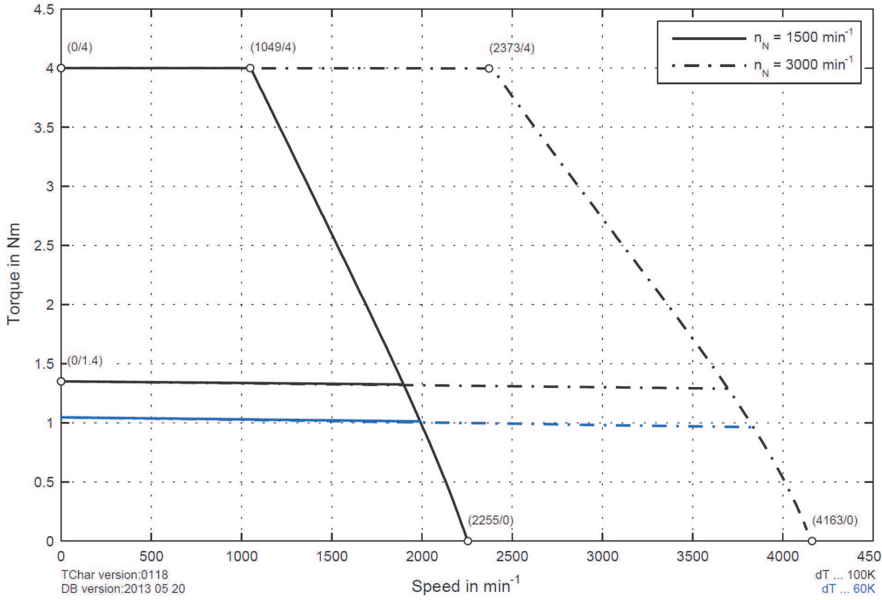

Figure 74: speed-torque curves for two *speed-classes* available for the *size-length* 23 at 80VDC operation.

- increase the operative range of speeds.

Among all the possible combinations, the following solution were considered:

- motors with *size-length* "13", with nominal speed $n_N = 3000$ rpm and nominal torque $M_n = 0.32$ Nm;
- motors with *size-length* "22", with nominal speed $n_N = 3000$ rpm and nominal torque $M_n = 0.65$ Nm;
- motors with *size-length* "23", with nominal speed $n_N = 3000$ rpm and nominal torque $M_n = 1.3$ Nm;
- motors with *size-length* "33", with nominal speed $n_N = 2100$ rpm and nominal torque $M_n = 2.45$ Nm;

The maximum value of the gear-ratio for the three *speed-classes* can be calculated as follows:

- for the motors with *speed-class* C, $k_{lim} = \frac{n_N}{\omega_{max}} = \frac{1500}{396} = 3.8$
- for the motors with *speed-class* D, $k_{lim} = \frac{n_N}{\omega_{max}} = \frac{2100}{396} = 5.3$

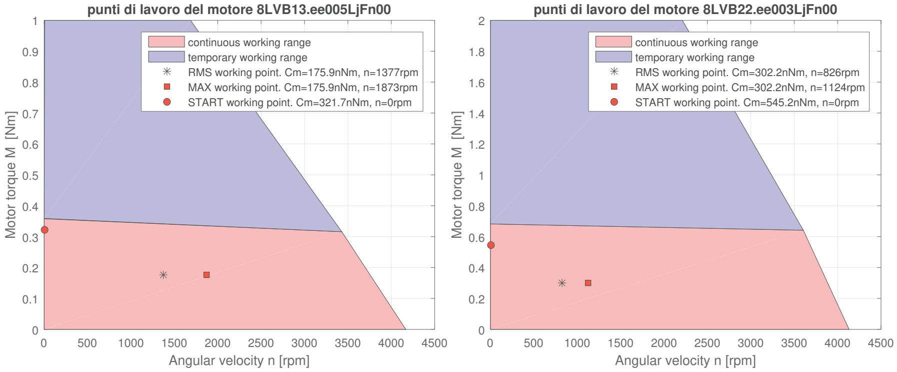

Figure 75: Working points for the motors 8LVB-13 with gear ratio $k = 5$ (a) and 8LVB-22 with gear ratio $k = 3$ (b).

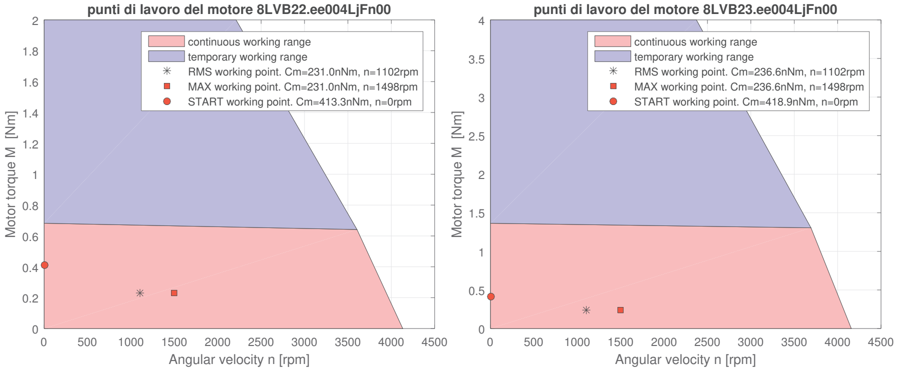

Figure 76: Working points for the motors 8LVB-22 with gear ratio $k = 4$ (a) and and 8LVB-23 with gear ratio $k = 4$ (b).

- for the motors with *speed-class* F, $k_{lim} = \frac{n_N}{\omega_{max}} = \frac{3000}{396} = 7.6$

Considering $k = 3, 4, 5, 8$, it was possible to calculate the maximum value of the torque (M_{max}) and the maximum value of the angular velocity (n_{max}) required by the motors:

- $n_{max} = 1188$ rpm and $M_{max} = 0.548\text{Nm}$, if $k = 3$;
- $n_{max} = 1584$ rpm and $M_{max} = 0.411\text{Nm}$, if $k = 4$;
- $n_{max} = 1980$ rpm and $M_{max} = 0.329\text{Nm}$, if $k = 5$;
- $n_{max} = 3168$ rpm and $M_{max} = 0.206\text{Nm}$, if $k = 8$;

Given the values obtained by the simulations (Table 10b), the *Principle of virtual works* was used to compute the torque and angular velocity required by the motors. Analyzing the results, some considerations can be derived:

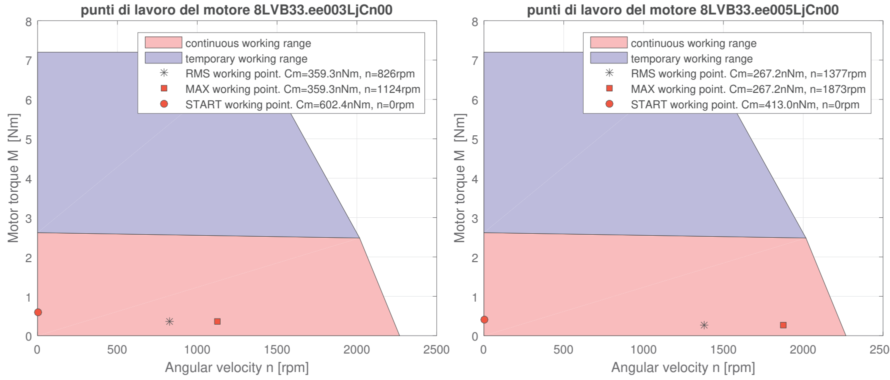

Figure 77: Working points for the motors 8LVB-33 with gear ratio $k = 3$ (a) and 8LVB-33 with gear ratio $k = 5$ (b).

- Motor configuration with *size-length* "13" allow a good operating range for the angular velocity but not for the torque as shown in Fig. 75a;
- Motor configuration with *size-length* "22" allow a large operating range for the angular velocity but not for the torque as shown in Fig. 75b and 76a;
- Motor configuration with *size-length* "23" allow a large operating range both for the angular velocity and the torque as shown in Fig. 76b;
- Motor configuration with *size-length* "33" allow a large operating range for torque and angular velocity but the gear-ratio can reduce the operating range for the angular velocity as shown comparing Fig. 77a and 77b

As a consequence, the motor configurations with *size-length* "13" and "22" were discarded because of the weak performance in terms of torque, whereas the motor configuration with *size-length* "33" was rejected for economical reasons. As a result, the final choice was a motor with *size-length* "23", *speed-class F* and gear-ratio $k = 4$; Table 16 lists the main parameters of the selected motor.

Finally, it is necessary to calculate the current and the voltage for the operating conditions using the following equations:

$$I_a = M/K_T \tag{123}$$

$$V_a - K_E n = R_a I_a - L_a \frac{I_a}{dt} \tag{124}$$

where I_a and V_a are the current and the voltage, respectively. In Table 14 the values of I_a and V_a calculated using (123,124) are compared with the nominal and maximum values reported in Table 16.

Table 13: Electromechanical parameters characterizing the gear-motor "8LVB23.ee004LjCn00", *size-length* "23", *speed-class F*, gearbox 8GM50 with $k = 4$.

Parameter	Value	Unit
Nominal speed n_N	3000	rpm
Number of pole pairs	4	
Nominal torque M_n	1.3	Nm
Nominal current I_n	5.8	A
Stall torque M_0	1.35	Nm
Stall current I_0	6	A
Maximum torque M_{max}	4	Nm
Maximum current I_{max}	20.7	A
Maximum speed n_{max}	6600	rpm
Torque constant K_T	0.23	Nm/A
Voltage constant K_E	13.61	$V/1000rpm$
Stator resistence R_a	0.83	Ω
Stator inductance L_a	2	mH
Moment of inertia of the motor J_m	0.26	$kg\ cm^2$
Moment of inertia of the brake J_{br}	0.12	$kg\ cm^2$
Number of gear stages	1	
Gear ratio k	4	
Moment of inertia of the gearbox J_g	0.06	$kg\ cm^2$
Efficiency at full load η	96	%

Table 14: Electrical parameters characterizing the gear-motor "8LVB23.ee004LjCn00"

	Value	Nominal value	Maximum value
Voltage V_a [V]	22.8	80	nd
Current I_a [A]	2.1	5.8	20.7

The calculation of the current and voltage required for the operating conditions allows the selection of the proper drive as shown in the next section.

5.6 DRIVE SELECTION

Drives were selected based on the maximum winding currents estimated for each motor. Specifically, each drive is capable of providing

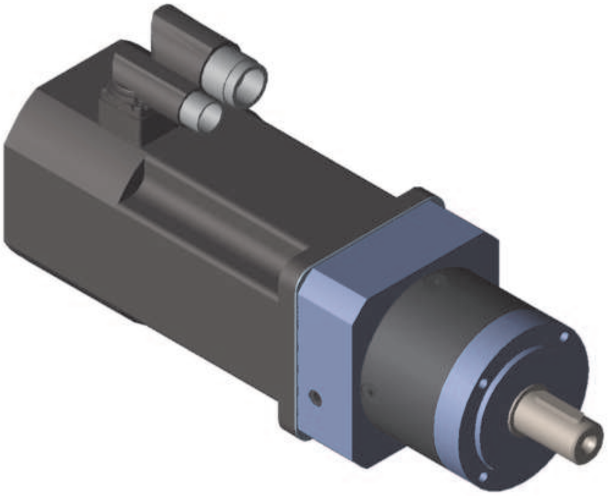

Figure 78: CAD model of the selected motor.

continuously the peak currents that characterize the corresponding motor.

The main characteristic that drove the selection of the drives was the compatibility with the EtherCAT fieldbus (as detailed described in Sec. 5.10). Four drives Beckhoff Ax5206 were chosen to drive the eight brushless motors. The Ax5206 is a 2-channel Servo Drive that enables the control of two motors with identical or even with different power, up to a total current of 12 A. The main features of these drives are outlined in Fig. 79 and Table 15. The estimated peak current required for a linear movement of the end-effector is rather lower than the maximum peak current that the driver can provide.

Table 15: Technical data of Beeckhoff Ax5206 2-channel servo drive

Technical data	Ax5206	Unit
Rated output current at 50 °C	2×6	A
Peak output current	2×13	A
Max breaking power	14	kW
System bus	EtherCAT	
Weight	6.0	kg
Height without connectors	274	mm
Width	92	mm
Depth without connectors	232	mm

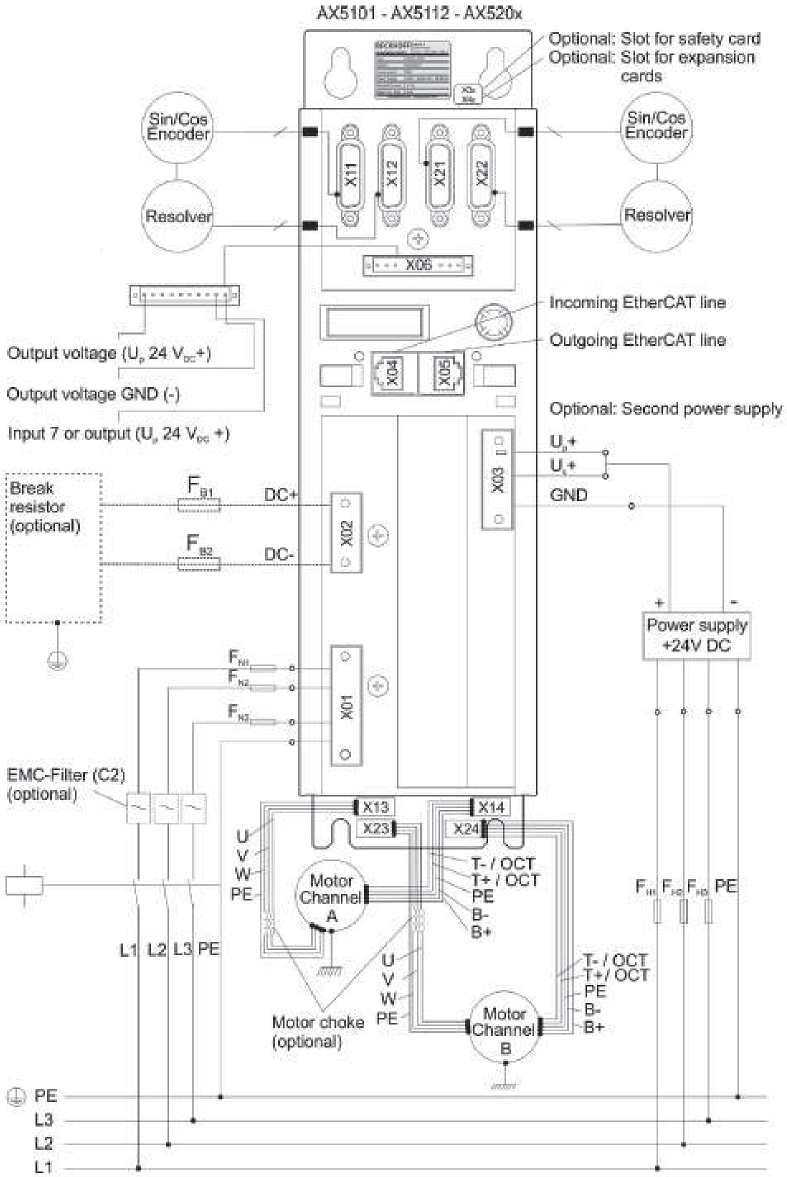

Figure 79: Beckhoff Ax5206 2-channel servo drive with electrical connection scheme.

5.7 PULLEY DESIGN

The pulley block was designed to be reconfigurable which means that it can be quickly repositioned inside the workcell. The system was designed to redirect the cable coming from the winch and follow the position of the end-effector as shown in Fig. 80.

The pulley block is composed by a main frame which is obtained by milling from a block of aluminum. The frame has a central hole on which is housed a bearing (SKF 6001-2Z). The bearing is fixed using a retaining ring for holes (UNI 7437). Then, a pin is positioned within the bearing, which is fixed by a screw *M4* to the housing containing

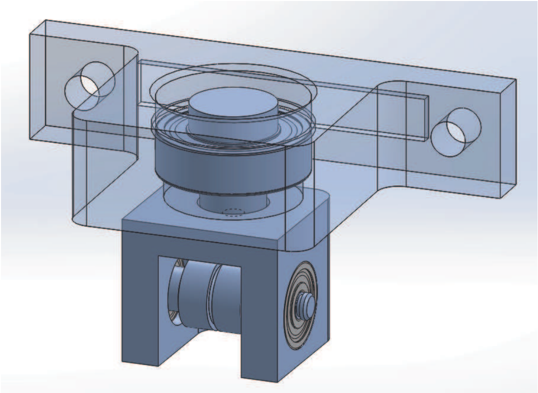

Figure 80: CAD model of the pulley block.

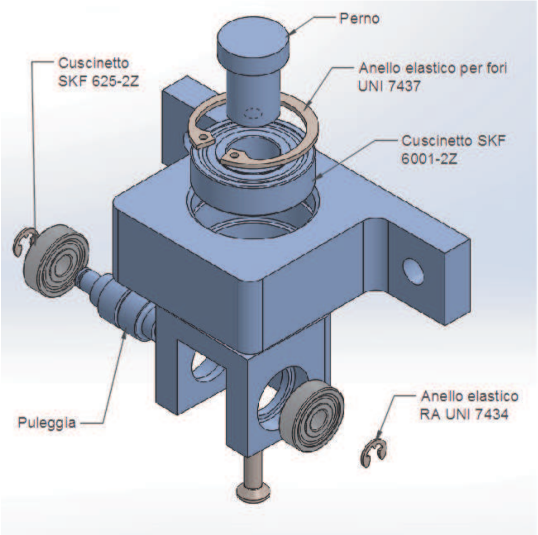

Figure 81: Exploded view of the pulley block.

the bearings (SKF 625-2Z), and it allows the rotation of the cable guide pulley. Two retaining rings for shafts (UNI 7434) are finally placed to avoid axial displacements. Figure 81 illustrates the details of the assembled system.

5.7.1 *Bearings selection*

In the market there are many types of bearings; radial ball bearings, thrust bearings, spherical roller bearings, thrust bearings and needle roller bearings of many other types. The first step to make to select the most suitable bearings for the application is to identify the most suitable type for the applied loads. The main requirements are:

- available space
- loads
- displacements

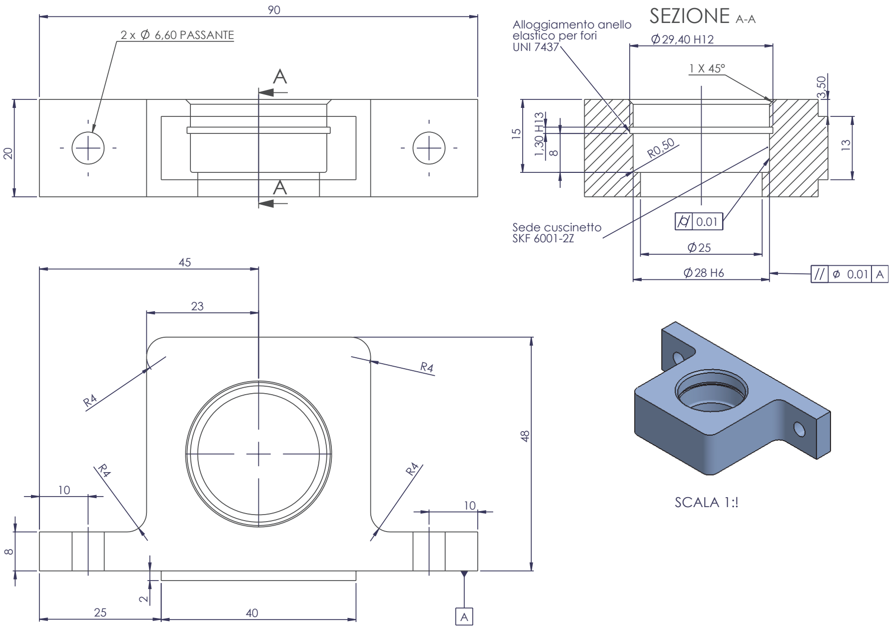

Figure 82: Technical draw of the main frame

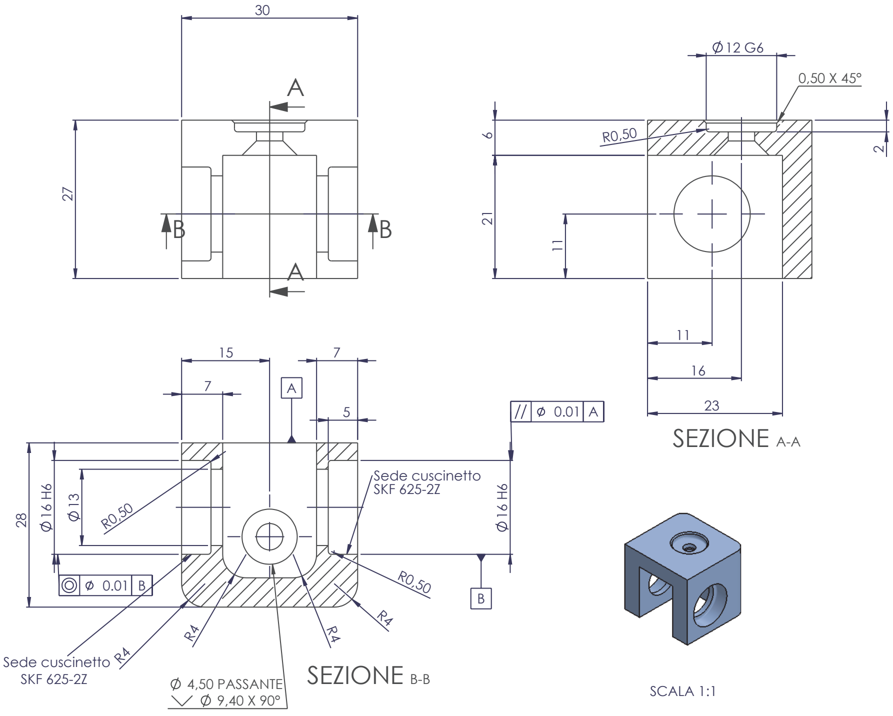

Figure 83: Technical draw of the main frame

- precision
- velocity
- noisiness
- stiffness

- axial displacements
- assembling

To make a proper bearing selection, the loads acting on it must be considered. A bearing is typically selected on the basis of its load rating relative to the applied loads and the requirements regarding bearing life and reliability [116]. Values for the basic dynamic load rating C and the basic static load rating C_0 are listed in the product tables. Both dynamic and static bearing load conditions should be independently verified and should include any heavy, short duration shock loads that may occur on rare occasions.

The basic dynamic load rating C is used for life calculations involving dynamically stressed bearings, i.e. bearings that rotate under load. It expresses the bearing load that will result in an ISO 281:2007 basic rating life of 1 000 000 revolutions. It is assumed that the load is constant in magnitude and direction and is radial for radial bearings and axial, acting centrically, for thrust bearings.

Verification of static bearing loads is performed by checking the static safety factor of the application, which is defined as

$$s_O = \frac{C_O}{P_0} \tag{125}$$

where s_0 indicates the static safety factor, C_0 indicates the basic static load rating (known by the technical documentation of the bearing) and P_0 indicates the equivalent static bearing load. The static safety factor s_0 must be lower than 2 for ball bearings with steel balls. The maximum load that can occur on a bearing should be used when calculating the equivalent static bearing load.

The basic static load rating C_0 as defined in ISO 76:2006 corresponds to a calculated contact stress at the center of the most heavily loaded rolling element/raceway contact. This stress produces a total permanent deformation of the rolling element and raceway, which is approximately 0.0001 of the rolling element diameter. The loads are purely radial for radial bearings and axial, centrically acting for thrust bearings. Values for basic static load rating C_0 are listed in the product tables

To compare actual loads with the basic static load rating, the actual loads must be converted into an equivalent load. The equivalent static bearing load P_0 is defined as that hypothetical load (radial for radial bearings and axial for thrust bearings) which, if applied, would cause the same maximum rolling element load in the bearing as the actual loads to which the bearing is subjected.

The equivalent static bearing load P_0 can be calculated as follows:

$$P_0 = X_0 F_r + Y_0 F_a \tag{126}$$

where F_r is the radial load whereas F_a is the axial load as shown in Fig. 84. X_0 and Y_0 are radial load factor and the axial load factor, respectively, and they can be found in the product documentation.

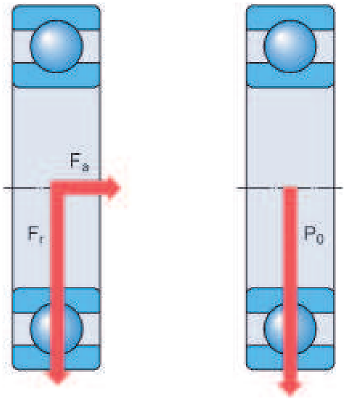

Figure 84: Loads applied to the bearing.

The basic rating life of a bearing according to ISO 281:2007 is:

$$L_{10} = (\frac{C}{P})^T \tag{127}$$

where L_{10} is the basic rating life (at 90% reliability in millions of revolutions), C is the basic dynamic load rating (in kN), P is the equivalent dynamic bearing load (in kN) and $T = 3$ for ball bearings.

A ball bearing SKF 6001-2Z was chosen to allow a rotation between the main frame and the housing containing the bearings that allow the rotation of the cable guide pulley. A maximum cable tension of 100 N was considered which was related to a maximum axial load of 200 N (100 N towards the end-effector + 100 N towards the winch). Only static load rating was performed since the angular velocity of the bearing was lower than 10 rpm.

The bearings for the pulley shaft must present reduced dimensions, withstand a dynamic load in the radial direction of 100N and rotate at high speed. SKF 625-2Z ball bearings were chosen because they are able to effectively withstand the radial load exerted by the cables and, at the same time, rotate at high speed. Dynamic loads calculations verified a standard duration of 10^6 cycles.

Shielded bearings were chosen in both cases since the shielding allows to increase their reliability and durability.

5.7.2 *structural analysis*

The pulley supported by the ball bearings SKF 625-2Z can be modeled as shown in Fig. 86. The material employed for the realization of the component is the aluminum alloy AA7075-T6 having yield stress $\sigma_{p,0.2} = 500$ MPa and fatigue limit $\sigma_{A,R=-1} = 170$ MPa. The shaft is

Table 16

Parameter	SKF 6001-2Z	SKF 625-2Z	Unit
d	12	5	mm
D	28	16	mm
B	8	5	mm
d_1	17	8.4	mm
D_2	24.7	13.2	mm
$r_{1,2}$ min	0.3	0.3	mm
d_a min	14	7.4	mm
d_a max	16.9	8.3	mm
D_a max	26	13.6	mm
r_a max	0.3	0.3	mm
Dynamic basic load rating C	5.4	1.1	kN
Static basic load rating C_0	2.3	0.38	kN
Fatigue load limit P_u	0.1	0.01	kN
Reference speed	60000	104000	rpm
Limiting speed	60000	55000	rpm

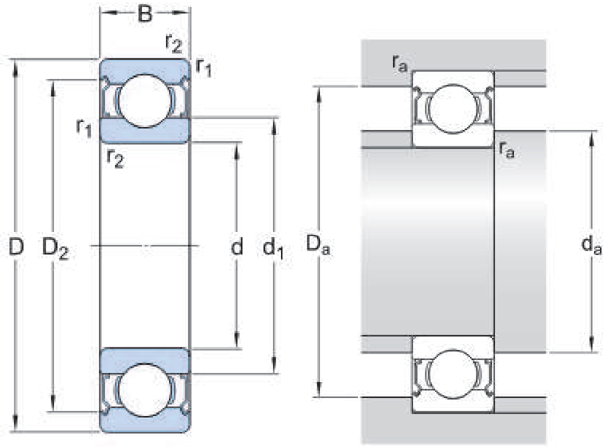

Figure 85: technical drawing of SKF 6001-2Z and SKF 625-2Z

subjected to a force T of 160 N. Figure 87 reports the shaft dimensions and the maximum stress in section A is given by:

$$\sigma_{max,A} = \frac{32M_f}{\pi d^3} = \frac{3216013.5}{\pi 8^3} = 42MPa \tag{128}$$

The static safety factor is:

$$\upsilon_s = \frac{\sigma_{p,0.2}}{\sigma_{max,A}} = \frac{500}{42} = 11.9 \tag{129}$$

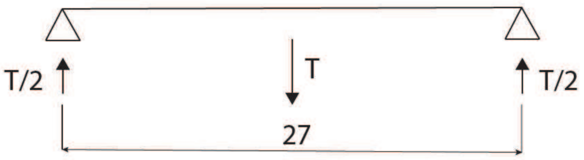

Figure 86: Schematizzazione dell'albero del passacavo

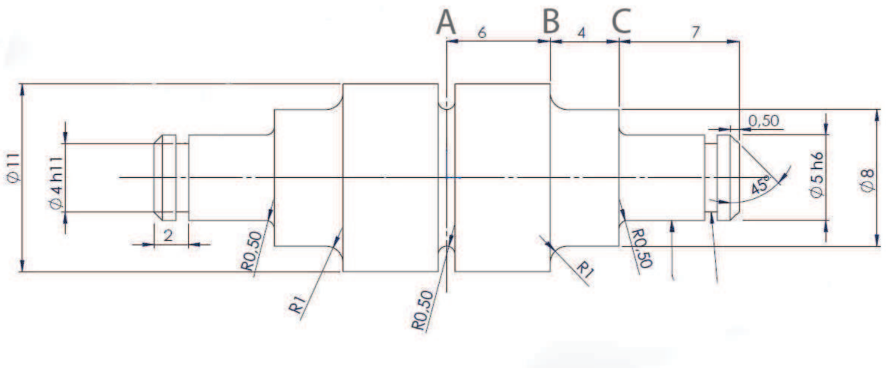

Figure 87: Albero del passacavo con quote

Basic fatigue stress analysis calculations were performed for sections A, B and C as described in [117].

The maximum stress in section A is:

$$\sigma_{f,A} = \frac{32M_f}{\pi d^3} = \frac{3216013.5}{\pi 8^3} = 42MPa \tag{130}$$

The maximum fatigue stress for section A can be computed as follows:

$$\sigma_A^* = \frac{\sigma_A}{K_f K_d K_l} = 64Mpa \tag{131}$$

where:

- $\sigma_A = \sigma_{A,R=-1} = 170$ MPa.
- $K_f = 1 + q(K_t - 1) = 1.78$ is the fatigue notch factor and it was computed considering $K_t = 2.2$ and $q = \frac{1}{(1+\frac{a}{r})} = \frac{1}{(1+\frac{0.265}{0.5})} = 0.65$;
- $k_d = 1$ is the size factor;

- $k_l = 1.5$ is the surface finishing factor.

The values of K_t, a and k_l were determined using the technical documentation found in [117]. The fatigue stress concentration factor can be computed as follows:

$$\nu_f = \frac{\sigma_A^*}{\sigma_{f,A}} = \frac{64}{42} = 1.51 \tag{132}$$

Therefore, section A is verified.

Similarly, the maximum stress in section B is:

$$\sigma_{f,B} = \frac{32M_f}{\pi d^3} = \frac{321607.5}{\pi 8^3} = 24MPa \tag{133}$$

and the maximum fatigue stress for section B can be computed as follows:

$$\sigma_A^* = \frac{\sigma_A}{K_f K_d K_l} = 70.9Mpa \tag{134}$$

where:

- $\sigma_A = \sigma_{A,R=-1} = 170$ MPa.
- $K_f = 1 + q(K_t - 1) = 1.55$ is the fatigue notch factor and it was computed considering $K_t = 2.2$ and $q = \frac{1}{(1+\frac{a}{r})} = \frac{1}{(1+\frac{0.265}{1})} = 0.79$;
- $k_d = 1$ is the size factor;
- $k_l = 1.5$ is the surface finishing factor.

The values of K_t, a and k_l were determined using the technical documentation found in [117]. The fatigue stress concentration factor can be computed as follows:

$$\nu_f = \frac{\sigma_A^*}{\sigma_{f,B}} = \frac{70.9}{24} = 2.59 \tag{135}$$

Therefore, section B is verified.

Finally, the maximum stress in section C is:

$$\sigma_{f,C} = \frac{32M_f}{\pi d^3} = \frac{321607.5}{\pi 5^3} = 45MPa \tag{136}$$

and the maximum fatigue stress for section B can be computed as follows:

$$\sigma_A^* = \frac{\sigma_A}{K_f K_d K_l} = 75.5Mpa \tag{137}$$

where:

- $\sigma_A = \sigma_{A,R=-1} = 170$ MPa.

- $K_f = 1 + q(K_t - 1) = 1.52$ is the fatigue notch factor and it was computed considering $K_t = 2.2$ and $q = \frac{1}{(1+\frac{a}{r})} = \frac{1}{(1+\frac{0.265}{0.5})} = 0.65$;
- $k_d = 1$ is the size factor;
- $k_l = 1.5$ is the surface finishing factor.

The values of K_t, a and k_l were determined using the technical documentation found in [117]. The fatigue stress concentration factor can be computed as follows:

$$\upsilon_f = \frac{\sigma_A^*}{\sigma_{f,C}} = \frac{75.5}{45} = 1.67 \tag{138}$$

Therefore, section C is verified.

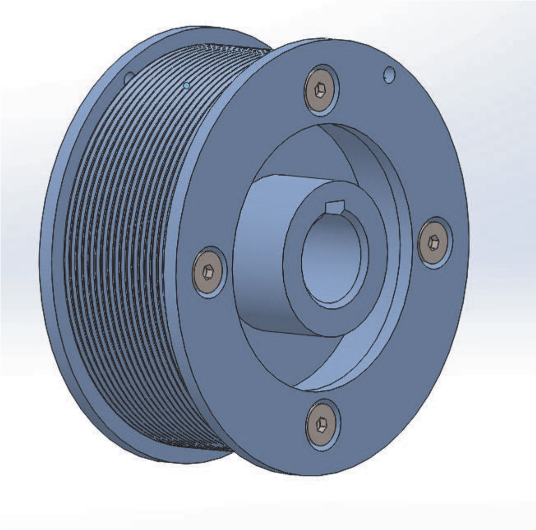

Figure 88

5.8 WINCH DESIGN

The design of the winch was based on the following considerations:

- Motor shaft with diameter: $\oslash = 16$ mm;
- Maximum axial length: 34 mm;
- Key size dimension: $5 \times 4 \times 28$ mm;
- maximum diameter: 72 mm;
- trapezoidal thread;
- Number of revolutions: 18;
- Maximum length of a wrapped cable: 3900 mm;

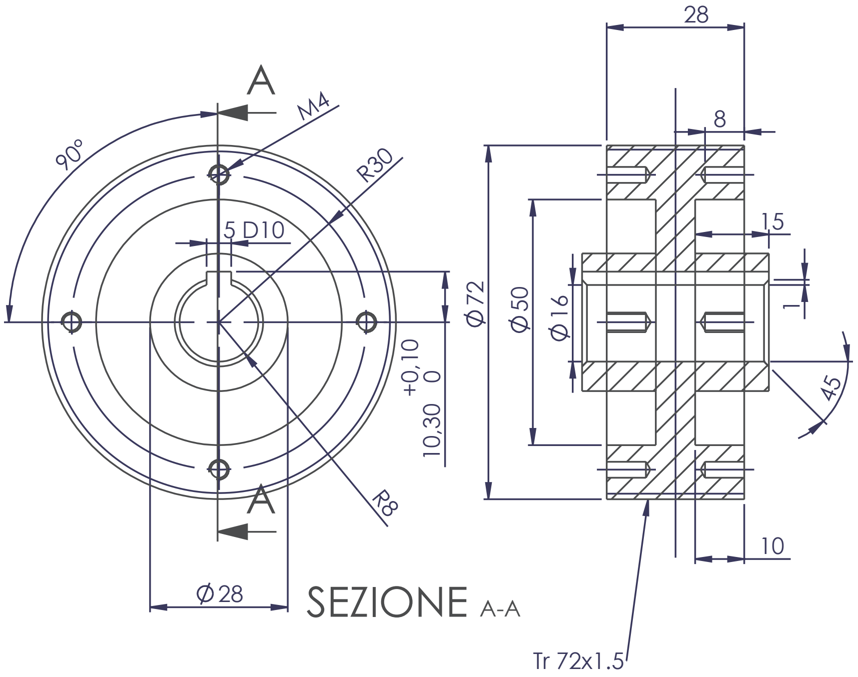

Figure 89

- Cable diameter: $\oslash \leqslant 1\ \mathrm{mm}$

A prototype of winch was built to test the cable wrapping. As a result, a final thread with pitch of $1.5\ \mathrm{mm}$ and depth of $1\ \mathrm{mm}$ was chosen as shown in Fig. 89. Figure **??** shows the final assembly with motors and pulleys.

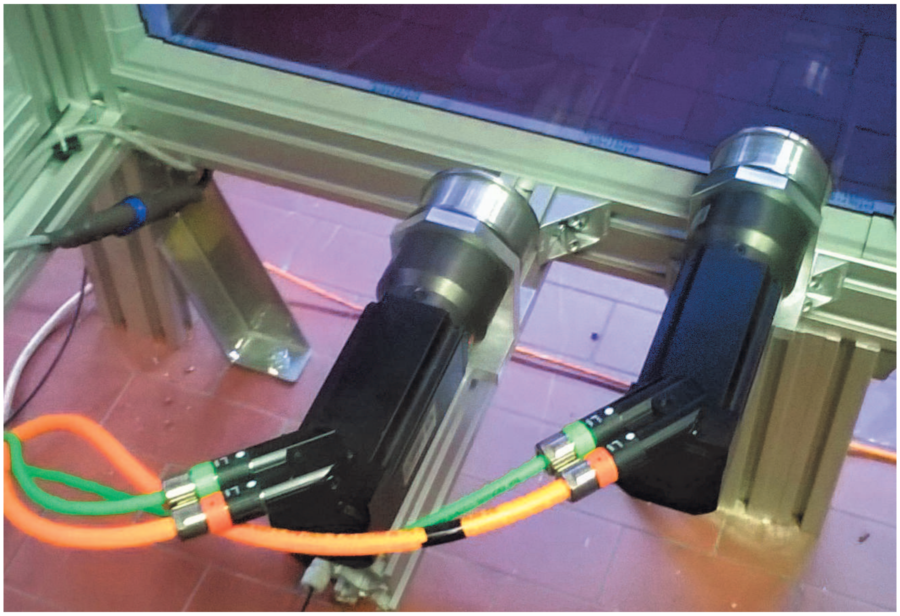

Figure 90: Motors and pulleys.

The end-effector can be modeled as described in Sec. 3.5. Figure 91 reports the free body diagram of the system that is characterized by two rigid bodies: the main supporting structure, here defined as *Body 1*, and the translating platform, here defined as *Body 2*. The upper cables are connected to the main structure of the end-effector; the lower cables are connected to the translating platform, which can slide along a linear axis through a prismatic joint.

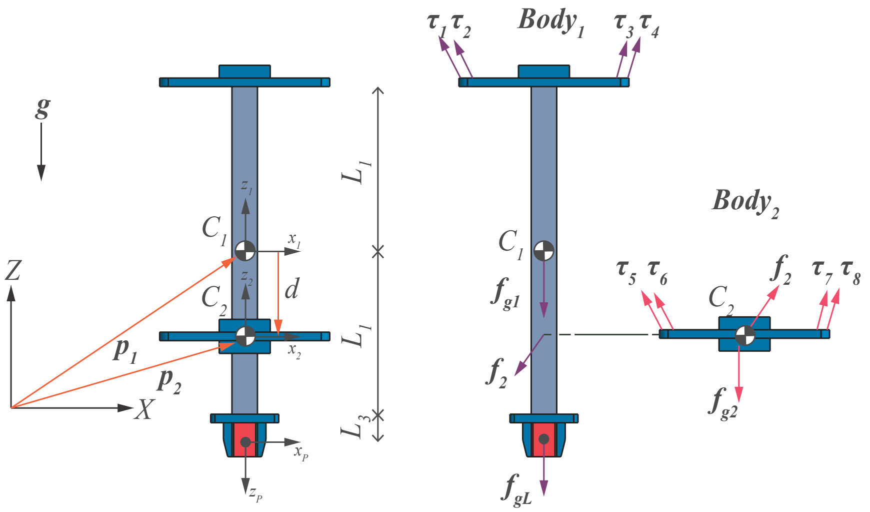

Figure 91: Free-body diagram of the end-effector.

The aim of this section is the detailed design of the reconfigurable end-effector based on the following requirements:

- Low mass of the system;
- Low cost;
- Large stroke (greater than $300\mathrm{mm}$);
- Capability of handle large payloads compared to the total mass of the end-effector;
- Controllable;
- Symmetric design.

Some solutions were considered and analyzed. The simplest solution to vary the distance of the cables is to use a pneumatic piston with rail guides. This solution is cheap and reliable but a continuous control of *Body 2* is not possible. A class of actuators that allows a continuous control of the movement consists in the electro-mechanical linear actuators that typically operate by conversion of rotary motion into linear motion. Three types of mechanisms can be found [118, 119]:

- Screw-type mechanisms. The screw shaft moves by rotating the actuator's nut;
- Wheel and axle mechanisms. A rotating wheel moves a cable, rack, chain or belt to produce linear motion;
- Cam mechanisms. A cam is a mechanical component capable of transmitting motion to a follower by direct contact and produce a linear movement. The stroke is typically small and not suitable for the purpose.

Several models that exploit this principle are available in the market but they have two main drawbacks: low stroke/mass ratio and lack of symmetry. Symmetry is needed to simplify the mechanical model of the end-effector and its control.

As a result, three non-commercial solutions were developed: a ball screw mechanism, a rack and pinion mechanism and a belt-driven mechanism. All the solutions were conceived with one or two linear guides and a mobile platform where the lower cables were anchored. The solution with the ball screw transmission was selected because of the highest stroke/mass ratio and the possibility to design a symmetric solution as shown in Fig. 92. Furthermore, ball screws are able to apply high thrust loads with minimum internal friction.

The model of the reconfigurable end-effector consist of three main platforms: a motor platform, a translating platform and a tool platform. The motor is fixed to the motor platform which is connected to the tool platform by means of two cylindrical shafts. The cylindrical shafts create a linear low-friction guideway where the translating platform slides. The translating platform is driven by a ball screw actuator. The mechanism is shown in Fig. 92 To select the most suitable ball screw actuator, one must consider the following key-points:

- Dynamic axial load capacity
- Static axial load capacity
- Radial loads
- Stiffness
- Axial tip load PB
- Critical speed
- Speed limit

The next section aims at computing the dynamic loads required for a pick and place movement with the on-line reconfiguration of the end-effector.

5.9.1 *Simulation of a pick and place movement with on-line reconfiguration*

The kinematic model presented in Sec. 3.4 was used to define the pose of the end-effector with respect to the base frame. Table 17 reports the layout of the robot as well as the inertial parameters of the end-effector. A pick and place movement was tested to calculate the linear actuator requirements in terms of torque ($C_{m,max}$, $C_{m,rms}$), angular velocity ($\dot{\theta}_{max}$, $\dot{\theta}_{rms}$) and angular acceleration ($\ddot{\theta}_{max}$, $\ddot{\theta}_{rms}$) to perform the desired trajectory of *Body 1* and *Body 2*. The reconfiguration of the lower cable is performed during the depart and approach movements and it is expressed by the relative distance d. It is important to point out that the linear actuator requirements are strictly correlated to the tensions exerted by the cables as discussed in Sec. 3.4. Table 18 reports the trajectory parameters that characterize a pick and place movement whereas Fig. 93 illustrates the pick and place path of the tool center point. Figure 94 illustrates position, velocity and acceleration of *Body 1* whereas Fig. 95 reports position, velocity and acceleration of *Body 2*. The trajectories were obtained using a V-order polynomial acceleration profile.

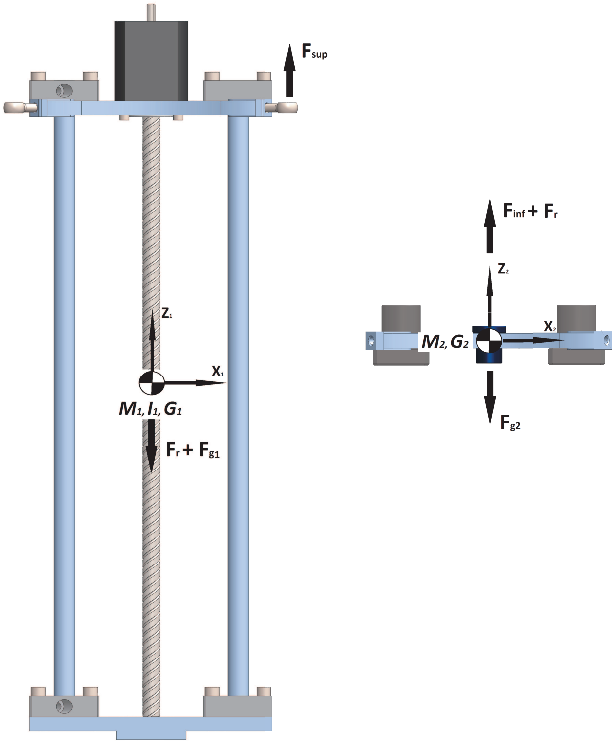

Figure 92: Prototype of the end-effector with forces

Using the ID algorithms implemented in the simulator, the pick and place movement was tested with the purpose of computing the linear force (F_r), the linear velocity ($\dot{d}$) and the linear acceleration

Table 17: (a) Cable exit points A_i and cable anchor points B_i. (b) Kinematic and inertial parameters of the reconfigurable end-effector.

Parameter	Value [m]
${}^{O}A_1, {}^{O}A_5$	$(0, 0.5, 2.21)$
${}^{O}A_2, {}^{O}A_6$	$(1.815, 0.5, 2.21)$
${}^{O}A_3, {}^{O}A_7$	$(1.815, 2.87, 2.21)$
${}^{O}A_4, {}^{O}A_8$	$(0, 2.87, 2.21)$
${}^{C_1}B_1$	$(d_x, -d_y, L_1)$
${}^{C_1}B_2$	(d_x, d_y, L_1)
${}^{C_1}B_3$	$(-d_x, d_y, L_1)$
${}^{C_1}B_4$	$(-d_x, -d_y, L_1)$
${}^{C_1}B_5$	$(-d_x, d_y, d)$
${}^{C_1}B_6$	$(-d_x, -d_y, d)$
${}^{C_1}B_7$	$(d_x, -d_y, d)$
${}^{C_1}B_8$	(d_x, d_y, d)

(a)

Parameter	Value	Unit
m_1	2	kg
m_2	0.5	kg
$I_{1_{xx}}$	0.050	kgm^2
$I_{1_{yy}}$	0.050	kgm^2
$I_{1_{zz}}$	0.005	kgm^2
$I_{1_{xy}}, I_{1_{xz}}, I_{1_{yz}}$	0	kgm^2
$I_{2_{xx}}$	0.00093	kgm^2
$I_{2_{yy}}$	0.00037	kgm^2
$I_{2_{zz}}$	0.00130]	kgm^2
$I_{2_{xy}}, I_{2_{xz}}, I_{2_{yz}}$	0	kgm^2
d_x	0.055	m
d_y	0.0775	m
L_1	0.16	m
L_3	0.04	m

(b)

Table 18: Trajectory parameters for the movement task.

Parameter	Value	Unit
${}^{O}P_{in}$	$(0.9, 1, 0.8)$	m
${}^{O}P_{d}$	$(0.9, 1, 1.3)$	m
${}^{O}P_{a}$	$(0.9, 2.36, 1.3)$	m
${}^{O}P_{fin}$	$(0.9, 2.36, 0.8)$	m
α	0	deg
β	0	deg
γ	0	deg
T_{dep}	1.0	s
T_{trans}	1.0	s
T_{app}	1.0	s

($\ddot{d}$) required to move the translating platform. Two simulations were performed:

- A pick and place movement without carried load;

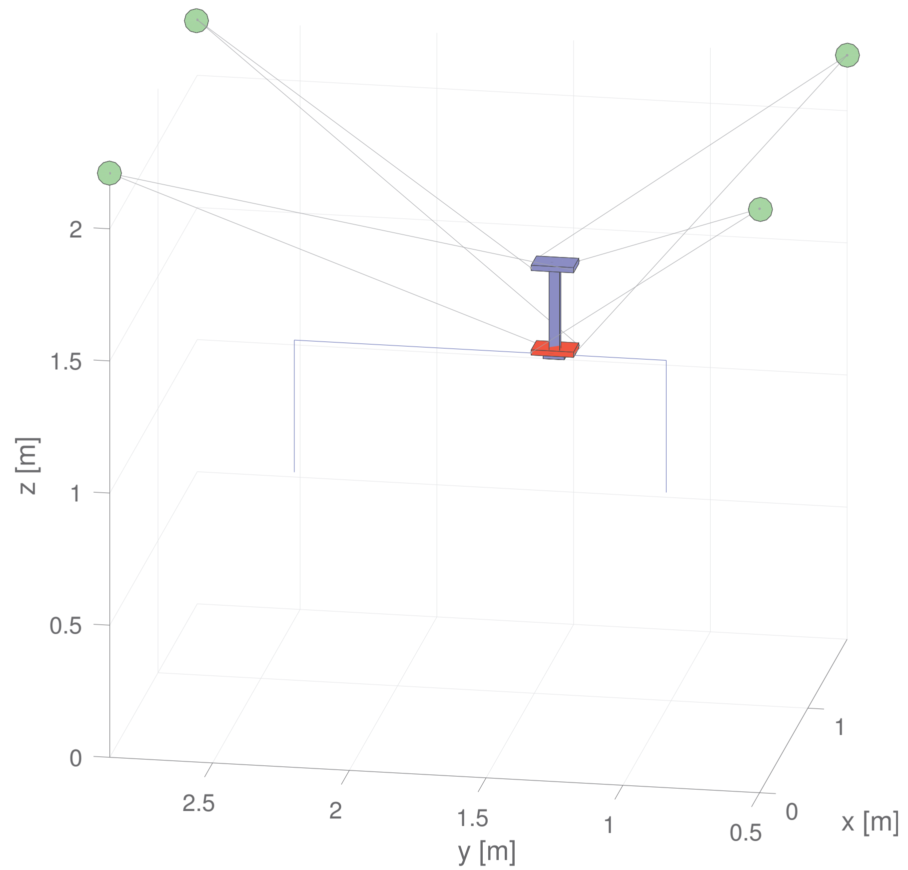

Figure 93: Reference path for the tool center point of the end-effector.

- A pick and place movement with 1 kg load located at the tool center point;

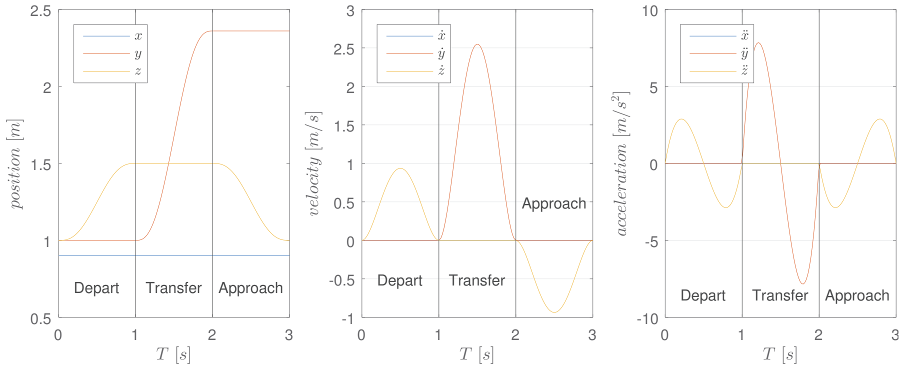

Figure 94: Planned trajectory of *Body 1* for the pick and place movement.

The results of the dynamic simulations of the movements are shown in Fig. 96 and 97 where the forces and the moments required to obtained the desired trajectory of the reconfigurable end-effector are displayed. Forces and moments are generated by

- the tensions exerted by the cables;

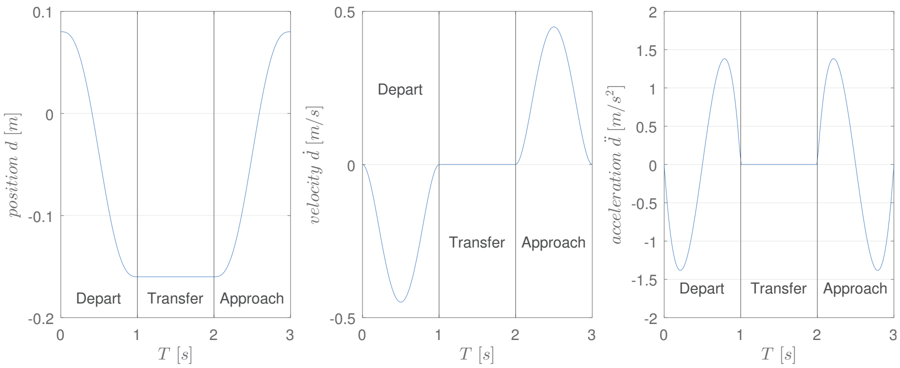

Figure 95: Planned trajectory of *Body 2* respect to *Body 1* for the pick and place movement.

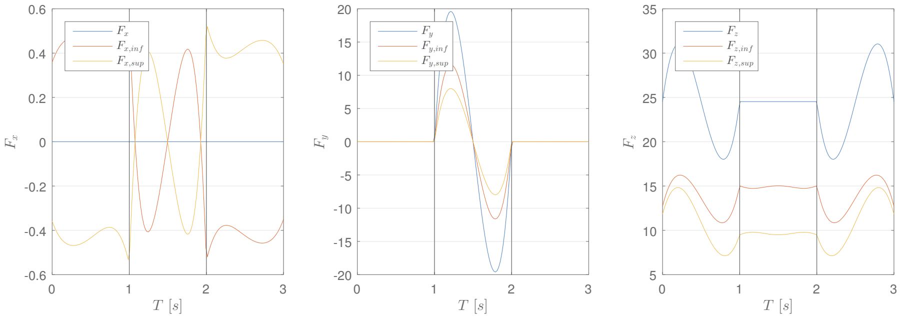

Figure 96: Equilibrium of the forces for the pick and place movement without carried load. The forces applied by the upper cables and the lower cables are displayed.

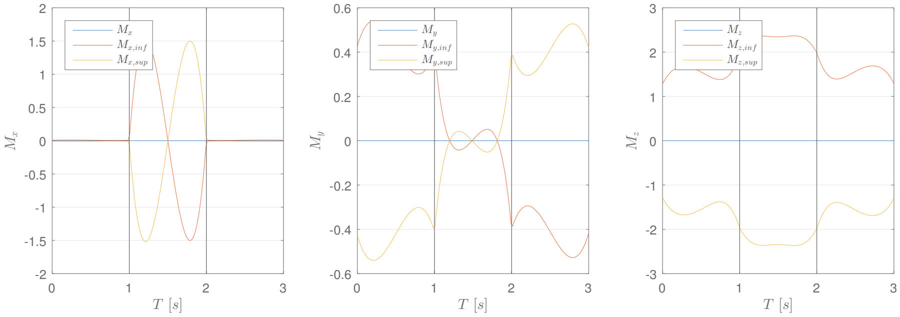

Figure 97: Equilibrium of the moments for the pick and place movement without carried load. The moments applied by the upper cables and the lower cables are displayed

- the force exerted by the linear actuator.

The equilibrium of *Body 2* is expressed by Eq. 53 (Fig. 98) and it allows to characterize the requirements in terms of torque (C_m) and angular

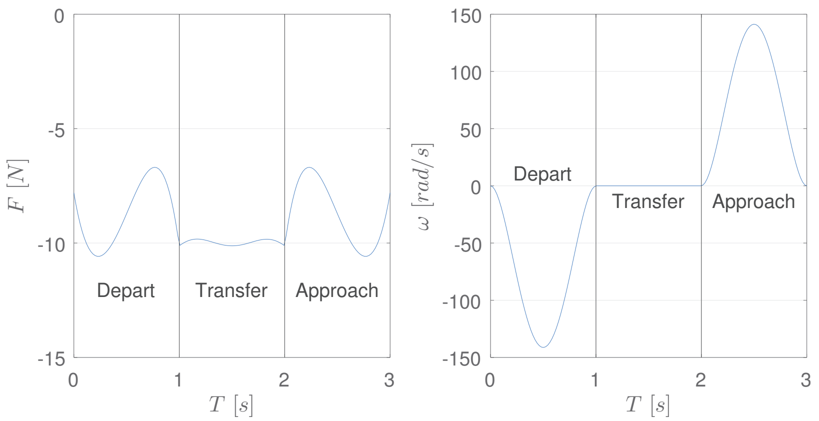

Figure 98: Linear force required for the pick and place movement without carried load.

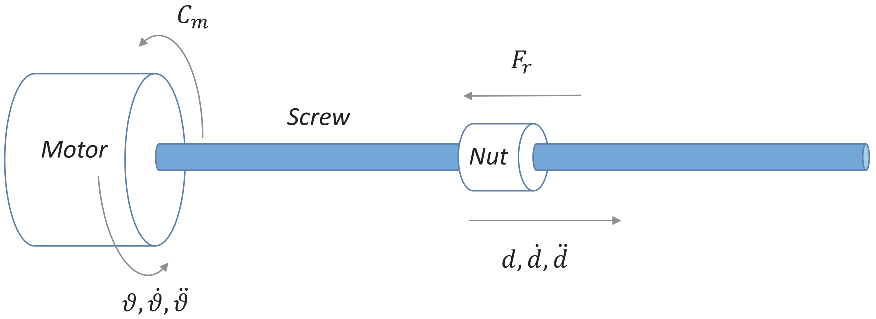

Figure 99: Transmission model for a screw ball actuator.

velocity ($\dot{\theta}$) for the motor that drives the screw using the *Principle of virtual work* (Fig. 99):

$$C_m = (I_m + I_v)\ddot{\theta} + \frac{F_r n}{\eta} \tag{139}$$

$$= (I_m + I_v)\frac{\ddot{d}}{n} + \frac{F_r n}{\eta} \tag{140}$$

if $n = \text{cost}\,|_{\theta}$:

$$n = \frac{\dot{d}}{\dot{\theta}} = \frac{\ddot{d}}{\ddot{\theta}} = \frac{P_v}{2\pi} \tag{141}$$

where the screw lead is $P_v = 20\ mm$, the mechanical efficiency is approximated at $\eta = 0.7$ and the rotor inertia is $I_m + I_v = 95\ gcm^2$.

Since the angular velocity $\omega = \dot{\theta}$ of the motor is not a major concern and the amount of torque required is not demanding, the simplest solution is represented by a stepper motor. In fact, while servo motors are excellent in applications requiring speeds greater than 3000 rpm and for high torque at high speeds or requiring high dynamic response. Steppers are excellent at speeds less than 3000 RPM and for low to medium acceleration rates and for high holding torque. Fur-

Table 19: Results of the inverse dynamics for the pick and place with on-line reconfiguration of the end-effector.

Parameter	Max value	RMS value	Unit
C_m (no load)	0.0378	0.0318	Nm
C_m (1 kg load)	0.0505	0.0497	Nm
$\dot{d}$	0.45	0.23	m/s
$\ddot{d}$	1.38	0.81	m/s^2
ω	1350	690	rpm
$\dot{\omega}$	4148	2422	rpm/s

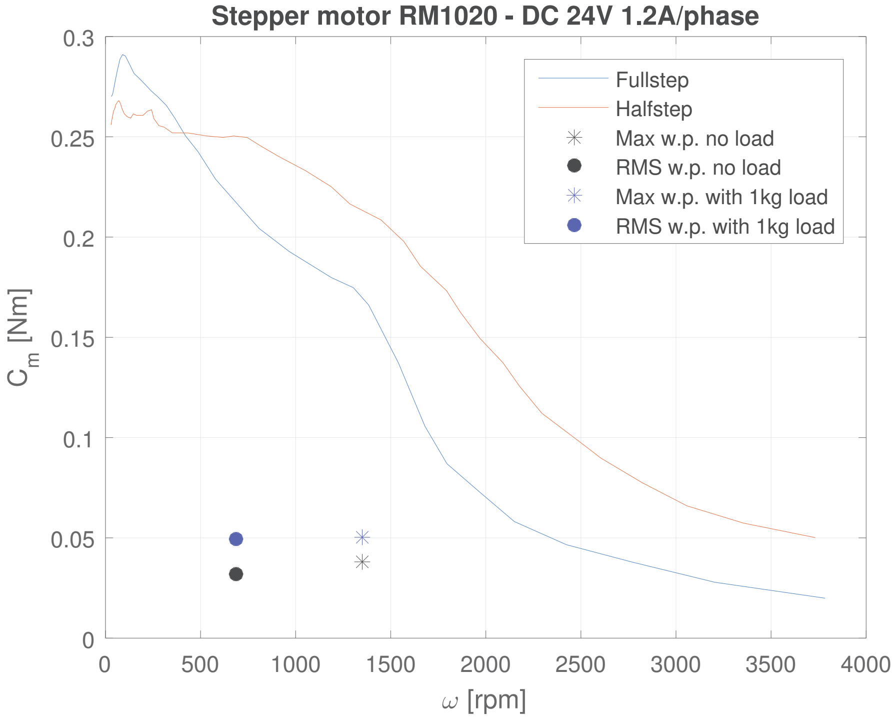

Figure 100: Working points for the stepper motor.

thermore, stepper control systems are less expensive and they can be controlled in open loop without the feedback provided by an encoder.

A stepper motor KSS ReMoBo 1020B-300 was available among the actuators owned by the research group and it was tested to check if the maximum working point ($C_{m,max}$, $\dot{\theta}_{rms}$) and the continuous working point ($C_{m,rms}$, $\dot{\theta}_{max}$), were inside the temporary working range and the continuous working range, respectively. Figure 100 illustrates the working points whereas Table 20 and Fig. 101 report the main parameters of the linear actuator.

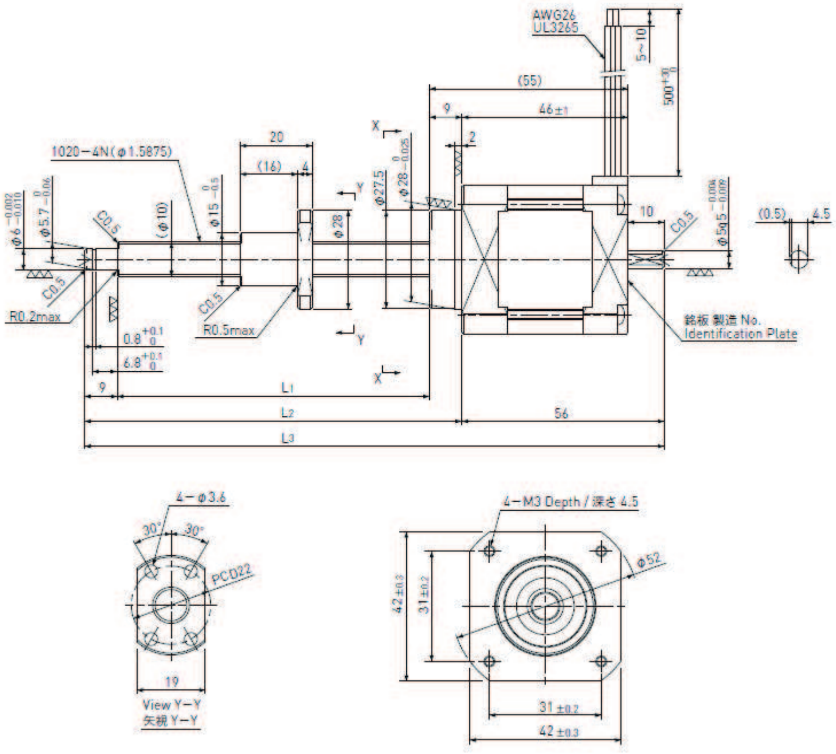

Figure 101: Technical drawing of the linear actuator KSS ReMoBo 1020B-300

Table 20: Datasheet of the linear actuator KSS ReMoBo 1020B-300

Parameter	Value	Unit
Stroke	0.320	m
Lead	0.02	m
Weight	0.570	kg
Step angle	1.8	deg
Axial play	0.1	mm
Rated voltage	4.0	V/Phase
Travel per pulse (full step)	0.01	mm
Reference thrust	50	N
Rated current	1.2	A/Phase
Winding resistance	1.2	Ω/Phase
Inductance	3	mH/Phase
Holding torque	0.32	N/m
Shaft material	SUS304	
Nut material	MRH polyamide type	
Driving method	2-phase Uni-polar	

5.9.2 *Design details*

The reconfigurable end-effector is composed by three aluminum alloy (AA7075-T6) platforms connected by two low-friction aluminum shafts IGUS AWM-12 as shown in Fig. 102. The translating platform is connected to two flange housings IGUS FJUM-12 that can slide along the low-friction shafts. The linear movement of the translating platform is obtained by means of ball screw shaft which is driven by the stepper motor.

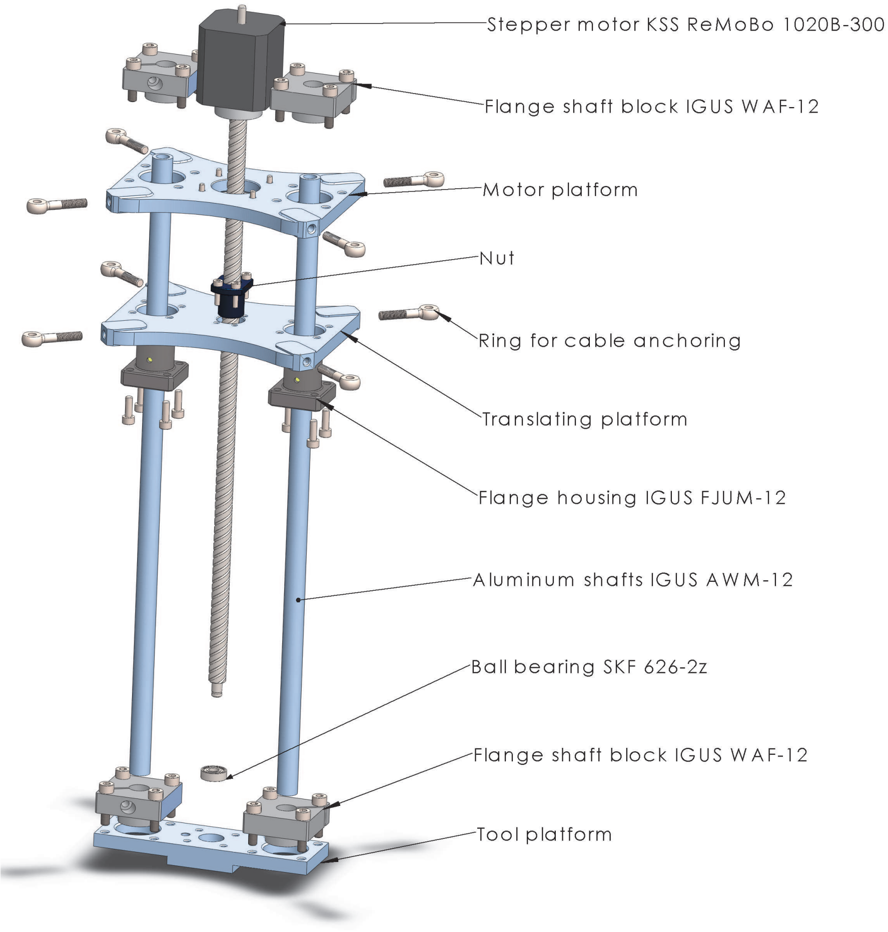

Figure 102: CAD model of the reconfigurable end-effector

The shafts are connected to the motor platform and the tool platform through four flange shaft blocks IGUS WAF-12. The shafts are hollow to allow the passage of cables from the motor platform to the gripper without interfering with the mobile platform. Eight rings are positioned at the vertices of the motor platform and the translating platform to anchor the cables.

Figures 103a, 103b and 104 illustrate the details of the motor platform, the translating platform and the tool platform, respectively. The platforms were designed with an optimal shape that allows to reduce the mass without affecting the stiffness.

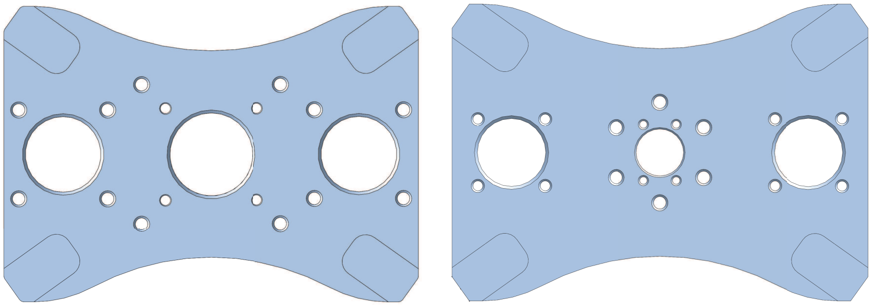

Figure 103: (a) Motor platform where the stepper motor KSS ReMoBo 1020B-300 is fixed. (b) Translating platform where the nut and the flange housings IGUS FJUM-12 are fixed.

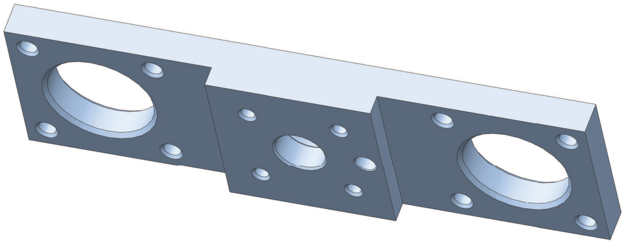

Figure 104: Tool platform where a gripper can be connected.

5.10 CONTROL ARCHITECTURE

The control architecture of ICABOT is based on the EtherCAT communication protocol developed by Beckhoff Automation [120]. EtherCAT is an Ethernet-based fieldbus system that has set new standards for real-time performance and topology flexibility, whilst meeting or undercutting fielbus cost levels [121]. It is also an international standard (IEC, ISO and SEMI).

The next sections aims at presenting the EtherCAT protocol and the software required to create a virtual PLC that manages the communication within the network.

5.10.1 *EtherCAT protocol*

The protocol is Ethernet based, which allows the use of the same network cables and some other network device (e.g. network cards), but it uses a different way of handling the Ethernet frames for the communication. In fact, the frames are processed *on the fly* and the Field Memory Management Modules (FMMUs) are used for this purpose. The FMMUs in each device on the bus readand shift the data to the devicefor processing and at the same time the frame is sent to the next device. Due to this way of handling the frames, delay of only a

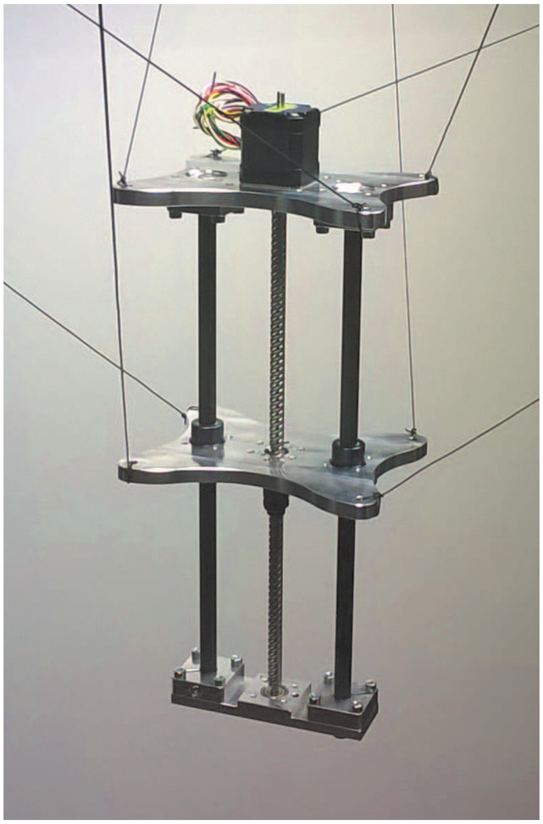

Figure 105: Prototype of the reconfigurable end-effector.

few nanoseconds occurs in the fieldbus, creating hard real-time communication.

EtheCAT implements a Master-Slave communication where the Master device manages the whole process. The Master device is an industrial PC, on which a software PLC is installed ans Slave devices are inputs, outputs, communication modules or servo drives connected with Ethernet cable. The EtherCAT fieldbus support almost every network topology and no additional switches are needed because the communication interfaces are integrated in the bus couplers.

5.10.2 *Twincat 3*

TwinCAT 3 is a real-time extension of Microsoft Windows operating system. It turns every compatible PC to a controller working in real-time. The possibility to replace all common PLC systems with TwinCAT and an industrial PC is a powerful tool to increase the flexibility of the system. Furthermore,the development environment is the well known Visual Studio 2010. In addition to the possibilities of controlling programming according to the 3^{rd} edition of IEC 61131-3, the TwinCAT 3 architecture allows the use of C and C++ as programming languages as well as the link to Matlab/Simulink. This opens up completely new application possibilities that exploit the computational power of these programming languages such as the use of a great variety of toolboxes for simulation, optimization and rapid prototyping. In particular, the integration of Matlab/Simulink enables the execution of TwinCAT modules that were generated as models in the Simulink simulation environment and the possibility to link Matlab using the ADS communication.

The functions of the high-level software developed in Matlab (with appropriate toolboxes) enable the easy design of controllers using calculation methods based on closed loop control theory. Controllers designed in this way can subsequently be simulated and validated together with a model of the controlled system in Simulink. But also entire production plants can be modeled and tested in simulation. This is advantageous in various ways in the process of developing a machine. For example, no real machine needs to be available for initial tests of the control software. Moreover, the danger of damage to the machine through initial commissioning with flawed control software is reduced.

To use control programs and controllers designed in Matlab/Simulink with the real machine after successful tests in simulation, the developed algorithms can be programmed manually in real-time-capable languages like C++ or PLC code. Simpler and significantly less prone to error is the automatic conversion of the already implemented algorithms into real-time-capable program modules. Two licenses allow to build interfaces between Matlab/Simulink and Twincat 3:

- The TE1400 TwinCAT Target license for Matlab/Simulink enables the user to generate real time capable modules, which can be executed on the TwinCAT 3 runtime. These modules can be instantiated multiple times, parameterized and debugged in the TwinCAT 3 engineering environment.

- The TE1410 Interface license for Matlab/Simulink provides an interface for data exchange between the TwinCAT 3 runtime and Simulink. The data exchange is based on ADS communication, which is managed by Simulink blocks provided by a Simulink library, delivered as a part of this software package.

The control architecture developed for ICABOT consists of a two-level framework as shown in Fig. 106:

- High-level software developed in Matlab. The CDPR simulator described in Sec. 5.4 is the core of the software along with a class for the ADS communication. The main goal of the high-level software is the configuration of the workcell, the calculation of the reference trajectories required for a movement and the algorithms for inverse kinematics/dynamics.

- Low-level software developed in Twincat 3. The software receives commands and data from Matlab and performs several tasks such as:

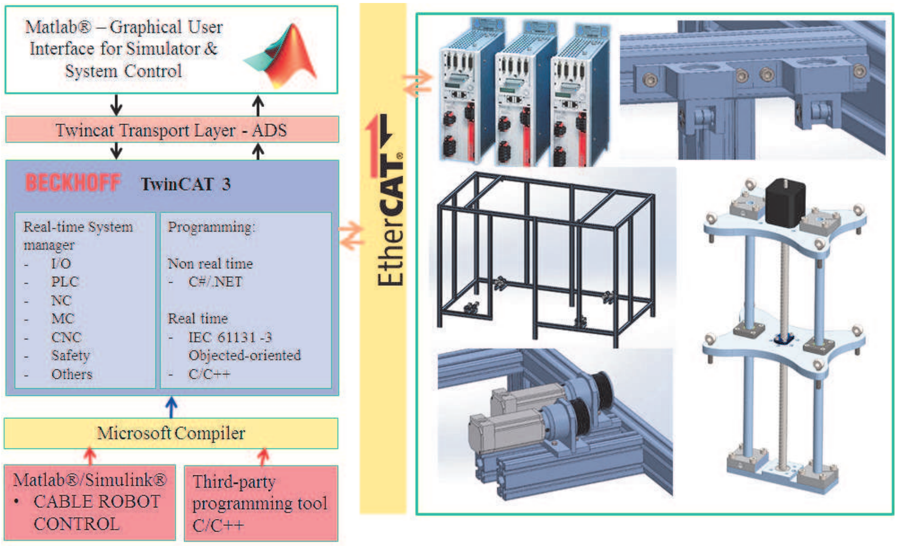

Figure 106: Control architecture with Matlab/Twincat 3

- enabling the motors;
- reading the position of the motors;
- setting the position of the motor during the homing process;
- moving the motors with point-to-point movements;
- moving the motors with user-defined trajectories;
- moving the motors using torque control;
- controlling input/output;

5.11 ELECTRIC SCHEME

In the following, the main characteristics of the electric scheme designed for ICABOT are briefly outlined. There are two different supply voltages:

1. Single phase **220** V_{AC}: serves drives' main power supply;
2. 24 V_{DC}: serves the safety circuit and the drives' control electronics

A master switch controls the mains of the electric panel. After turning the switch on, the drives are immediately turned on, however, the device remains in the emergency status until the start button is pressed. The emergency and the ready states are indicated by a red and a green lamp, respectively. A magneto thermal switch was installed to protect against short-circuit and non short-term overloads. Additionally, all the components are protected by fuses. The servo drives AX5020 are connected to a high voltage input, which is the

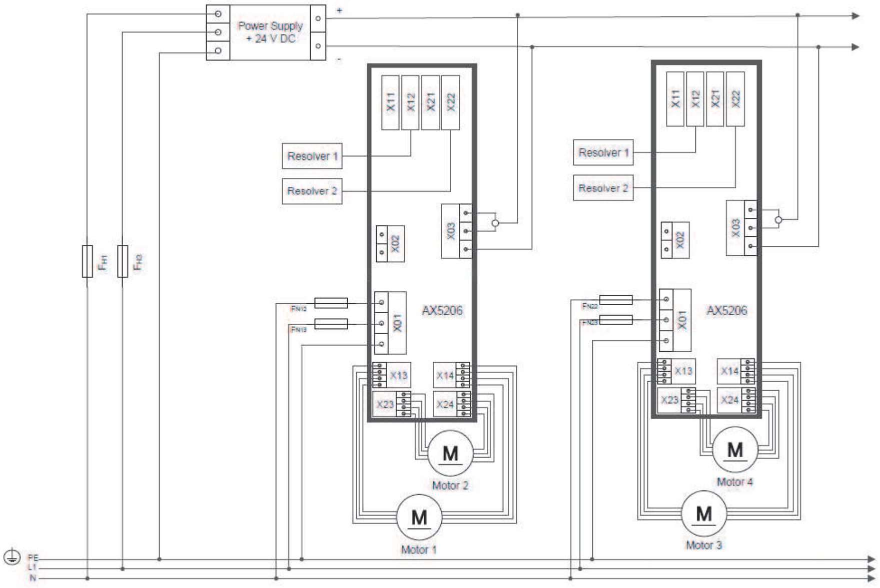

Figure 107: Simplified electric scheme for two of the four drives of the ICABOT prototype.

main power supply, and a low voltage input for the control electronics (Fig. 107). Each drive controls two motors and two resolvers.

In accordance with the UNI EN ISO 10218 [32, 33], the robot workcell is equipped with a safety circuit (108) that cuts the power supplied to the motors in case of fault. The safety circuit is guarded by a safety relay ABB RT7. Therefore, the following devices are capable of switching the machine to the emergency status:

- the stop button;
- the emergency buttons;
- the watchdog of the drives;
- the safety door switches.

Thus, the run status can be achieved only once all the previous contacts have been closed,

5.12 PRELIMINARY RESULTS

In this section we illustrate a first experimental test which was carried out with the prototype of ICABOT presented in the previous sections. The control process for ICABOT is shown in Fig. 110. The user manage the configuration of the system and the trajectory planning using the simulator developed in MATLAB® and described in Sec. 5.4. A state machine is implemented in the virtual PLC, creating a real time interface with the hardware. The workflow in MATLAB® can be summarized as follows:

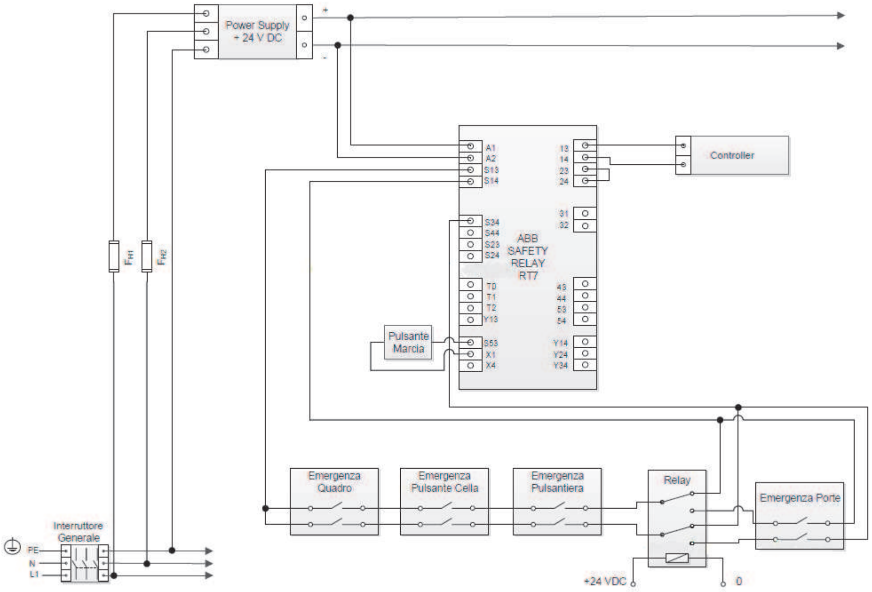

Figure 108: Simplified safety circuit of the ICABOT prototype

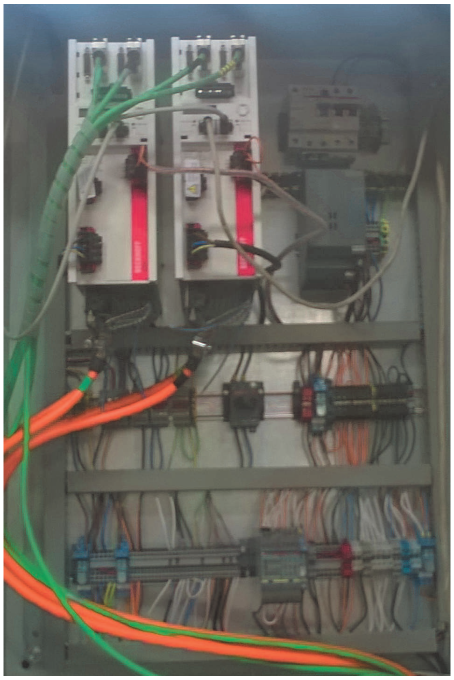

Figure 109: One of the electric cabinet of ICABOT.

1. Create an instance of the *cableRobot* object. Define the layout of the system using the available methods;
2. Create an instance of the *TwincatCOM* object and set up the ADS communication with TwinCAT $3^{®}$;
3. Enable the motors and define home position;

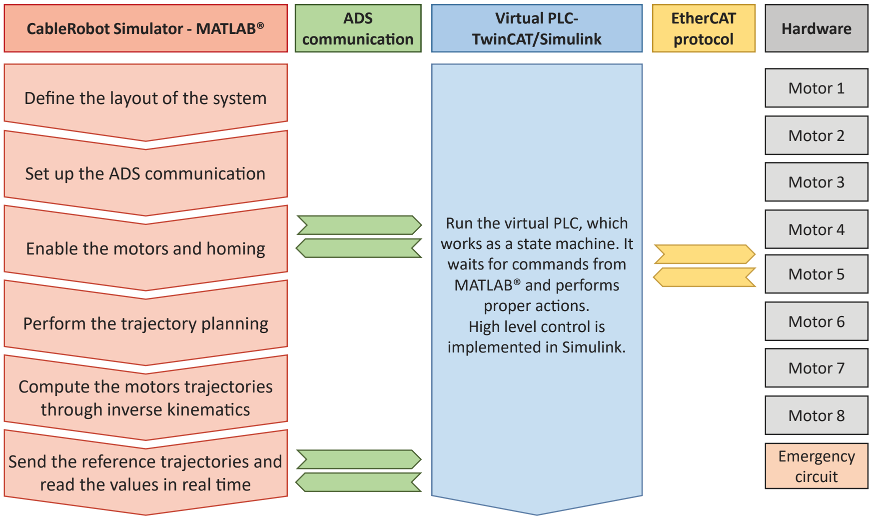

Figure 110: Control process for ICABOT

4. Define the movement in the operational space and perform the trajectory planning;

5. Compute the inverse kinematics and generate the reference trajectories for the motors;

6. Send the reference trajectories to TwinCAT 3® using the available methods and read the results in real time.

The virtual PLC is implemented in TwinCAT 3® and it is based on a state machine. The software runs cyclically waiting for commands from MATLAB®. When a movement command is received, the virtual PLC activates the high level control in Simulink® and elaborates the reference signals for the motors. The virtual PLC is constantly monitoring the emergency status of the systems and reacts in case of failures.

In the following example a jump movement has been performed. The movement is planned in the operational space and it is composed by three linear movements with different temporal parameters. Figure 111 illustrates the path in the operational space and the motor trajectories obtained through inverse kinematics in terms of position, velocity and acceleration. The reference trajectories for the motors are sent to the virtual PLC, which activate a Simulink® block that drives the motors using a built-in funcions for position control. Torque control can also be implemented.

Figure 112 reports the experimental results of the motor positions for the planned movement as well as the errors. The motors are able to follow the planned trajectories and the error is generally less than $10\mathrm{deg}$. Only motors 5 and 6 present high variability of the position error, which can be mitigate with a better characterizations of the

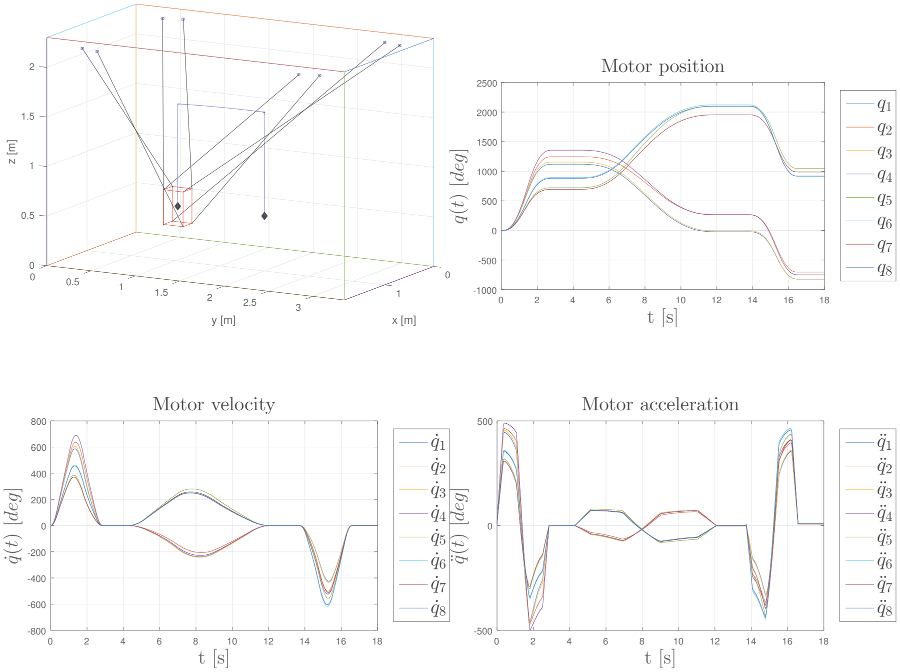

Figure 111: Reference trajectory for a jump movement: path in the operational space(a), position (b), velocity (c) and acceleration (d) for the motors.

motor low level control.All the motors present a the peak value of the errors in the middle of the vertical movements. This is caused by the higher velocities and accelerations characterizing the depart/approach movements (Fig.111) that, as a consequence, generate higher position errors. The errors can be strongly reduced with a better tuning of the PID control embedded in the drivers in terms of position, derivative and integral gains.

Figure 113 reports the results of the trajectory in the operational space obtained through forward kinematics. The initial and final points are $P_i = (1, 1, 0.5)\ m$ and $P_f = (1, 2, 0.5)\ m$, respectively. Figure 113(b) displays the root mean square of the error in the operational space. The error at the final position is $0.7\ mm$ whereas the maximum value of the position error is obtained during the vertical depart/approach and it is less than $11\ mm$. The orientation errors of the end-effector are less than $1\ deg$ along the whole trajectory.

Future work aims at improving the control algorithm of ICABOT. Improved Simulink control models can be tested and compared. Inertial sensors and camera-based systems will be considered for a direct measurement of the platform pose across the workspace.

To improve the accuracy of the system, force control with motor angular positions in the feedback loop can be implemented. The use of tension sensors to characterize the forces applied by the cable to the and-effector will increase the robustness of the control.

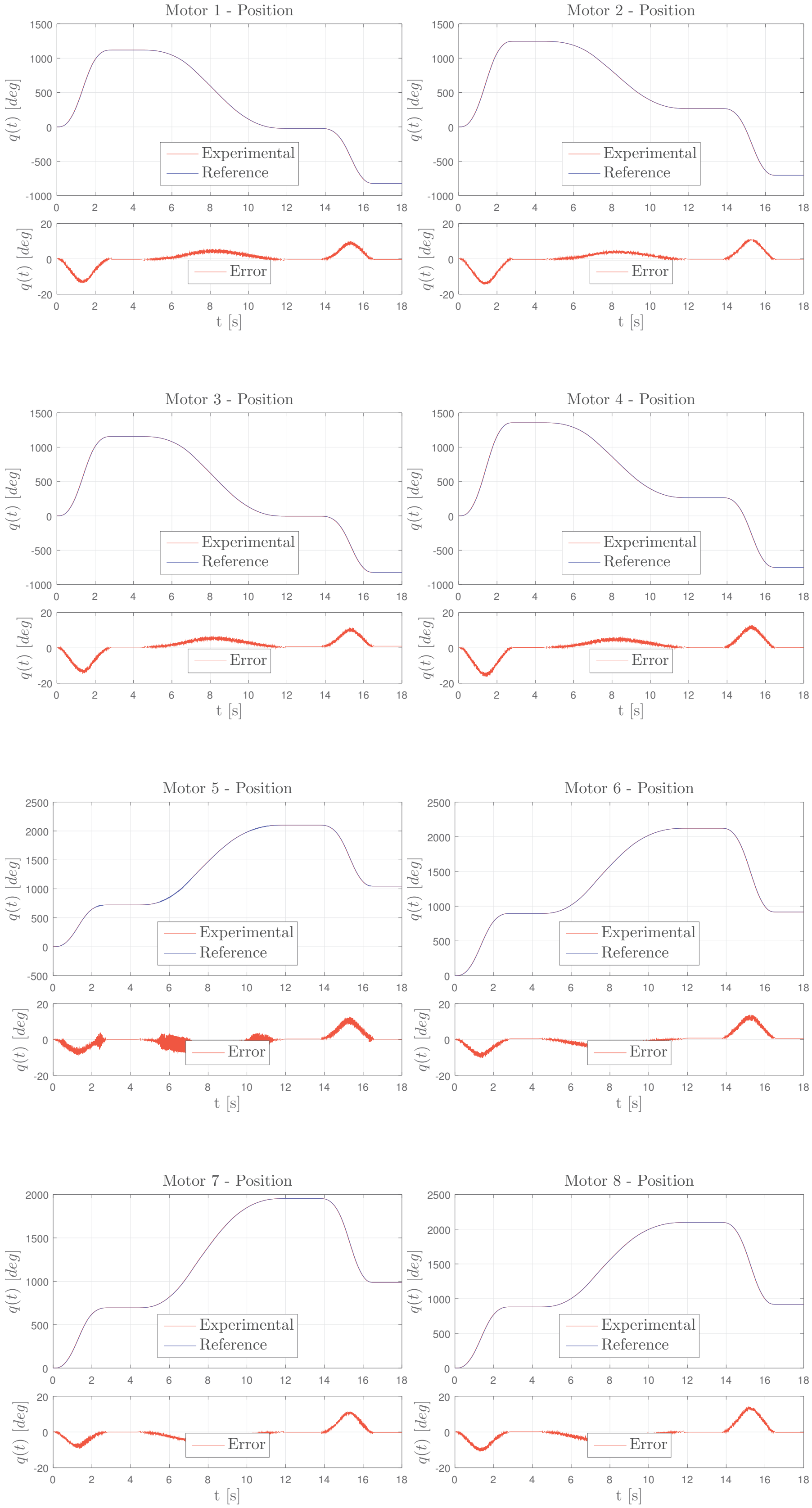

Figure 112: Reference and experimental positions of the motors.

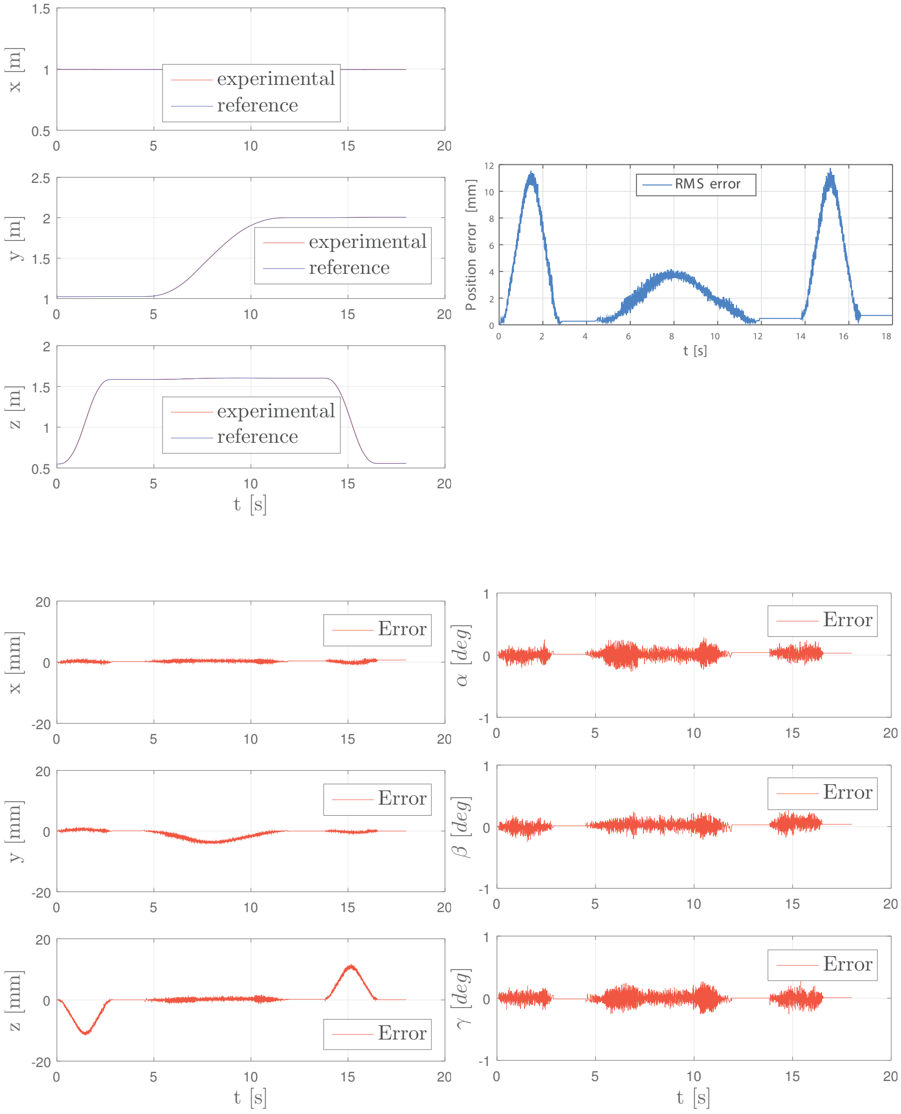

Figure 113: Position of the end-effector in the operational space (a). Position error (b). Orientation error (c).

5.13 CONCLUSION

This chapter presented the design of a novel family of Intelligent CAble-driven paralle roBOTs (ICABOTs) whose architecture and control were conceived to maximize the robot versatility to the task to be performed and the environment in which the robot is intended to operate. The development of ICABOT followed the paradigm of concurrent engineering which is based on an integrate approach for the design of a mechatronic system.

A software platform for the analysis and simulation of CDPRs was developed. The possibility to simulate and test multiple configurations of a cable robot is a promising way to improve versatility and reduce the design time. The simulator was fundamental to define the general layout and characterize the performance of the system.

Using the simulator, motors and drives were accurately selected whereas the main mechanical parts, conceived to be simple and versatile, were illustrated. Furthermore, the design of the reconfigurable end-effector introduced in Chapter 3 was presented.

An innovative control architecture was created for ICABOT based on the EtherCAT communication protocol. Matlab and Twincat 3 are used to build a powerful framework for industrial applications. First results demonstrate the possibility to control the motors with a user-defined trajectory computed in MATLAB.

6

CONCLUSION

The main contribution of this thesis consists in the introduction of new design solutions for mechatronic systems able to work inside large workspaces and safely collaborate with human operators. Cable driven Parallel Robots (CDPRs) are considered a promising technology able to fulfill the previous requirements and guarantee the maximum versatility. In fact, compared to rigid serial and parallel robots, they have several advantages such as large workspaces, high payloads per unit of weight, ease of construction, versatility and affordable costs. Therefore, applications that require a combination of such features are good candidates for the use of CDPRs. For such applications, two types of CDPRs can be found: fully-constrained, if the pose of the end effector is completely defined by the lengths of the cables, and under-constrained suspended, when the end effector makes use of gravity to get a pose. If compared to fully-constrained CDPRs, under-constrained Cable-Suspended Parallel Robots (CSPRs) can reduce collision risks between cables and obstacles since the mobile platform is suspended with cables connected to the ceiling, making cable-free the workspace below the platform.

A way to allow suspended CDPRs to enlarge the workspace, improve the versatility and reduce the collision risks is the possibility to design new mechanisms for the end-effector. To date, no contributions are present in literature with the aim of studying end-effector for under-constrained suspended CDPRs whose target is the interaction with workers, the reduction of collision between cables and obstacles and the maximization of the performance. Two innovative solutions are proposed in this work. The first solution consists of a reconfigurable end-effector whereas the second solution is an innovative model of micro-macro robot.

Chapter 3 introduced a planar cable-suspended parallel robot (CSPR) with reconfigurable end effector. The system was conceived for pick and place operations inside industrial environments. For such applications, the possibility to change the configuration of the cables at the end-effector level is a promising way to avoid collisions with obstacles in the approaching phases, while reducing at the same time the duration of motion in the remaining part of the trajectory. An optimized trajectory planning algorithm was proposed, which implements a pick and place operation in the task space with dynamic online reconfiguration of the end-effector. The results on a simplified scenario with a planar system demonstrate the ability of the system to obtain reduced movement times together with obstacle avoidance.

From the planar mechanism, we developed a system with 7-DOFs and 8 cables which has the capability of modifying the position of the cable anchor points on the end-effector using a linear actuator. The model of the reconfigurable end-effector consists of a main structure and a translating platform which can slide along a linear axis. A simple pick and place task composed of three linear movements was defined and the design of the end-effector was optimized to minimize the linear actuator force. Among the design variables that affect the linear actuator force, mass distribution was found to be the most significant one.

Chapter 4 introduced the model of a planar under-actuated Cable-Driven Micro-Macro Robot. The system consists of a Cable-Suspended Parallel Robot whose end-effector is a two-link passive serial manipulator. The kinematic and dynamic models were presented and the *differential flatness* framework was applied to make the system controllable for point-to-point movements. The application of *differential flatness* for cable-driven robots is a further novelty of this work. The system can increase the reachable workspace of a traditional CSPR. Furthermore, u-CDMMRs are potential solutions for applications involving inspection inside large workspaces where obstacles may be present. The work proposed a novel optimization framework for the design of u-CDMMRs. Given a point-to-point movement to execute, a multi-objective optimization was used to minimize two objective functions simultaneously: the movement time and the control effort required by the actuators. Optimal time-energy control was applied to compute the optimal trajectory. This approach allows to analyze the effect of the design parameters, such as link dimensions, mass distributions, and spring stiffness on the performance of the system.

Chapter 5 presented the design of a novel family of Intelligent CAble-driven paralle roBOTs (ICABOTs) whose architecture and control were conceived to maximize the robot versatility to the task to be performed and the environment in which the robot is intended to operate. The development of ICABOT followed the paradigm of concurrent engineering which is based on an integrate approach for the design of a mechatronic system. A software platform for the analysis and simulation of CDPRs was developed and described as long as the design of the mechanical parts. The possibility to simulate and test multiple configurations of a cable robot is a promising way to improve versatility and reduce the design time. The simulator was fundamental to define the general layout and characterize the performance of the system. Finally, an innovative control architecture was created for ICABOT based on the EtherCAT communication protocol. Matlab and Twincat 3 are used to build a powerful framework for the prototype than can be exploited the future industrial applications. First experimental results were presented and discussed.

From the theoretical point of view, the studies on the reconfigurable cable-driven systems and cable-driven micro-macro robot may be further extended, for example by studying new performance indexes for the reachable workspace. The possibility to introduce further degrees of freedom in the end-effector can be a further improvement as well as the use of compliant or passive joints. Also, the introduction of passive cables and springs may be an effective choice to reduce design complexity and costs, especially when the dynamic performances of the device are not a major concern. Furthermore, new experimental tests will be carried out with the purpose of validating the reconfigurable end-effector and demonstrate the ability to avoid collisions with obstacles. Future works aims also at demonstrating the effectiveness of these design solutions through real industrial applications.

A

APPENDIX A

$$\begin{aligned}
b_1 = &-\frac{1}{2}\dot{v}_5^2 \sin(2v_7) + \frac{1}{2}\dot{v}_6^2 \sin(2v_7) + \frac{1}{2}\dot{v}_4^2 (\cos v_5)^2 \sin(2v_7) \\
&- \frac{1}{2}\dot{v}_4^2 (\cos v_6)^2 \sin(2v_7) + \frac{1}{2}\dot{v}_5^2 (\cos v_6)^2 \sin(2v_7) \\
&+ \frac{1}{2}\dot{v}_4^2 (\cos v_5)^2 (\cos v_6)^2 \sin(2v_7) + \dot{v}_4 \dot{v}_6 \cos v_5 \sin(2v_7) \\
&+ \dot{v}_5 \dot{v}_6 \sin v_6 \cos(2v_7) - \dot{v}_4^2 \cos v_5 \cos v_6 \sin v_5 \cos(2v_7) \\
&+ \dot{v}_4 \dot{v}_5 \cos v_5 \sin v_6 \cos(2v_7) - \dot{v}_4 \dot{v}_6 \cos v_6 \sin v_5 \cos(2v_7) \\
&+ \dot{v}_4 \dot{v}_5 \cos v_6 \sin v_5 \sin v_6 \sin(2v_7)
\end{aligned} \tag{142}$$

$$\begin{aligned}
b_2 = &\frac{1}{2}\dot{v}_5^2 \sin(2v_7) - \frac{1}{2}\dot{v}_6^2 \sin(2v_7) - \frac{1}{2}\dot{v}_4^2 (\cos v_5)^2 \sin(2v_7) \\
&+ \frac{1}{2}\dot{v}_4^2 (\cos v_6)^2 \sin(2v_7) - \frac{1}{2}\dot{v}_5^2 (\cos v_6)^2 \sin(2v_7) \\
&- \frac{1}{2}\dot{v}_4^2 (\cos v_5)^2 (\cos v_6)^2 \sin(2v_7) - \dot{v}_4 \dot{v}_6 \cos v_5 \sin(2v_7) \\
&- \dot{v}_5 \dot{v}_6 \sin v_6 \cos(2v_7) + \dot{v}_4^2 \cos v_5 \cos v_6 \sin v_5 \cos(2v_7) \\
&- \dot{v}_4 \dot{v}_5 \cos v_5 \sin v_6 \cos(2v_7) + \dot{v}_4 \dot{v}_6 \cos v_6 \sin v_5 \cos(2v_7) \\
&- \dot{v}_4 \dot{v}_5 \cos v_6 \sin v_5 \sin v_6 \sin(2v_7)
\end{aligned} \tag{143}$$

$$b_3 = -\dot{v}_5 \dot{v}_6 \sin(v_6) + \dot{v}_4 \dot{v}_5 \cos(v_5) \sin(v_6) + \dot{v}_4 \dot{v}_6 \cos(v_6) \sin(v_5) \tag{144}$$

$$\begin{aligned}
b_4 = &-\dot{v}_5^2 \cos(2v_7) + \dot{v}_6^2 \cos(2v_7) + \dot{v}_4^2 (\cos v_5)^2 \cos(2v_7) \\
&+ \dot{v}_5^2 (\cos v_6)^2 \cos(2v_7) - \dot{v}_4^2 (\cos v_6)^2 \cos(2v_7) \\
&+ \dot{v}_4^2 (\cos v_5)^2 (\cos v_6)^2 \cos(2v_7) + 2\dot{v}_4 \dot{v}_6 \cos v_5 \cos(2v_7) \\
&- 2\dot{v}_5 \dot{v}_6 \sin v_6 \sin(2v_7) + 2\dot{v}_4^2 \cos v_5 \cos v_6 \sin v_5 \sin(2v_7) \\
&- 2\dot{v}_4 \dot{v}_5 \cos v_5 \sin v_6 \sin(2v_7) + 2\dot{v}_4 \dot{v}_6 \cos v_6 \sin v_5 \sin(2v_7) \\
&+ 2\dot{v}_4 \dot{v}_5 \cos v_6 \sin v_5 \sin v_6 \sin(2v_7)
\end{aligned} \tag{145}$$

$$\begin{aligned}
b_5 = &-2\dot{v}_5 \dot{v}_6 \cos v_6 \cos(v_7) - \dot{v}_4^2 \cos v_6 \sin v_6 \sin(v_7) + \dot{v}_5^2 \cos v_6 \sin v_6 \sin(v_7) \\
&+ 2\dot{v}_4 \dot{v}_5 \sin v_5 \sin(v_7) - 2\dot{v}_4 \dot{v}_5 (\cos v_6)^2 \sin v_5 \sin(v_7) \\
&- \dot{v}_4^2 \cos v_5 \sin v_5 \sin v_6 \cos(v_7) - 2\dot{v}_4 \dot{v}_6 \sin v_5 \sin v_6 \cos(v_7) \\
&+ \dot{v}_4^2 (\cos v_5)^2 \cos v_6 \sin v_6 \sin(v_7)
\end{aligned} \tag{146}$$

$$\begin{aligned} b_6 = {} & 2\dot{v}_4\dot{v}_5 \sin v_5 \cos(v_7) - \dot{v}_4^2 \cos v_6 \sin v_6 \cos(v_7) \\ & + \dot{v}_5^2 \cos v_6 \sin v_6 \cos(v_7) + 2\dot{v}_5\dot{v}_6 \cos v_6 \sin(v_7) \\ & - 2\dot{v}_4\dot{v}_5 (\cos v_6)^2 \sin v_5 \cos(v_7) + \dot{v}_4^2 \cos v_5 \sin v_5 \sin v_6 \sin(v_7) \\ & + 2\dot{v}_4\dot{v}_6 \sin v_5 \sin v_6 \sin(v_7) + \dot{v}_4^2 (\cos v_5)^2 \cos v_6 \sin v_6 \cos(v_7) \end{aligned} \tag{147}$$

$$\begin{aligned} A_4 = {} & I_{2yz} \cos v_5 \cos(v_7) - I_{2zz} \sin v_5 \sin v_6 + I_{2xz} \cos v_5 \sin(v_7) \\ & + I_{2yz} \cos v_6 \sin v_5 \sin(v_7) - I_{2xz} \cos v_6 \sin v_5 \cos(v_7) \end{aligned} \tag{148}$$

$$A_5 = I_{2xz} \sin v_6 \cos(v_7) - I_{2zz} \cos v_6 - I_{2yz} \sin v_6 \sin(v_7) \tag{149}$$

$$A_6 = I_{2yz} \cos(v_7) + I_{2xz} \sin(v_7) \tag{150}$$

$$A_7 = I_{2zz} \tag{151}$$

BIBLIOGRAPHY

[1] E. Cevikcan, “A mathematical programming approach for walking-worker assembly systems,” *Assembly Automation*, vol. 34, no. 1, pp. 56–68, 2014.

[2] J. P. Shewchuk, “Worker allocation in lean u-shaped production lines,” *International Journal of Production Research*, vol. 46, no. 13, pp. 3485–3502, 2008.

[3] J. Heilala, J. Montonen, and O. Väätäinen, “Life cycle and unit-cost analysis for modular reconfigurable flexible light assembly systems,” *Proceedings of the Institution of Mechanical Engineers, Part B: Journal of Engineering Manufacture*, vol. 222, no. 10, pp. 1289–1299, 2008.

[4] M. Hägele, J. Neugebauer, and R. D. Schraft, “From robots to robot assistants,” in *Proc. of the 32nd ISR (International Symposium on Robotics)*, pp. 19–21, 2001.

[5] M. Zäh, M. Beetz, K. Shea, G. Reinhart, K. Bender, C. Lau, M. Ostgathe, W. Vogl, M. Wiesbeck, M. Engelhard, *et al.*, “Changeable and reconfigurable manufacturing systems,” *The cognitive factory, Springer, London*, pp. 355–371, 2009.

[6] J. Krüger, T. K. Lien, and A. Verl, “Cooperation of human and machines in assembly lines,” *CIRP Annals-Manufacturing Technology*, vol. 58, no. 2, pp. 628–646, 2009.

[7] G. Michalos, S. Makris, J. Spiliotopoulos, I. Misios, P. Tsarouchi, and G. Chryssolouris, “Robo-partner: Seamless human-robot cooperation for intelligent, flexible and safe operations in the assembly factories of the future,” *Procedia CIRP*, vol. 23, pp. 71–76, 2014.

[8] M. Hermann, T. Pentek, and B. Otto, “Design principles for industrie 4.0 scenarios,” in *2016 49th Hawaii International Conference on System Sciences (HICSS)*, pp. 3928–3937, IEEE, 2016.

[9] R. Alami, A. Albu-Schäffer, A. Bicchi, R. Bischoff, R. Chatila, A. De Luca, A. De Santis, G. Giralt, J. Guiochet, G. Hirzinger, *et al.*, “Safe and dependable physical human-robot interaction in anthropic domains: State of the art and challenges,” in *2006 IEEE/RSJ International Conference on Intelligent Robots and Systems*, pp. 1–16, IEEE, 2006.

[10] R. Bemelmans, G. J. Gelderblom, P. Jonker, and L. De Witte, "Socially assistive robots in elderly care: A systematic review into effects and effectiveness," *Journal of the American Medical Directors Association*, vol. 13, no. 2, pp. 114–120, 2012.

[11] T. L. Chen, M. Ciocarlie, S. Cousins, P. Grice, K. Hawkins, K. Hsiao, C. C. Kemp, C.-H. King, D. A. Lazewatsky, A. E. Leeper, *et al.*, "Robots for humanity: Using assistive robots to empower people with disabilities," 2013.

[12] H. I. Krebs, J. J. Palazzolo, L. Dipietro, M. Ferraro, J. Krol, K. Rannekleiv, B. T. Volpe, and N. Hogan, "Rehabilitation robotics: Performance-based progressive robot-assisted therapy," *Autonomous robots*, vol. 15, no. 1, pp. 7–20, 2003.

[13] M. A. Goodrich and A. C. Schultz, "Human-robot interaction: a survey," *Foundations and trends in human-computer interaction*, vol. 1, no. 3, pp. 203–275, 2007.

[14] G. Kwakkel, B. J. Kollen, and H. I. Krebs, "Effects of robot-assisted therapy on upper limb recovery after stroke: a systematic review," *Neurorehabilitation and neural repair*, 2007.

[15] K. Kosuge, H. Yoshida, D. Taguchi, T. Fukuda, K. Hariki, K. Kanitani, and M. Sakai, "Robot-human collaboration for new robotic applications," in *Industrial Electronics, Control and Instrumentation, 1994. IECON'94., 20th International Conference on*, vol. 2, pp. 713–718, IEEE, 1994.

[16] J. Edward, C. W. Wannasuphoprasit, and M. A. Peshkin, "Cobots: Robots for collaboration with human operators," in *International Mechanical Engineering Congress and Exposition, Atlanta*, Citeseer, 1996.

[17] O. Khatib, "Mobile manipulation: The robotic assistant," *Robotics and Autonomous Systems*, vol. 26, no. 2, pp. 175–183, 1999.

[18] R. D. Schraft, C. Meyer, C. Parlitz, and E. Helms, "Powermate-a safe and intuitive robot assistant for handling and assembly tasks," in *Proceedings of the 2005 IEEE International Conference on Robotics and Automation*, pp. 4074–4079, IEEE, 2005.

[19] S. Takata and T. Hirano, "Human and robot allocation method for hybrid assembly systems," *CIRP Annals-Manufacturing Technology*, vol. 60, no. 1, pp. 9–12, 2011.

[20] M. Morioka and S. Sakakibara, "A new cell production assembly system with human–robot cooperation," *CIRP Annals-Manufacturing Technology*, vol. 59, no. 1, pp. 9–12, 2010.

[21] H. Medellin, J. Corney, J. Ritchie, and T. Lim, "Automatic generation of robot and manual assembly plans using octrees," *Assembly Automation*, vol. 30, no. 2, pp. 173–183, 2010.

[22] P. Gil, J. Pomares, S. Puente, F. Candelas, G. García, J. Corrales, and F. Torres, "A cooperative robotic system based on multiple sensors to construct metallic structures," *The International Journal of Advanced Manufacturing Technology*, vol. 45, no. 5-6, pp. 616–630, 2009.

[23] S. Sugita, T. Itaya, and Y. Takeuchi, "Development of robot teaching support devices to automate deburring and finishing works in casting," *The International Journal of Advanced Manufacturing Technology*, vol. 23, no. 3-4, pp. 183–189, 2004.

[24] G. Michalos, S. Makris, P. Tsarouchi, T. Guasch, D. Kontovrakis, and G. Chryssolouris, "Design considerations for safe human-robot collaborative workplaces," *Procedia CIRP*, vol. 37, pp. 248–253, 2015.

[25] S. Haddadin, A. Albu-Schaffer, A. De Luca, and G. Hirzinger, "Collision detection and reaction: A contribution to safe physical human-robot interaction," in *2008 IEEE/RSJ International Conference on Intelligent Robots and Systems*, pp. 3356–3363, IEEE, 2008.

[26] J. A. Corrales Ramón, G. J. García Gómez, F. Torres Medina, and V. Perdereau, "Cooperative tasks between humans and robots in industrial environments," 2012.

[27] N. Pedrocchi, F. Vicentini, M. Matteo, and L. M. Tosatti, "Safe human-robot cooperation in an industrial environment," *International Journal of Advanced Robotic Systems*, vol. 10, 2013.

[28] B. Schmidt and L. Wang, "Contact-less and programming-less human-robot collaboration," *Procedia CIRP*, vol. 7, pp. 545–550, 2013.

[29] F. Flacco, T. Kröger, A. De Luca, and O. Khatib, "A depth space approach to human-robot collision avoidance," in *Robotics and Automation (ICRA), 2012 IEEE International Conference on*, pp. 338–345, IEEE, 2012.

[30] C. Morato, K. N. Kaipa, B. Zhao, and S. K. Gupta, "Toward safe human robot collaboration by using multiple kinects based real-time human tracking," *Journal of Computing and Information Science in Engineering*, vol. 14, no. 1, p. 011006, 2014.

[31] T. Arai, R. Kato, and M. Fujita, "Assessment of operator stress induced by robot collaboration in assembly," *CIRP Annals-Manufacturing Technology*, vol. 59, no. 1, pp. 5–8, 2010.

[32] ISO, "Robots for industrial environments safety requirements-part 1," ISO ISO 10218-1, International Organization for Standardization, Geneva, Switzerland, 2011.

[33] ISO, "Robots for industrial environments safety requirements-part 2," ISO ISO 10218-2, International Organization for Standardization, Geneva, Switzerland, 2011.

[34] IEC, "Safety of machinary - electrical equipment of machines - part 1: General requirements," IEC IEC 60204-1, International Electrotechnical Commission, Geneva, Switzerland, 2005.

[35] I. F. of Robotics, "http://www.ifr.org/," 2016.

[36] kuka, "http://www.kuka-robotics.com/," 2016.

[37] S. Haddadin, M. Suppa, S. Fuchs, T. Bodenmüller, A. Albu-Schäffer, and G. Hirzinger, "Towards the robotic co-worker," in *Robotics Research*, pp. 261–282, Springer, 2011.

[38] Fanuc, "http://www.fanuc.eu/uk/en," 2016.

[39] ABB, "http://www.abb.com/," 2016.

[40] L. Sciavicco and B. Siciliano, *Modelling and control of robot manipulators*. Springer Science & Business Media, 2012.

[41] S. K. Mustafa, W. B. Lim, G. Yang, S. H. Yeo, W. Lin, and S. K. Agrawal, *Cable-driven robots*. Handbook of Manufacturing Engineering and Technology, 2015.

[42] C. Gosselin, "Cable-driven parallel mechanisms: state of the art and perspectives," *Mechanical Engineering Reviews*, vol. 1, no. 1, pp. 1–17, 2014.

[43] D. Cunningham and H. H. Asada, "The winch-bot: A cable-suspended, under-actuated robot utilizing parametric self-excitation," in *Robotics and Automation, 2009. ICRA'09. IEEE International Conference on*, pp. 1844–1850, IEEE, 2009.

[44] C. Gosselin, S. Lefrançois, and N. Zoso, "Underactuated cable-driven robots: machine, control and suspended bodies," in *Brain, Body and Machine*, pp. 311–323, Springer, 2010.

[45] L. L. Cone, "Skycam: An aerial robotic camera system," *Byte*, vol. 10, no. 10, pp. 122–132, 1985.

[46] J. Albus, R. Bostelman, and N. Dagalakis, "The nist robocrane," *Journal of Robotics System*, vol. 10, no. 5, 1992.

[47] C. S. Holland and D. J. Cannon, "Cable array robot for material handling," Nov. 30 2004. US Patent 6,826,452.

[48] A. Pott, C. Meyer, and A. Verl, "Large-scale assembly of solar power plants with parallel cable robots," in *Robotics (ISR), 2010 41st International Symposium on and 2010 6th German Conference on Robotics (ROBOTIK)*, pp. 1–6, VDE, 2010.

[49] J.-B. Izard, M. Gouttefarde, M. Michelin, O. Tempier, and C. Baradat, "A reconfigurable robot for cable-driven parallel robotic research and industrial scenario proofing," in *Cable-Driven Parallel Robots*, pp. 135–148, Springer, 2013.

[50] R. L. Williams II, "Five-hundred meter aperture spherical radio telescope (fast) cable-suspended robot model and comparison with the arecibo observatory," *Internet Publication, www.ohio.edu/people/williar4/html/pdf/FAST.pdf*, 2015.

[51] P. Gallina, G. Rosati, and A. Rossi, "3-dof wire driven planar haptic interface," *Journal of Intelligent and Robotic Systems*, vol. 32, no. 1, pp. 23–36, 2001.

[52] P. Gallina and G. Rosati, "Manipulability of a planar wire driven haptic device," *Mechanism and Machine Theory*, vol. 37, no. 2, pp. 215–228, 2002.

[53] G. Boschetti, G. Rosati, and A. Rossi, "A haptic system for robotic assisted spine surgery," in *Proceedings of 2005 IEEE Conference on Control Applications, 2005. CCA 2005.*, pp. 19–24, IEEE, 2005.

[54] C. Fanin, P. Gallina, A. Rossi, U. Zanatta, and S. Masiero, "Nerebot: a wire-based robot for neurorehabilitation," in *Proceedings of the 8th International Conference on Rehabilitation Robotics*, pp. 23–25, 2003.

[55] G. Rosati, P. Gallina, S. Masiero, and A. Rossi, "Design of a new 5 dof wire-based robot for rehabilitation," in *9th International Conference on Rehabilitation Robotics, 2005. ICORR 2005.*, pp. 430–433, IEEE, 2005.

[56] V. Vashista, S. Mustafa, and S. K. Agrawal, "Experimental studies on the human gait using a tethered pelvic assist device (t-pad)," in *2011 IEEE International Conference on Rehabilitation Robotics*, pp. 1–6, IEEE, 2011.

[57] Y. Mao and S. K. Agrawal, "Design of a cable-driven arm exoskeleton (carex) for neural rehabilitation," *IEEE Transactions on Robotics*, vol. 28, no. 4, pp. 922–931, 2012.

[58] P. Bosscher, A. T. Riechel, and I. Ebert-Uphoff, "Wrench-feasible workspace generation for cable-driven robots," *Robotics, IEEE Transactions on*, vol. 22, no. 5, pp. 890–902, 2006.

[59] N. Zhang and W. Shang, "Dynamic trajectory planning of a 3-dof under-constrained cable-driven parallel robot," *Mechanism and Machine Theory*, vol. 98, pp. 21–35, 2016.

[60] J. Lamaury and M. Gouttefarde, "A tension distribution method with improved computational efficiency," in *Cable-driven parallel robots*, pp. 71–85, Springer, 2013.

[61] J. Lamaury, M. Gouttefarde, M. Michelin, and O. Tempier, "Design and control of a redundant suspended cable-driven parallel robots," in *Latest Advances in Robot Kinematics*, pp. 237–244, Springer, 2012.

[62] J. Lamaury and M. Gouttefarde, "Control of a large redundantly actuated cable-suspended parallel robot," in *Robotics and Automation (ICRA), 2013 IEEE International Conference on*, pp. 4659–4664, IEEE, 2013.

[63] R. L. Williams and P. Gallina, "Planar cable-direct-driven robots, part i: Kinematics and statics," in *Proceedings of the 2001 ASME Design Technical Conference, 27th Design Automation Conference*, no. 26, pp. 178–186, 2001.

[64] A. Pott and V. Schmidt, "On the forward kinematics of cable-driven parallel robots," in *Intelligent Robots and Systems (IROS), 2015 IEEE/RSJ International Conference on*, pp. 3182–3187, IEEE, 2015.

[65] J.-P. Merlet and J. Alexandre-dit Sandretto, "The forward kinematics of cable-driven parallel robots with sagging cables," in *Cable-Driven Parallel Robots*, pp. 3–15, Springer, 2015.

[66] V. Schmidt, B. Müller, and A. Pott, "Solving the forward kinematics of cable-driven parallel robots with neural networks and interval arithmetic," in *Computational Kinematics*, pp. 103–110, Springer, 2014.

[67] P. Gallina, A. Rossi, and R. L. Williams II, "Planar cable-direct-driven robots, part ii: Dynamics and control," in *ASME. DECT2001 ASME Design Engineering Technical Conference. Pittsburgh: ASME Publisher*, vol. 2, pp. 1241–1247, 2001.

[68] G. Rosati, D. Zanotto, and A. Rossi, "Performance assessment of a 3d cable-driven haptic device," in *ASME 2008 International Mechanical Engineering Congress and Exposition*, pp. 597–606, American Society of Mechanical Engineers, 2008.

[69] Y. Shen, H. Osumi, and T. Arai, "Set of manipulating forces in wire driven systems," in *Intelligent Robots and Systems' 94.'Advanced Robotic Systems and the Real World', IROS'94. Proceedings*

of the IEEE/RSJ/GI International Conference on, vol. 3, pp. 1626–1631, IEEE, 1994.

[70] P. Gallina and G. Rosati, "Manipulability of a planar wire driven haptic device," *Mechanism and Machine Theory*, vol. 37, no. 2, pp. 215–228, 2002.

[71] S. Krut, F. Pierrot, *et al.*, "Velocity performance indices for parallel mechanisms with actuation redundancy," *Robotica*, vol. 22, no. 02, pp. 129–139, 2004.

[72] G. Rosati, D. Zanotto, and S. K. Agrawal, "On the design of adaptive cable-driven systems," *Journal of mechanisms and robotics*, vol. 3, no. 2, p. 021004, 2011.

[73] D. Zanotto, G. Rosati, S. Minto, and A. Rossi, "Sophia-3: A semi-adaptive cable-driven rehabilitation device with a tilting working plane," *Robotics, IEEE Transactions on*, vol. 30, no. 4, pp. 974–979, 2014.

[74] X. Zhou, S.-k. Jun, and V. Krovi, "Tension distribution shaping via reconfigurable attachment in planar mobile cable robots," *Robotica*, vol. 32, no. 02, pp. 245–256, 2014.

[75] D. Q. Nguyen, M. Gouttefarde, O. Company, and F. Pierrot, "On the analysis of large-dimension reconfigurable suspended cable-driven parallel robots," in *Robotics and Automation (ICRA), 2014 IEEE International Conference on*, pp. 5728–5735, IEEE, 2014.

[76] L. Gagliardini, S. Caro, M. Gouttefarde, and A. Girin, "A reconfiguration strategy for reconfigurable cable-driven parallel robots," in *Robotics and Automation (ICRA), 2015 IEEE International Conference on*, pp. 1613–1620, IEEE, 2015.

[77] K. G. Shin and N. D. McKay, "Minimum-time control of robotic manipulators with geometric path constraints," *Automatic Control, IEEE Transactions on*, vol. 30, no. 6, pp. 531–541, 1985.

[78] D. Costantinescu and E. Croft, "Smooth and time-optimal trajectory planning for industrial manipulators along specified paths," *Journal of robotic systems*, vol. 17, no. 5, pp. 233–249, 2000.

[79] F. Ramos, M. Gajamohan, N. Huebel, and R. D'Andrea, *Time-optimal online trajectory generator for robotic manipulators*. Eidgenössische Technische Hochschule Zürich, Institute for Dynamic Systems and Control, 2013.

[80] G. Rosati, F. Oscari, L. Barbazza, and M. Faccio, "Throughput maximization and buffer design of robotized flexible production systems with feeder renewals and priority rules," *The International Journal of Advanced Manufacturing Technology*, pp. 1–17, 2015.

[81] A. Gasparetto and V. Zanotto, "A technique for time-jerk optimal planning of robot trajectories," *Robotics and Computer-Integrated Manufacturing*, vol. 24, no. 3, pp. 415–426, 2008.

[82] M. Zarebidoki, A. Lotfavar, and H. Fahham, "Dynamic modeling and adaptive control of a cable-suspended robot," in *Proceedings of the World Congress on Engineering*, vol. 3, 2011.

[83] Z. Ugray, L. Lasdon, J. Plummer, F. Glover, J. Kelly, and R. Martí, "Scatter search and local nlp solvers: A multistart framework for global optimization," *INFORMS Journal on Computing*, vol. 19, no. 3, pp. 328–340, 2007.

[84] A. Sharon, N. Hogan, and D. E. Hardt, "The macro/micro manipulator: An improved architecture for robot control," *Robotics and computer-integrated manufacturing*, vol. 10, no. 3, pp. 209–222, 1993.

[85] W. Cho, "Control of a high precision macro-micro robotic manipulator system," *KSME International Journal*, vol. 11, no. 1, pp. 29–44, 1997.

[86] M. Bamdad, F. Taheri, and N. Abtahi, "Dynamic analysis of a hybrid cable-suspended planar manipulator," in *2015 IEEE International Conference on Robotics and Automation (ICRA)*, pp. 1621–1626, IEEE, 2015.

[87] A. Trevisani, P. Gallina, and R. L. Williams II, "Cable-direct-driven robot (cddr) with passive scara support: theory and simulation," *Journal of Intelligent and Robotic Systems*, vol. 46, no. 1, pp. 73–94, 2006.

[88] L. Pigani and P. Gallina, "Cable-direct-driven-robot (cddr) with a 3-link passive serial support," *Robotics and Computer-Integrated Manufacturing*, vol. 30, no. 3, pp. 265–276, 2014.

[89] M. W. Spong, "Swing up control of the acrobot," in *Robotics and Automation, 1994. Proceedings., 1994 IEEE International Conference on*, pp. 2356–2361, IEEE, 1994.

[90] L. U. Odhner, L. P. Jentoft, M. R. Claffee, N. Corson, Y. Tenzer, R. R. Ma, M. Buehler, R. Kohout, R. D. Howe, and A. M. Dollar, "A compliant, underactuated hand for robust manipulation," *The International Journal of Robotics Research*, vol. 33, no. 5, pp. 736–752, 2014.

[91] M. Fumagalli, R. Naldi, A. Macchelli, R. Carloni, S. Stramigioli, and L. Marconi, "Modeling and control of a flying robot for contact inspection," in *2012 IEEE/RSJ International Conference on Intelligent Robots and Systems*, pp. 3532–3537, IEEE, 2012.

[92] K. Senda and Y. Murotsu, “Methodology for control of a space robot with flexible links,” *IEE Proceedings-Control Theory and Applications*, vol. 147, no. 6, pp. 562–568, 2000.

[93] G. Belforte, D. R. Aimonino, and P. Gay, *Robotics for improving quality, safety and productivity in intensive agriculture: challenges and opportunities*. INTECH Open Access Publisher, 2006.

[94] S. Haddadin, A. Albu-Schaffer, and G. Hirzinger, “The role of the robot mass and velocity in physical human-robot interaction-part i: Non-constrained blunt impacts,” in *Robotics and Automation, 2008. ICRA 2008. IEEE International Conference on*, pp. 1331–1338, 2008.

[95] D. Zanotto, G. Rosati, and S. K. Agrawal, “Modeling and control of a 3-dof pendulum-like manipulator,” in *Robotics and Automation (ICRA), 2011 IEEE International Conference on*, pp. 3964–3969, IEEE, 2011.

[96] N. Zoso and C. Gosselin, “Point-to-point motion planning of a parallel 3-dof underactuated cable-suspended robot,” in *Robotics and Automation (ICRA), 2012 IEEE International Conference on*, pp. 2325–2330, IEEE, 2012.

[97] M. Fliess, J. Lévine, P. Martin, and P. Rouchon, “Flatness and defect of non-linear systems: introductory theory and examples,” *International journal of control*, vol. 61, no. 6, pp. 1327–1361, 1995.

[98] H. Sira-Ramirez and S. K. Agrawal, *Differentially flat systems*. CRC Press, 2004.

[99] S. K. Agrawal and V. Sangwan, “Design of under-actuated open-chain planar robots for repetitive cyclic motions,” in *ASME 2006 International Design Engineering Technical Conferences and Computers and Information in Engineering Conference*, pp. 1057–1066, American Society of Mechanical Engineers, 2006.

[100] V. Sangwan, H. Kuebler, and S. K. Agrawal, “Differentially flat design of under-actuated planar robots: Experimental results,” in *Robotics and Automation, 2008. ICRA 2008. IEEE International Conference on*, pp. 2423–2428, IEEE, 2008.

[101] J. Franch, S. K. Agrawal, and V. Sangwan, “Differential flatness of a class of-dof planar manipulators driven by 1 or 2 actuators,” *IEEE transactions on automatic control*, vol. 55, no. 2, pp. 548–554, 2010.

[102] A. Konak, D. W. Coit, and A. E. Smith, “Multi-objective optimization using genetic algorithms: A tutorial,” *Reliability Engineering & System Safety*, vol. 91, no. 9, pp. 992–1007, 2006.

[103] D. E. Kirk, *Optimal control theory: an introduction*. Courier Corporation, 2012.

[104] L. S. Pontryagin, *Mathematical theory of optimal processes*. CRC Press, 1987.

[105] Z. Shiller, "Time-energy optimal control of articulated systems with geometric path constraints," *Journal of dynamic systems, measurement, and control*, vol. 118, no. 1, pp. 139–143, 1996.

[106] J. Aldrich and R. Skelton, "Time-energy optimal control of hyper-actuated mechanical systems with geometric path constraints," in *Proceedings of the 44th IEEE Conference on Decision and Control*, pp. 8246–8253, IEEE, 2005.

[107] M. Bamdad, "Time-energy optimal trajectory planning of cable-suspended manipulators," in *Cable-Driven Parallel Robots*, pp. 41–51, Springer, 2013.

[108] J. Kierzenka and L. F. Shampine, "A bvp solver based on residual control and the maltab pse," *ACM Transactions on Mathematical Software (TOMS)*, vol. 27, no. 3, pp. 299–316, 2001.

[109] C. Zheng, M. Bricogne, J. Le Duigou, and B. Eynard, "Survey on mechatronic engineering: A focus on design methods and product models," *Advanced Engineering Informatics*, vol. 28, no. 3, pp. 241–257, 2014.

[110] M. Lawson and H. Karandikar, "A survey of concurrent engineering," *Concurrent Engineering*, vol. 2, no. 1, pp. 1–6, 1994.

[111] W. Quan and H. Jianmin, "A study on collaborative mechanism for product design in distributed concurrent engineering," in *2006 7th International Conference on Computer-Aided Industrial Design and Conceptual Design*, pp. 1–5, IEEE, 2006.

[112] J. Aca, M. Ramos, J. L. Serrano, H. Ahuett, and A. Molina, "Concurrent engineering of mechatronic products in virtual enterprises: selection and deployment of a plm system for the machine tool industry," in *International Conference on Cooperative Design, Visualization and Engineering*, pp. 318–326, Springer, 2006.

[113] The Mathworks, Inc., Natick, Massachusetts, *MATLAB version 8.5.0.197613 (R2015a)*, 2015.

[114] S.-R. Oh and S. K. Agrawal, "Cable suspended planar robots with redundant cables: controllers with positive tensions," *IEEE Transactions on Robotics*, vol. 21, no. 3, pp. 457–465, 2005.

[115] S. Abdolshah and G. Rosati, “First experimental testing of a dynamic minimum tension control (dmtc) for cable driven parallel robots,” in *Cable-Driven Parallel Robots*, pp. 239–248, Springer, 2015.

[116] SKF, “Skf,” 2016.

[117] W. D. Pilkey and D. F. Pilkey, *Peterson’s stress concentration factors*. John Wiley & Sons, 2008.

[118] N. Sclater and N. P. Chironis, *Mechanisms and mechanical devices sourcebook*, vol. 3. McGraw-Hill New York, 2001.

[119] D. H. Myszka, *Machines and Mechanisms: Applied Kinematic Analysis*. Pearson Prentice Hall, 2005.

[120] B. A. G. . Co, “Beckhoff,” 2016.

[121] D. Jansen and H. Buttner, “Real-time ethernet: the ethercat solution,” *Computing and Control Engineering*, vol. 15, no. 1, pp. 16–21, 2004.

Enjoy the apetizer and dream the postpetizer.

— L. Barbazza